

This item was submitted to Loughborough University as a PhD thesis by the author and is made available in the Institutional Repository (<https://dspace.lboro.ac.uk/>) under the following Creative Commons Licence conditions.



For the full text of this licence, please go to:
<http://creativecommons.org/licenses/by-nc-nd/2.5/>



Pilkington Library

Author/Filing Title MULLAN, C

Accession/Copy No. 040165883

Vol. No. Class Mark

copy

FOR REFERENCE ONLY

040165883X



**SHAPE ANALYSIS
OF SYNTHETIC DIAMOND**

by

Claire Mullan

a doctoral thesis


submitted in partial fulfilment of the requirements for the award of

Ph. D.

of Loughborough University

28th September, 1997

© by Claire Mullan, 1997

 Loughborough University Library
Date Jul 98
Class
Acc No. 040165883

K0631025

ABSTRACT

Two-dimensional images of synthetic industrial diamond particles were obtained using a camera, framegrabber and PC-based image analysis software. Various methods for shape quantification were applied, including two-dimensional shape factors, Fourier series expansion of radius as a function of angle, boundary fractal analysis, polygonal harmonics, and corner counting methods. The shape parameter found to be the most relevant was axis ratio, defined as the ratio of the minor axis to the major axis of the ellipse with the same second moments of area as the particle.

Axis ratio was used in an analysis of the sorting of synthetic diamonds on a vibrating table. A model was derived based on the probability that a particle of a given axis ratio would travel to a certain bin. The model described the sorting of bulk material accurately but it was found not to be applicable if the shape mix of the feed material changed dramatically. This was attributed to the fact that the particle-particle interference was not taken into account.

An expert system and a neural network were designed in an attempt to classify particles by a combination of four shape parameters. These systems gave good results when discriminating between particles from bin 1 and bin 9 but not for neighbouring bins or for more than two classes.

The table sorting process was discussed in light of the findings and it was demonstrated that the shape distributions of sorted diamond fractions can be quantified in a useful and meaningful way.

ACKNOWLEDGEMENTS

I would like to express my gratitude to my employer, De Beers Industrial Diamond Division (Ireland), for supporting and financing this research. All of the work was carried out at the De Beers plant in Shannon and the following people helped in various ways; Dr. Rob Caveney, Mike Fish, Alan Hyde, Chris Taylor, Kieran O'Loughlin, Mike Frawley, Mike O'Dwyer, Pat O'Driscoll and his staff, Michele Leigh, Barry Cullen, Christy Leyden, Owen Kilker and Pat Forristal.

It was sometimes difficult to keep up with a busy full-time job and part-time study but there was always someone there to encourage me and I am indebted to my family, my friends Stephen, Richard, Lucy, Louise and Sara, and my workmates John, Michele and Kieran.

Finally, I would like to thank John Lloyd for supervising and guiding this work and for postponing full retirement to see me through to the end.

TABLE OF CONTENTS

Abstract	(i)
Acknowledgements	(ii)
Table Of Contents	(iii)
Nomenclature	(vi)
Index Of Figures	(viii)
Index Of Tables	(x)
1 INTRODUCTION	1
1.1 General Introduction	1
1.2 The Concept Of Shape Measurement	1
1.3 Introducing Synthetic Diamond	2
1.4 Shape Sorting On A Vibrating Table	4
1.5 The Problem	6
1.6 Objectives Of This Study	7
1.7 Scope Of The Study	8
2 SHAPE MEASUREMENT - A REVIEW	9
2.1 The Shape Quantification Problem	9
2.2 Separation Techniques	10
2.3 Analysis Of Individual Particles	12
2.3.1 Shape Factors	13
2.3.2 Fourier Analysis	17
2.3.3 Fractal Analysis And Polygonal Harmonics	23
2.3.4 Other Methods	28
2.4 A Review Of Shape Analysis Of Diamond	30
2.5 Summary	34
3 MEASURING THE SHAPE OF DIAMOND	36
3.1 Image Analysis	36
3.1.1 Description Of Equipment	36
3.1.2 Sample Preparation	39
3.1.3 Image Capture And Analysis	40
3.2 2-D Shape Factors	41
3.2.1 Identification Of Relevant Shape Factors	41

3.2.2	Relationship Between Shape Factors And Strength	45
3.3	Fourier Analysis	49
3.3.1	Theory	49
3.3.2	Determining The Fourier Coefficients	50
3.3.3	Fourier Analysis Results	53
3.3.4	Comparison Of Bin 2 With Bin 9 Using Fourier Coefficients	60
3.3.5	Discussion Of Fourier Analysis Results	62
3.4	Fractals And Polygonal Harmonics	63
3.4.1	Boundary Fractal Analysis	63
3.4.2	Polygonal Harmonics	65
3.5	Counting Corners	70
3.5.1	The Spanning Chord Method	72
3.5.2	The Radius of Curvature Method	76
3.5.3	Comparison Of Corner Counting Methods	78
3.6	Summary Of Shape Exploration	78
4	MODELLING DIAMOND TABLING	80
4.1	Investigating The Measurement Of Axis Ratio	80
4.1.1	Verification Of Axis Ratio	80
4.1.2	Effects Of Image Capture Conditions	81
4.1.3	Choice Of A Sample Size	81
4.2	Sampling	83
4.2.1	Sampling Experiment 1	83
4.2.2	Sampling Experiment 2	88
4.3	Modelling	90
4.3.1	Basis For A Model	90
4.3.2	Experimental Data	91
4.3.3	Setting Up The Models	93
4.3.4	Testing The Models	95
4.3.5	Discussion	99
4.3.6	Developing The Model	103
5	ARTIFICIAL INTELLIGENCE	105
5.1	Expert System	105
5.1.1	Setting Up The Expert System	106
5.1.2	Expert Results	110
5.2	Neural Network	112

5.2.1	A Feedforward Network With Training By Back Propagation	112
5.2.2	Setting Up The Network	114
5.2.3	Neural Network Results	116
5.3	Predicting Tabling	117
5.3.1	Discussion	119
6	APPLICATIONS AND DISCUSSION	122
6.1	Summary	122
6.2	Learning From Axis Ratio Measurements	126
6.2.1	Learning Experiment 1	126
6.2.2	Learning Experiment 2	128
6.3	Discussion	129
6.3.1	Past	129
6.3.2	Present	130
6.3.3	Future	133
6.4	Conclusion	134
	References	135
	Appendix 1 - Program For Finding Edge Coordinates	139
	Appendix 2 - Program For Calculating Fourier Coefficients	141
	Appendix 3 - Program For Polygonal Harmonics	144
	Appendix 4 - Program For Spanning Chords	146
	Appendix 5 - Program For Spacing Points Evenly	147
	Appendix 6 - Program For Radius Of Curvature	149
	Appendix 7 - Calculation Of Axis Ratio	151
	Appendix 8 - Program For Calculation Of Axis Ratio	153
	Appendix 9 - Expert System Program	155
	Appendix 10 - Neural Network Program	157

NOMENCLATURE

Shape Factors

$A, a, b, c, d, N, P, R, r, S, S_S, S_T, s, V, x, y, z,$	see table 2.1, page 14
k	ratio of long axis to short axis of equivalent ellipse
w_m	maximum projected sphericity
α	fraction of ellipse

Fourier Analysis

A_1	intercept of fitted line on a plot of A_n versus n
A_n	amplitude of n th harmonic
a_n	magnitude of n th cosine component
b_n	magnitude of n th sine component
L	maximum arc length = perimeter
L_o	size normalised mean radius of profile radial distribution
$L_2(n)$	LBV shape descriptors (see page 19)
$L_3(m,n)$	LBV shape descriptors (see page 19)
l	arc length between start point and point xy
N	number of coefficients in a truncated series
n	harmonic number
R_o	radius of a circle with the same area as the profile
$R(\theta)$	radius at angle θ
s	normalised arc length
s	slope
α_n	phase angle of the n th component
$\phi(l)$	angle between tangent at start point and tangent at xy
$\phi^*(t)$	$\phi(l)$ normalised for interval $[0,2\pi]$
μ_i	i th moment about the mean of the radial distribution
θ	angle relative to a chosen axis
σ_m	scatter

Fractal Analysis

D	fractal dimension
e	step size
$L(e)$	length estimate for step size e
r	disc radius
w	width of boundary

Modelling

b_i	proportion of sample in class i
c_i	i th axis ratio class
d_j	proportion of sample in bin j
n	sample size
p_{ij}	probability that a particle in the i th axis ratio class will land in bin j
w_{ij}	proportion that is in the i th axis ratio class and has landed in bin j
σ	standard deviation

Expert System

$d(j)$	decision vector for outcome j
$r(i,j)$	rule vector for i th variable and j th outcome
V_i	i th input variable
V_{norm}	value of the variable normalised in the range [0,1]
$V_{\text{min}}, V_{\text{max}}$	minimum, maximum values in the range for the variable

Neural Network

A_d	desired activation
A_j	activation of j th node
I_j	input to j th node
w_{jk}	weight associated with the i th input to the j th node
Δw_{jk}	previous change in w_{jk}
α	momentum
δ_k	a parameter related to the error at node k
η	learning rate
θ_j	threshold for j th node

Other

M	a parameter related to magnetic susceptibility
UB	percentage of unbroken crystals in the Friatest

INDEX OF FIGURES

Figure 1.1	Growth of synthetic diamond	3
Figure 1.2	SDA25+	5
Figure 1.3	SDA100S	5
Figure 1.4	A sorting table	6
Figure 2.1	Synthetic diamond morphology index	32
Figure 2.2	Definition of GE's tau	33
Figure 3.1	Image analysis equipment	38
Figure 3.2	Prepared slides	38
Figure 3.3	Image of diamond particles with particle outlining	40
Figure 3.4	Variation of perimeter with bin number	42
Figure 3.5	Variation of length with bin number	42
Figure 3.6	Six parameters showing trends with bin number	43
Figure 3.7	Cumulative distributions	45
Figure 3.8	Shape parameters related to strength parameter	48
Figure 3.9	UB predicted from shape parameters	48
Figure 3.10	Five diamond profiles	51
Figure 3.11	Regeneration errors for particles 1-5	52
Figure 3.12	Particle 1 (a) original, (b) regenerated using 50 coefficients, (c) regenerated using 500 coefficients	52
Figure 3.13	Particle 5, (a) original, (b) regenerated using 50 coefficients, (c) regenerated using 500 coefficients	52
Figure 3.14	Profiles of 24 particles from bin 2	54
Figure 3.15	Profiles of 24 particles from bin 9	54
Figure 3.16	Magnitudes of Fourier coefficients	56
Figure 3.17	$\ln(A_n)$ v's $\ln(n)$ for the three particles shown	59
Figure 3.18	Triangular graph of Fourier coefficients A_2, A_3, A_4	60
Figure 3.19	Triangular graph of $L_2(2), L_1(3), L_2(4)$	61
Figure 3.20	Sums of first 6 coefficients	62
Figure 3.21	Second coefficient	62
Figure 3.22	Second Fourier coefficient plotted against axis ratio for particles from bin 2 and bin 9	63
Figure 3.23	Richardson plot of computer drawn shapes	64
Figure 3.24	Richardson plot for five particles	65
Figure 3.25	Harmonic frequency histogram	69
Figure 3.26	Polygonal harmonic frequencies	69
Figure 3.27	Second polygonal harmonic plotted against axis ratio for particles from bin 2 and bin 9	70
Figure 3.28	Test shapes generated by computer	71
Figure 3.29	Spanning a corner	72
Figure 3.30	Spanning chord plots for shapes A and B, step length 10	72
Figure 3.31	Spanning chord plot for shape C (uneven spacing of points)	73
Figure 3:32	Spanning chord plots for shapes A to E with evenly spaced points	74
Figure 3:33	Spanning chord plots for particles from Figs 3.14 and 3.15	75
Figure 3.34	Radius of curvature plots for shape C ($s=7$)	76
Figure 3.35	Radius of curvature plots for selected shapes	77
Figure 4.1	Axis Ratio Distribution 1040 particles from bin 2	82
Figure 4.2	Bin 2 sampling plan	84
Figure 4.3	Weight% distributions for <i>tb1</i> and <i>tb2</i>	93
Figure 4.4	Axis ratio distribution of selected bins	94
Figure 4.5	Axis ratio averages and standard deviations for <i>tb1</i> and <i>tb2</i> compared	94

Figure 4.6	Probabilities for <i>tb1</i> and <i>tb2</i> for selected axis ratio classes	96
Figure 4.7	Predicted weight distributions for retabbling of selected bins and predicted repeatability curves	98
Figure 4.8	Retabbling of <i>tb2</i> bins, predicted and actual	99
Figure 4.9	Original <i>tb2</i> and reset <i>tb2</i> distributions by bin	100
Figure 4.10	Scatter plot showing length dif and axis ratio to be independent variables .	103
Figure 4.11	Reproducibility curves for various axis ratio/length dif models	104
Figure 5.1	Expert's performance up to 5,000 training cases	108
Figure 5.2	Expert's performance up to 16,000,000 training cases	108
Figure 5.3	Example of a neural network	112
Figure 5.4	Activation function	113
Figure 5.5	Predicting tabling at <i>tb2</i> settings (a) expert system (b) neural network	118
Figure 5.6	Bulk tabling predicted by expert with inclusion of axis ratio probabilities .	119
Figure 6.1	Cumulative axis ratio distributions for bulk tabling with deliberate interference	127
Figure 6.2	Cumulative axis ratio distributions after retabbling bins 6 to 9	127
Figure 6.3	Cumulative axis ratios for magnetic fractions of (a) bin 1 and (b) bin 9	128
Figure 6.4	Cumulative axis ratios of diamond compared with SiC	132

INDEX OF TABLES

Table 2.1	Examples of shape factors	14
Table 3.1	Fourier coefficients for rotated particles	55
Table 3.2	Slope, intercept and scatter for A_n v's n	58
Table 3.3	Fractal dimensions for five particles	65
Table 3.4	Determining the polygonal harmonics for particle 8, bin 2	67
Table 4.1	Axis ratios for bin 2	85
Table 4.2	T-test results for bin 2	85
Table 4.3	Axis ratios for bin 9	86
Table 4.4	T-test results for bin 9	86
Table 4.5	Axis ratios for bin 8	88
Table 4.6	T-test results for bin 8	89
Table 4.7	Differences in distribution on retableting <i>tb2</i> material at slightly altered settings	100
Table 4.8	Comparison of predicted (p) with actual (a) weight distribution for <i>tb2</i>	101
Table 5.1	Expert's rules $r(i,j)$ for $j=2$ (bin 9) for 50/60 bins 1 and 9	109
Table 5.2	Performance of averaged rules	109
Table 5.3	Performance by training with averaging - 50/60 bins 1 and 9	110
Table 5.4	Expert's range of performance over ten trials	111
Table 5.5	Neural Network v's Expert System for tabled bulk 40/45	116
Table 6.1	Examples of observations that have been quantified	130

1 INTRODUCTION

1.1 GENERAL INTRODUCTION

Scientists and engineers who work with powders or particulate materials are aware of the fact that particle shape influences particle behaviour. They are constantly looking for new and improved methods of analysing the shapes of particles so that they can better understand and enhance the performance of their materials.

This dissertation explores the possibilities for quantifying the shapes of the particles in synthetic diamond grits produced for saw-blades. It then uses shape measurements to analyse the shape sorting process. This chapter provides the background and describes the concepts and principles involved, before stating the objectives of the study. Chapter 2 contains a general overview of the literature on shape quantification. Selected methods are applied to diamond in Chapter 3 and used for modelling in Chapter 4. The use of artificial intelligence for shape classification is explored in Chapter 5. Conclusions are summarised and discussed in the final chapter.

1.2 THE CONCEPT OF SHAPE MEASUREMENT

Because people are accustomed to using numbers to describe size and words to describe shape, there is a tendency to think that shape is much more difficult to quantify than size. Size measurement is much more complex than many people realise, and shape measurement presents the same difficulties. Measuring the shape of fractions from a shape-sorting operation is a similar problem to measuring the size of fractions from a size-sorting operation (such as batch sieving). In either case the property must be defined before it can be measured and the most suitable definition depends on the reason for wanting the measurement.

Before commencing any study on shape the following fundamental principles must be acknowledged and understood.

- ♦ Separation and measurement are two different things.

- Shape is easily quantified. The difficulty is in identifying the most suitable quantifier for the application.
- Few, if any, characteristics or behavioural traits of a particulate material are influenced by particle shape alone.

These principles apply to all particulate materials, whether the shapes are regular or irregular, and diamond is no exception.

1.3 INTRODUCING SYNTHETIC DIAMOND

Diamond is an allotrope of carbon and is the hardest natural substance known. Each carbon atom lies at the centre of a regular tetrahedron and is bonded covalently to four other carbon atoms lying at the corners of the tetrahedron. The chemical stability and hardness of diamond are due to the rigidity of this structure and the nearness of the atoms (1.54 Angstroms). The optical properties of diamond, such as a high refractive index, give natural polished stones a brilliance that has made them popular in the gem market. The output from diamond mines also includes stones of lower quality, and it was quickly realised that the hardness of these rejects could be exploited. Called industrial diamonds, these natural stones find application in drilling and cutting operations.

Graphite is the stable form of diamond at normal temperatures and pressures. Diamond is of higher density than graphite (3.52 as against 2.25) and is the high pressure form of carbon, but pressure alone is not enough to convert graphite to diamond. High temperature is required to provide sufficient energy to allow the carbon atoms to regroup into the diamond crystal lattice form. The first commercial synthetic diamonds were produced by General Electric in the early 1950s. Today there are many companies world-wide in the business of making diamond by high-temperature, high-pressure synthesis. The conversion of graphite to diamond is aided by metal solvents/catalysts, the most common combinations being cobalt/iron, iron/nickel and manganese/nickel. The graphite/metal mixture is encased in a ceramic capsule and inserted into a cemented tungsten carbide die, which is supported by a set of hardened steel rings in the press. Uniaxial pressure is applied through cemented

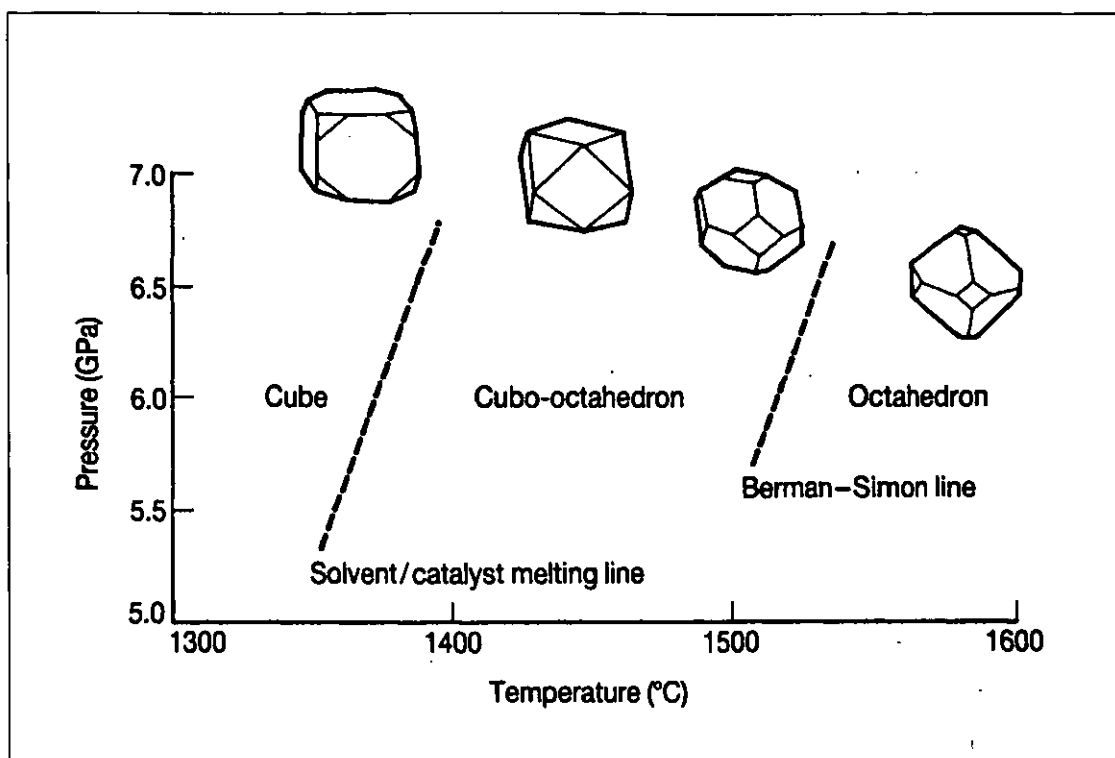


Figure 1.1 : Growth of Synthetic Diamond (after Figure 10.4 in *The Properties of Natural and Synthetic Diamond*, J. E. Field ed., Academic Press, 1992)

tungsten carbide anvils and high temperatures are produced by an electric current. Typical pressures and temperatures are shown in *Figure 1.1*.

Carefully designed pressure/temperature profiles give some control over the amount of time spent at conditions suitable for spontaneous nucleation, and at conditions suitable for crystal growth, so the process can be tuned to produce diamonds with a size distribution peaking at a certain size. The relative growth rates of the different faces, and hence the final shapes of the crystals, are influenced also by the thermodynamic and chemical conditions in the capsule. The dominant crystal habit for diamonds synthesised by this technique is the cubo-octahedron. Diamonds of a cubic habit are formed at a higher pressure and lower temperature than diamonds of an octahedral habit.

After synthesis the diamonds are recovered by dissolving the metal and the remaining graphite in acid. The output of any one press run contains a distribution of sizes centring on the target peak size. There is also a variation in the crystallinity and purity of the particles, ranging from clear regular crystals to twinned crystals and

irregular particles with metal inclusions. A sieving operation sorts into size bands, then vibrating tables sort into shape classes. The result is a range of products, each uniform in its particle characteristics.

Industrial diamond applications include cutting, grinding, sawing, drilling, wire drawing, coring, and polishing. To cover this wide range of applications there are natural and synthetic grits, strong crystalline grits, weak friable grits with a mosaic particle structure, large monocrystals and micronised powders. The diamonds are incorporated into tools using metal bonds, resin bonds, vitrified bonds, or electroplating. These grits cannot all come from the same synthesis process, so the ingredients in the capsule and the thermodynamic profile for the press runs vary for the different product types.

This study will be confined to one type of synthetic diamond, namely sawgrits. The SDA (Saw Diamond Abrasive) range of sawgrits manufactured by De Beers Industrial Diamond Division consists of eight different products in a range of sizes from 20/30 to 70/80¹. At the top end of the range are very strong, pure, regular crystals for sawing the hardest stone and cast refractories. At the lower end are crystals of lower strength, with metal impurities and less regular shape. These grits are used for the production of handheld, non-professional tools. *Figures 1.2 and 1.3* show the products at the extreme ends of the range.

There is no such thing as a reject particle in this industry because the wide range of products ensures that every particle is suitable for sale. However, particles are not purchased individually so it is essential that the sorting processes, including shape sorting, are effective in producing homogeneous particle sets.

1.4 SHAPE SORTING ON A VIBRATING TABLE

If a sample of particulate material is fed onto an inclined vibrating table at appropriate settings, the material separates into a number of classes. Assuming that the feed material is reasonably homogeneous with regard to size, surface texture and density, it

¹ These sieve sizes indicate the number of wires per inch in the US mesh system. The use of "US Mesh" is now obsolete and "70/80 US Mesh" can be expressed as 70/80 or 70/80#. The particles in a 70/80 size have diameters of about 200µm while 20/30 particles are approximately 1mm in diameter.

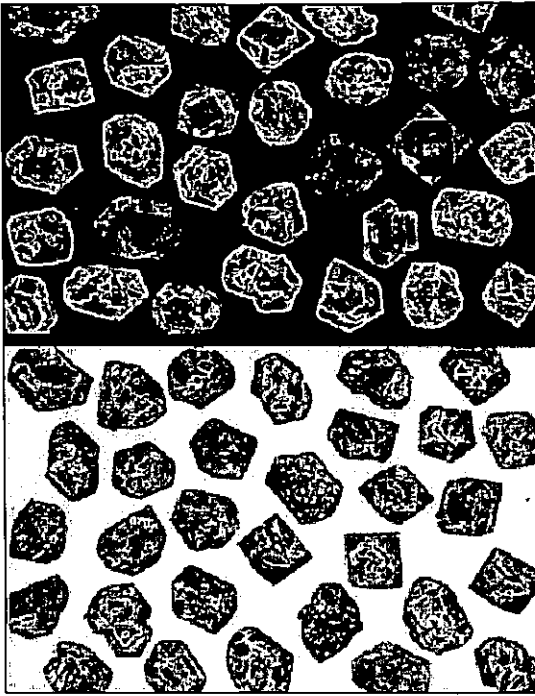


Figure 1.2 : SDA25+

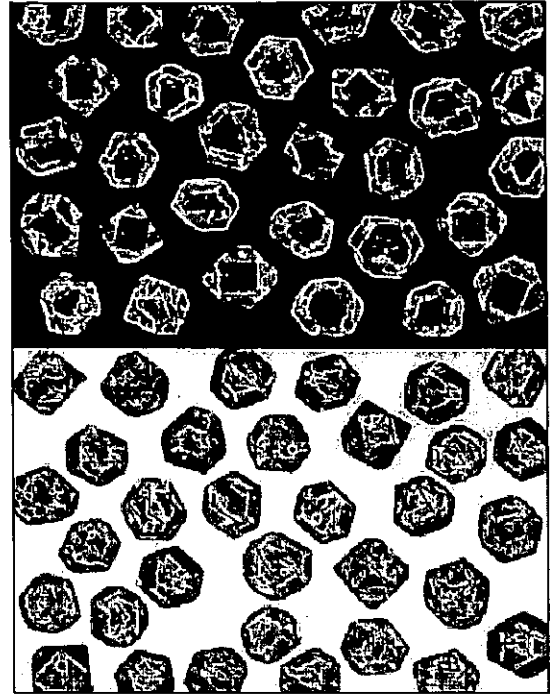


Figure 1.3 : SDA100S

is believed that the classification by the table is based on the influence of the shapes of individual particles on their movement across the table, and that the collecting bins contain shape fractions. Visual examination of the contents of the bins confirms a gradual change in overall appearance of the fractions, from rounded or blocky at one end of the table to irregular, flattened or elongated at the other end. The common explanation for this is that the rounded particles tend to roll and choose the steepest path available, while irregularly shaped particles couple to the vibration and take a higher path across the table.

Figure 1.4 shows a standard Jeffrey Galion table with twelve collecting bins. Its variable parameters include feed rate, tilt angle, fore and aft angle, vibration level and deck surface. In most industrial processing applications, optimisation of these parameters tends to be based on getting an even spread across the bins, with the feed rate as high as possible. The distribution by weight across the bins is sometimes used as a shape measurement of the feed material for comparison purposes, but, strictly speaking, the vibrating table is not a shape-measuring device. It is a sorting tool, designed to divide a material into sub-classes based on shape. Usually the output of a tabling operation is examined by an experienced technician, the bin contents are split

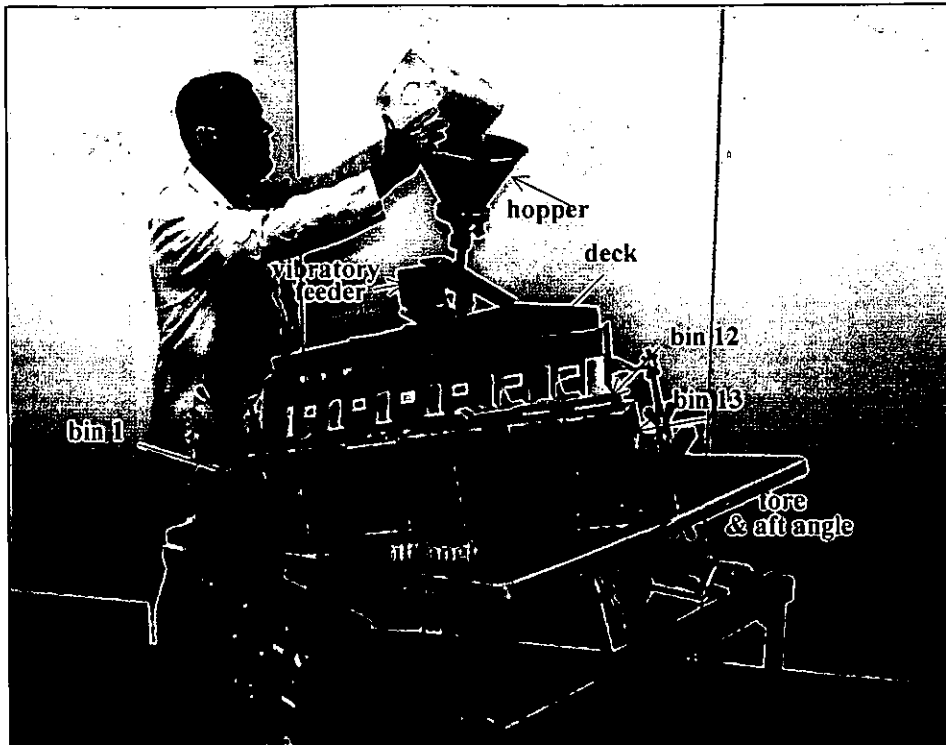


Figure 1.4 : A sorting table

or combined to give the required, visually acceptable fractions, and no measurement of shape is carried out.

1.5 THE PROBLEM

The vibrating table gives very little quantitative information on shape, and the shape gradient it produces for diamond particles is not understood. There is a certain amount of randomness in the movement of a particle across the deck so reproducibility is poor and there is a large overlap between the shape fractions produced, no matter how they are assessed. It is believed that the relative sizes of different facets on a diamond particle affect its tabling behaviour, resulting in a shape separation unique to the diamond industry.

The many experiments carried out within the diamond industry in the past have failed to explain some of the tabling mysteries. For example, if the contents of all the table bins are recombined and sorted again at the same settings the distribution by weight across the bins is repeatable, but if the contents of one of the middle bins is retabled on its own less than half of it will return to the bin from which it came. The rest

spreads out to the other bins. Suggested explanations are: (a) the interference between particles on the table is different if the feed material is different, and (b) the destination of a particle is governed by probabilities relating to the size and number of edges and flat faces. Some work has been done to lend credibility to the former (this is discussed on page 131) but there is still a lack of understanding of what is really happening. Is the "even" sort the optimum sort? Why is there such an apparent overlap between the contents of adjacent bins? Why is the weight distribution repeatable when there appears to be so much randomness involved?

These questions can only be answered if the bin contents can be analysed in detail, preferably by measuring individual particle shapes and analysing the shape distributions in the feed material and in the bins. Until recently this was almost an impossible task but now, with ever-increasing computer power, techniques like image analysis are more accessible. The ability to measure large numbers of particles and process data at high speed without huge capital expenditure has opened up new possibilities for quantifying shape. The time has come for a fresh look at the tabling of synthetic diamond.

1.6 OBJECTIVES OF THIS STUDY

The following hypotheses are proposed:

Hypothesis 1: There exists a shape quantifier that describes meaningfully the table sorting of synthetic diamond sawgrit particles.

Hypothesis 2: The shape quantifier can be used to characterise and model the table sorting of synthetic diamond sawgrit particles.

The first hypothesis can be tested by applying known methods of shape measurement to tabled fractions. This hypothesis is supported if one or more methods show a definite trend in mean shape value across the bins of a table, and if the measured shape correlates with another measurable property known to be influenced by shape. If such a quantifier is found then hypothesis 2 can be tested by analysing bin contents for various table settings, repeat tabling, and retableting of individual bin contents. The

probabilities associated with the destinations of particles of a certain measured shape can be determined from the experimental data, and form the basis of a model. If a model can be set up, then both hypothesis 1 and hypothesis 2 are confirmed.

The primary objective of this thesis is to produce a tabling model that is characteristic for diamond sorting. Secondary objectives are to understand and apply to diamond many different shape measurement techniques, to solve some of the mysteries of table sorting, and to suggest some improvements in diamond processing.

1.7 SCOPE OF THE STUDY

The study is confined mostly to De Beers SDA type synthetic sawgrit in size 40/45 but other types or sizes are used for convenience or to illustrate a point. Tabling was carried out on tables similar to the Jeffrey Galion table shown in *Figure 1.4*, but with some minor modifications. The findings and conclusions of this study only apply to SDA type material tabled on these tables, although the general principles may hold for other applications.

Some samples were taken by production personnel during routine tabling but otherwise all of the reported tabling, sampling, slide preparation, image analysis measurements, data manipulation, computer programming and typing were carried out by the author.

2 SHAPE MEASUREMENT - A REVIEW

Many particle characteristics or properties are influenced by the shape of the particle, and cannot be analysed in full without taking the shape into account. This creates a need for shape measurement techniques across many branches of science and engineering. Particle technology is a recognised field in itself, but publications on shape analysis originate from disciplines as diverse as geology and aerospace engineering. There is a continuing demand for better methods of characterising the shapes of both individual particles and bulk powders. This has prompted the exploration of a multitude of different techniques for quantitative measurement of shape.

2.1 THE SHAPE QUANTIFICATION PROBLEM

Luerkens, Beddow and Vetter [1] defined particle shape as the recognised pattern of relationships among all of the points which constitute the external surface of the particle. Lloyd [2] suggested that the only way to characterise a particle's shape fully is to divide the surface into small areas and record the location and orientation of each of these areas. He pointed out that even if this were practical it depends on the chosen magnitude of the areas, and conveys little useful information about the particle. Hausner [3] listed characteristics of individual powder particles and of bulk powder and explained the difficulties of singling out any one of them to determine its effect on powder behaviour. Flook [4], on investigation of several different quantitative methods of shape description, concluded that *it is unrealistic to expect that any one type of shape coefficient will adequately quantify all the aspects of particle morphology that contribute to the physical properties of powders in bulk*. More than sixty years ago Wentworth said [5] *it is to be hoped that more investigators will apply self-devised quantitative numerical methods to their problems, while profiting from the successes and failures of their predecessors*. Nothing has been developed yet to change this sentiment.

The task of quantifying particle shape is obviously not an easy one. It is more or less agreed among the researchers in this field that it is overly ambitious to look for an absolute, universally applicable solution to the problem, so the only approach to take is to look for the method which gives the most useful and meaningful results in the context of a single application. In some cases this will mean no more than applying a simple, well-established technique; in others it may be necessary to invent a new one. Meloy, Mani and Clark [6] pointed out in a review of particle shape analysis and separation techniques that the human eye is the most sophisticated shape research tool, and its usefulness in identifying which shape properties to measure should not be overlooked. They claim that the secret of successful analysis is to *avoid getting lost in a hyperspace of too many dimensions*.

It has already been stated that separation and measurement are two different things. However, in particulate industries there is generally a need for both and sometimes the result of a sorting operation is used as a characterisation of the feed material. For example, a sieving operation sorts by size, but the relative amounts of material on the sieves can prove that a sample is coarser or finer than another sample with a different sieving result. Although no actual measurement has been made the result of sorting has given some information about size. The same applies to tabling and shape measurement. However, since single particle measurement is the main concern in this work, shape separation techniques are reviewed separately, and the review of measurement methods concentrates on individual particle analysis. Bulk shape analysis (for example packing density) is not discussed.

2.2 SEPARATION TECHNIQUES

There are many ways to sort a particulate material according to behaviour that is influenced by particle shape. Examples of sorting devices based on the movement of particles on a vibrating surface are tilted vibrating plate, tilted vibrating trough, tilted rotating cylinder, tilted rotating disc, and tilted vibrating screen. These techniques have been in use for many years for mineral processing and in the grain industries. Endoh [7] modelled the behaviour of particles on a vibrating plate to show that

particles may be effectively sorted according to frictional properties at low inclination angle. Ohya et al [8] developed an inclined conveyor belt based on a similar model.

More recently, Meloy and his colleagues [9,10,11] developed sieve cascadowgraphy as a method of shape separation. This works on the principle that the residence time on a sieve is dependent on shape. If a closely-sized fraction of particles is sieved through a stack of identical sieves, the more irregular particles will take longer to arrive at the catchpan. This idea has been expanded to a two-dimensional network of sieves by Meloy and Williams [12], but is intended for separating spheres of similar but different diameters. It is interesting to note that these authors used the same mathematical techniques to model the behaviour of particles in both the two-dimensional cascadowgraph [12] and a vibrating plate [13]. In both of these separation methods each particle spends much of its time in flight, and its movement is influenced by its orientation each time it lands. The models allow particles to move in one of two directions on each bounce. Different particle populations have different probabilities associated with these directions and the models show how the populations separate over time. This is a highly simplified approach but the idea of basing the model on probabilities is attractive.

Another sieving method for shape separation is the use of slotted screens. Nakajima et al [14] developed a practical method of using square aperture and rectangular slot sieves for shape analysis of crushing operations. Slotted sieves sort particles by two of their three principal dimensions - thickness and width. Whiteman and Ridgeway [15] compared the performance of slotted screens and a vibrating table in sorting both citric acid monohydrate and sodium perborate tetrahydrate. They used triaxial measurements and various shape factors to analyse the fractions produced by the sorting methods, and found that $width*thickness/length^2$ best described the shape variation for both materials and both methods. Ludwick and Henderson [16] studied the behaviour of ellipsoids (handmade from alabaster or ivory) on square aperture sieves, and developed a mathematical sieving theory based on particle passing probabilities. An interesting finding was that the type of particle making up the core of a fraction occurred in that fraction only, while other particles were distributed

among other fractions. The authors suggested that the size distribution of a sieved sample should be constructed as *a plurality of bell-shaped distributions, the area under each being proportional to the weight or number of particles trapped in each sieved fraction*. Since their probability tables could only be used if a shape distribution of the input material was known, they finished their 1968 paper with the comment that a practical method of obtaining particle shape data was needed. Ludwick [17] later studied the passage of sand grains through a stack of slotted sieves of decreasing slot width and showed how to calculate the frequency distribution of relative particle thickness.

Differences in the particle holding force or adhesion may also be used to sort by shape. Sano and co-workers have developed shape separators based on these differences. Particles are fed onto a rotating drum with circular holes. Spherical particles are held more tightly by the air suction than the non-spherical ones, which can be brushed off into a collector [18]. Alternatively particles are fed onto a rotating glass cylinder vibrated by an electromagnet. Non-spherical particles fall off and spherical particles are carried around to be brushed off into a separate collector [19].

The drag coefficient of a particle settling in a fluid depends on its shape as well as other factors. The settling velocity depends on the drag coefficient, the mass and the projected area in the settling direction. Sedimentation techniques are commonly used for sizing very fine particles, but can also be applied for shape separation. Endoh and Iwata [20] demonstrated the use of this technique to separate blocky mica particles from flaky ones.

A review of shape separation of particles has been published by Furuuchi and Gotoh [21]. It describes all of the above techniques in detail and provides a comprehensive list of references.

2.3 ANALYSIS OF INDIVIDUAL PARTICLES

Single particle shape quantification can be divided into two main categories. The first involves making actual measurements on the particle or some profile of the particle

and combining the measurements to obtain a shape factor. Typically the measurements have dimensions of length, area or volume. An example of such a shape factor is *maximum diameter*minimum diameter/area*. A brief history and review of the development of this type of shape factor is given in section 2.3.1. Many of these can be applied to diamond particles and will be discussed further in Chapter 3.

The second type of measurement is based on computation using the co-ordinates of a two-dimensional particle outline. Fourier analysis and fractal analysis are two of the methods in use and there are also some methods for counting the corners on the outline. These are introduced and reviewed in sections 2.3.2, 2.3.3 and 2.3.4 respectively, and are applied to diamond in Chapter 3.

2.3.1 Shape Factors

Prior to the development of fast computers and automatic imaging systems, the task of analysing particles individually was very tedious and slow. For larger particles triaxial measurements could be made mechanically, but even the simple idea of picking three diameters has never been rigidly defined, and there is no agreement as to whether or not the three diameters should have a common point of crossing, or even be mutually perpendicular. Wadell [22] tried to move away from characterisation by diameter and proposed measurements of sphericity and roundness. As he was interested in sedimentation he defined sphericity in terms of surface area compared to the surface area of a sphere of equal volume. He defined roundness as the sum of the curvature of all the corners in one plane of the particle, where the curvature of a corner is expressed as the ratio of the radius of curvature of the corner to the radius of the maximum inscribed circle in the plane of measurement. The impracticalities of using these definitions in practice, however, meant that he later resorted to using diameters of circumscribed circles and of circles of equivalent projected area, instead of surface area measurements [23]. Nevertheless, he saw roundness and sphericity as two distinct properties. Wentworth [5] disagreed with these definitions on the basis that a particle could then have a high degree of sphericity and no roundness, which contradicts the intuitive notion of sphericity. He also pointed out that there was a

Author	Shape Factor		Symbols
Wadell	sphericity	$\frac{s}{S}$	s = surface area of a sphere of the same volume as the particle S =surface area of the particle
	roundness	$\frac{\sum \frac{r}{R}}{N}$	r =radius of curvature of a corner R =radius of maximum inscribed circle in the plane N =number of corners in the plane
Zingg	four classes of roundness based on :	$\frac{b}{a}, \frac{c}{b} < \frac{2}{3}$	a =longest diameter b =intermediate diameter=longest diameter perpendicular to a c =short diameter=longest diameter perpendicular to a and b
Krumbein	sphericity	read from chart $\frac{b}{a} v' s \frac{c}{b}$	a, b, c as above
Aschenbrenner	sphericity	$\frac{S_s}{S_T}$	S_T =surface area of the tetrakaidekahedron defined by orthogonal dimensions of the particle S_s =surface area of a sphere of the same volume as the tetrakaidekahedron
Heywood	volume coefficient	$\frac{V}{d^3}$	V =volume of the particle d =diameter of circle of same area as projected particle profile
	surface area coefficient	$\frac{S}{d^2}$	S =surface area of particle d =as above
Hausner	elongation	$\frac{a}{b}$	a, b =long, short sides of enclosing rectangle of minimum area
	bulkiness	$\frac{A}{a \times b}$	A =area of particle profile
	surface factor	$\frac{P^2}{4\pi A}$	P =perimeter of particle profile
Medalia	anisometry	$\frac{a}{b}$	a, b =major, minor axis of ellipse with same radii of gyration as particle profile
	bulkiness	$\frac{\pi ab}{A}$	πab =area of ellipse A =area of particle profile

Table 2.1 : Examples of shape factors

growing number of indexes of sphericity and roundness, and that no one of them could be the "correct" one.

Zingg [24] used triaxial measurements to classify pebbles by shape. The four classes were based on the ratios of an intermediate diameter to the long diameter and the short to the intermediate diameter, and were described as disks, spheres, blades, and rods. Some years later Krumbein [25] developed a procedure for measuring sphericity

which used the same ratios as Zingg and gave average sample values in agreement with results from Wadell's method. Krumbein's sphericity was based on Wadell's definition but used the volume of an ellipsoid rather than a sphere. The procedure for obtaining the results was much more practical, although very crude by today's standards. It involved making calliper measurements of the three diameters, calculating the ratios, and plotting them on a special chart. This routine took one to two hours for fifty pebbles, or thirty minutes using a less accurate version of the routine. Roundness was then estimated by comparing each pebble to a set of pictures of pebbles of known roundness.

Aschenbrenner [26] took Wadell's sphericity a step further. The length, width and thickness measurements were used this time to approximate to a tetrakaidekahedron - a form which is bounded by three pairs of equal and opposite quadrilateral faces and by four pairs of equal and opposite hexagonal faces. This was chosen in preference to an ellipse because the surface area is more easily calculated and because sedimentary particles do not usually have smooth surfaces. Sphericity was then defined as the ratio of the surface area of a sphere of the same volume as the tetrakaidekahedron to the surface area of the tetrakaidekahedron. Because of the greater angularity this gives slightly smaller values of sphericity than Krumbein's ellipsoidal estimation.

Perhaps the most well-known measures of shape are the Heywood shape factors [27], which relate the mean projected diameter of a particle to its volume or surface area. Because of the difficulties in measuring the volume and surface area of an individual particle these shape factors tend to be determined using approximations. The volume coefficient can be calculated if the number of particles and the mean size, weight and density of a closely sized fraction are known. Calculation of the surface coefficient requires the use of a table of constants derived by Heywood for the shape groups of angular tetrahedral, angular prismoidal, sub-angular and rounded.

Instead of concentrating on spheres, Hausner [3] opted to examine the projected profile of a particle in its most stable plane and base his dimensionless shape factors on the surrounding rectangle of minimum area. The ratio of the long to the short sides of the rectangle gives an elongation factor. The bulkiness is measured by the ratio of

the area of the particle to the area of the rectangle. Finally, resorting to a circle again, the surface factor compares the perimeter of the particle to the perimeter of a circle of equivalent area. The formula for calculating the surface factor is $P^2 / 4\pi A$, where P is the length of the perimeter and A is the area. This has since become widely accepted as a measure of circularity.

Medalia [28] also devised anisometry and bulkiness shape factors, but instead of using a bounding rectangle he approximated the particle by an ellipsoid with equivalent radii of gyration according to the rules of rigid body dynamics. The anisometry is taken as that of the ellipsoid, and the bulkiness is determined from a comparison of the volume of the ellipsoid with that of the particle. For simplification, a two dimensional ellipse can be used to represent a projection or section of the particle. Whereas most of the shape factors discussed so far are based on the convex hull of the particle, Medalia's method takes every point on the body into account (within the limits of the chosen resolution, of course). In the quantification of macro shape, convex hull methods tend to be unduly affected by protuberances or other minor variations in shape.

A population of particles can be represented by a triangular plot using triaxial measurements. This technique is used in sedimentology to study the effects of folding and faulting on the deformation of pebbles in the earth's crust, or to study the sand and silt content of sediments. For example, Burns and Spry [29] plotted ellipsoidal pebbles on a triangular diagram with sides $\ln(x/r)$, $\ln(y/r)$ and $\ln(z/r)$, where x , y and z are the axes of the ellipsoid and r is the cube root of xyz . The scatter diagram so produced could then be contoured to give a shape dispersion of the population of pebbles. In this case the application was to find the pure component of strain in the interior of the pebbles. Sneed and Folk [30] defined the maximum projected sphericity, w_m , as the cube root of c^2/ab , where a , b and c are length, width and thickness respectively. They used this on one axis of a triangular plot, with c/a and $(a-b)/(a-c)$ on the others. Davies [31] suggested adding Wadell's roundness on a vertical axis to give a three dimensional representation of form and roundness features. However, in practice, he simply used a , b and c on the horizontal axes and

roundness on the vertical in a study of abrasive powders. Contours were plotted in two dimensions at various mean roundness values.

Although the idea of representing particle populations on a triangular plot is widely applicable, the choice of parameters for the axes tends to be unique to each application. A poor choice could result in a set of elaborate diagrams giving little or no useful information.

2.3.2 Fourier Analysis

If the outline of a particle profile is "unrolled" the resulting waveform can be analysed. The most usual way to do this is to choose a point within the particle as the origin, for example the centroid, and express the boundary points in polar co-ordinates with respect to this origin. A Fourier series can then be used to represent radius, R , as a function of angle, θ . A true Fourier series has an infinite number of terms, but for computational purposes an appropriate truncation point, N , has to be chosen, and the series is expressed

$$R(\theta) = A_0 + \sum_{n=1}^N (a_n \cos n\theta + b_n \sin n\theta) \dots\dots\dots (1)$$

The number of coefficients that can be calculated is limited by the number of data points on the boundary. Regeneration of the profile from the truncated Fourier series is a good test of its appropriateness. Shape information can then be extracted from the coefficients.

Many authors have explored this form of shape analysis. Schwarcz and Shane [32] continued with the established concept of sphericity and roundness. In two dimensions sphericity became circularity and they defined it as the sum of the squares of the coefficients. Two methods of evaluating roundness, or, more correctly, surface irregularity or roughness, were proposed. The first, m_1 , is based on the degree of fit of approximations of successively higher order and is defined as the number of terms of the Fourier series required to give a fit error less than a prescribed value, the fit error being the root mean square difference between the regenerated profile co-ordinates and the original data. The second measure is the root mean square difference between

a curve defined by half the points and a curve defined by all the points. When tested on plastic particles from various stages of a rounding process these two measures were found to be equally sensitive.

Ehrlich and Weinberg [33] defined a roughness coefficient as the average squared deviation of the profile perimeter from a circle of equal area. This is very similar to the Schwarz and Shane definition of circularity. They considered a modified version of this which allowed selection of a certain range of harmonics, rather than using all of them, and showed how analysis of different ranges could lead to different types of information on sand grains.

Using the relations

$$A_n = \sqrt{a_n^2 + b_n^2} \dots\dots\dots (2)$$

$$\alpha_n = \tan^{-1}(b_n/a_n) \dots\dots\dots (3)$$

a Fourier series can also be expressed

$$R(\theta) = A_0 + \sum_{n=1}^N A_n \cos(n\theta - \alpha_n) \dots\dots\dots (4)$$

where A_n is the amplitude and α_n is the phase angle. Meloy [34] plotted A_n against n on a log-log scale and found that for a wide range of different types of particles there is a simple linear relationship. He proposed three shape parameters associated with this kind of plot - slope, intercept, and scatter about the fitted line.

The amplitude of the tenth harmonic was used by Gotoh et al [35] to characterise the shape of a particle by a fraction of ellipse, α , and a fraction of diamond (i.e \diamond shape), $1-\alpha$. A_{10} is taken from the fitted line of the log-log graph, as plotted by Meloy, and the ratio, k , of the long to the short axis of an equivalent ellipse is calculated. A point is then plotted on a graph of k versus A_{10} which contains contour lines for an ellipse and a diamond. The purpose of this analysis is to give an intuitive description of shape in terms of prescribed forms.

Beddow et al [36] defined a set of morphic descriptors that could be extracted from Fourier series coefficients. The set of amplitude coefficients is divided arbitrarily into three portions and the sums of the lower, intermediate and higher members give values for lumpiness, roughness and texture respectively. Asymmetry is defined as the sum of the absolute values of the phase angles where the corresponding amplitudes are large (that is at least within an order of magnitude of A_0). They also defined the centroid aspect ratio as the maximum dimension through the centroid divided by the dimension perpendicular to it. They then calculated these parameters for atomised copper/lead and sponge iron. Various combinations of pairs of parameters were plotted and it was suggested that a linear decision function to distinguish between the two powders could be developed using visual observation.

Beddow et al [37] discussed the interpretation of the Fourier coefficients and pointed out that a scalene triangle will not necessarily have a notably high value of A_3 . They concluded that it is preferable to regard the coefficients as a set, rather than as individual descriptors.

The Fourier coefficients a_n , b_n and α_n are rotationally variant, which means that the same profile in a different orientation will have a different set of coefficients. Beddow et al [36] defined the orientation by rotating the particles so that the longest axis was at $\theta=0$. This also facilitated the computation of the centroid aspect ratio from the coefficients. Luerkens, Beddow and Vetter [38] later went on to develop a set of morphological Fourier descriptors which are rotationally invariant. Using the second form of the Fourier series (equation 4) the size and shape terms are defined as follows:

$$R_0 = \sqrt{A_0^2 + \frac{1}{2} \sum_{n=1}^N A_n^2} \dots\dots\dots (5)$$

$$L_0 = A_0/R_0 \dots\dots\dots (6)$$

$$L_2(n) = A_n^2/2R_0^2 \dots\dots\dots (7)$$

$$L_3(m, n) = \frac{3}{4R_0^2} (A_m A_n A_{m+n} \cos(\alpha_{m+n} - \alpha_m - \alpha_n)) \dots\dots (8)$$

$$(m + n = 2, 3, 4 \dots N)$$

The size term, R_0 , is the radius of a circle having the same area as the particle profile. L_0 is the size normalised mean radius. $L_2(n)$ is the size normalised inner product of $R(\theta)-A_0$ and $A_n \cos(n\theta-\alpha_n)$, and is related to the second moment about the mean of the radial distribution as follows:

$$\mu_2 = R_0^2 \sum_{n=1}^{\infty} L_2(n) \dots\dots\dots (9)$$

A high value of $L_2(2)$ indicates an elliptical profile, or a profile with a large aspect ratio. A large $L_2(3)$ means the particle has an equilateral triangular profile, while a large $L_2(4)$ suggests a squared or blocky profile. Higher order $L_2(n)$ terms can be interpreted as roughness.

$L_3(m,n)$ is the size normalised inner product of $(R(\theta)-A_0)^2$ and $A_n \cos(n\theta-\alpha_n)$ and is related to the third moment.

$$\mu_3 = R_0^3 \sum_{m=1}^{\infty} \sum_{n=1}^{\infty} L_3(m,n) \dots\dots\dots (10)$$

The particle profile can be regenerated from the size and shape terms. The number of terms needed is the same as the original number of coefficients, but with the advantage of being rotationally invariant.

Swanson and Vetter [39,40] applied this technique to characterise abrasive soil particles and to study the effect of abrasive particle shape on the wear rates of selected steels. They measured roughness as the sum of the $L_2(n)$ terms where $n > 5$. They defined radance as $1-L_0^2$, which is the total variance of the profile from a circle of the same area. Both these parameters successfully distinguished between angular crushed quartz particles and more rounded AFS test sand. They also showed a marked difference between two batches of crushed quartz, ordered to the same specification, which had behaved differently in wear tests.

Rajpal et al [41] studied the relationship between these descriptors and batch sieving behaviour of metal powders. A change in features with sieving time was observed. Morphic descriptors were then used as shape factors in calculating probability of

passage, and sieving curves were drawn. These curves were found to agree with experimental data.

Fourier series expansion of a three-dimensional body was explored by Gotoh and Finney [42]. Using cylindrical co-ordinates, the particle is expressed as a superposition of two-dimensional sections. The resulting coefficients can then be used to approximate the particle by an equivalent ellipsoid with the same volume, surface area and average projected area. Luerkens [43,44] also developed a method of three-dimensional particle representation, based on the morphological variational principle, which states *A mathematical representation of a particle or surface may be derived by finding a normalised boundary function which causes the surface area integral to take on stationary values.* Using the variational principle, the solution for a flat particle, or flake, is the Fourier equation, as discussed previously. For an extended surface the surface height in the z direction can be expressed as a function of θ in a Bessel-Fourier form. This also finds application in texture analysis of images, where surface variation is represented by changes in grey level. Using a spherical co-ordinate system, bulky three-dimensional particles can be represented using a Legendre-Fourier function to express radius as a function of azimuthal and polar angles. Boundary functions have also been developed for fibres and threads using a Tchebycheff-Fourier form for expressing radius as a function of θ and z .

The Luerkens equations form the mathematical basis for a complete characterisation of particle shape, but application is hindered by difficulties in obtaining the three-dimensional data. In practice, most analyses are carried out in two dimensions, using the standard Fourier form.

One of the biggest drawbacks of the Fourier (R,θ) method is the requirement that there is only one value of radius for each angle, which rules out this method for re-entrant particles. Zahn and Roskies [45] used an alternative approach to overcome the problem. Instead of converting x,y pairs to polar co-ordinates, the profile is parameterised by arc length, l , from a starting point to (x,y) , and the angle, $\phi(l)$, between the tangent at the starting point and the tangent at (x,y) . To normalise to the interval $[0,2\pi]$ the function $\phi^*(l)$ was defined :

$$\phi^*(t) = \phi(l) + t \dots\dots\dots (11)$$

where $t = 2\pi l/L$

This function can then be expanded into a Fourier series. Zahn and Roskies used the amplitudes and phase angles to analyse shape symmetries and similarities, experimenting with shape discrimination of numerals from hand-printed character sets. Fong, Beddow, and Vetter [46] compared this method with the (R,θ) method and found that the (ϕ,l) method was superior when it came to regenerating the profile, for both simple and complex profiles.

Luerkens, Beddow, and Vetter [47] proposed a third Fourier method, called the (R,S) method. The co-ordinates of the profile boundary are converted to polar co-ordinates. A Fourier series expansion is used to represent radius as a function of normalised arc length, s , and another Fourier series expansion is used to express the first derivative of the angle with respect to s , as a function of s . As with the other methods, the Fourier coefficients can be reduced to invariant forms and statistical methods can be applied to discriminate or cluster the data. The advantages of the (R,S) method are that it can be used to differentiate between re-entrant and non-re-entrant particles, and that properties such as area, moment of inertia etc. can be calculated analytically. The main disadvantage is the requirement for two Fourier series expansions.

Shibata and Yamaguchi [48] overcame the re-entrant problem by using the x and y co-ordinates instead of the radius and expressing each as a function of i , where $i = 1$ to N for N angular steps around the profile beginning at $\theta=0$. They used half-range Fourier transformations (sine only) and found that $y(i)$ could be expressed with fewer higher harmonics because of its similarity to a sine wave. This prompted them to shift $x(i)$ by $N/4$ (90°) so that $x(1) = 0$ and it would also resemble a sine wave. This significantly reduced the number of harmonics needed for regeneration of the original profile. This method is called the shift x, y co-ordinate function method.

Meloy [49,50] showed how Walsh transforms can be used in a similar way to Fourier functions. The added advantage is that Walsh coefficients represent a series of square waves, so the solution of integrals becomes easier, and physical properties such as

excess surface area can be derived by use of superposition. Other orthogonal functions include the pulse wave Haar transform. This can be applied to a set of x,y,z co-ordinates, typically obtained by taking an SEM image of the fine surface detail using Y modulation.

2.3.3 Fractal Analysis And Polygonal Harmonics

In 1977 Mandelbrot published his book "Fractals: Form, Chance and Dimension" [51], which triggered a whole new approach to the measurement of shape. In the book, Mandelbrot describes how Richardson estimated the length of coastlines by stepping along a map with a pair of dividers and finding that the length estimate, $L(e)$, increases without limit as the step size, e , decreases. A plot (now called a Richardson plot) of $\log L(e)$ against $\log e$ yields a straight line with negative slope. Mandelbrot recognised the significance of this slope and coined the term fractal, where the slope is $1-D$, and D is the fractal dimension of the rugged boundary.

Kaye [52] decided that rugged fine particle profiles have, like coastlines, a sufficient degree of self-similarity to make the concept of fractal dimension a useful one. His initial experiments in manually stepping around profile boundaries showed that rugged fineparticles can exhibit fractal characteristics, with more complex outlines giving a higher value of D . He also described a method based on the intersection frequency of the lines of a grid with the profile. As the grid spacing decreases, more of the profile detail is taken into account. These manual methods are tedious and time-consuming so Kaye made some suggestions for automating them. He proposed using coupled light pens on a computer screen for the hand-and-dividers technique, and line scan logic for the grid technique [53].

This encouraged other workers to explore computer-based techniques. Using digital images a sequence of discrete boundary points can be obtained, and various algorithms for stepping along these points were quickly developed. An exact method requires an iterative process to test each point until the step length is exceeded and then find the exact position by interpolation. Schwarz and Exner [54] simply took every n th point along the profile and calculated the distances between them. The sum

of these distances (plus the length required to close the polygon) gave the perimeter estimate, and the average distance gave the equivalent step length. Clark [55] preferred to find the discrete point closest to the step length from the previous point, calculate the distance, and then obtain the perimeter and average step length as in the Schwarz and Exner method. He called this the hybrid method and referred to the Schwarz and Exner method as the FAST method.

Normand and Peleg [56] showed that the Richardson plot can be constructed directly by counting the number of edge pixels at different resolutions. An SEM micrograph of an agglomerated instant coffee particle was digitised and the variation in resolution was then achieved by averaging blocks of pixel grey-level values. The results agreed with published data on instant coffee from other methods.

Kaye [57] compared fractal analysis with Fourier analysis by constructing Richardson plots for profiles which had been regenerated from finite Fourier series. The profiles which were regenerated with fewer harmonics showed Euclidean regions (ideal smooth curved shapes give a flat Richardson plot). As more harmonics were added, the break point between Euclidean and fractal portions of the graph occurred at smaller step lengths. Kaye suggested that, as a profile becomes more rugged, the number of harmonics required to describe the ruggedness increases exponentially.

Because many stereological measurements are affected by the resolution at which they are measured, Flook [58] suggested that a fractal plot should be drawn first, to determine whether the structure exhibits fractal behaviour over the range of resolution being used. Fractal plots may also be used to adjust data obtained at different resolutions.

A different approach is to use dilation logic, now available on most image analysis systems. This method is based on a technique used by the mathematician, Cantor, to tame non-differentiable curves. Each point along the curve is replaced by a disc of radius r , giving a path of width $2r$. The area of the path divided by the width gives an estimate of the length of the curve. The length estimate decreases with increasing r . As before, the fractal dimension can be obtained from a plot of $\log L$ versus r . Flook

[59] employed this method using an octagonal dilation element on a commercially available image analysis instrument.

An improvement on sequential dilations is the use of the distance transfer function. This image analysis function assigns to each pixel within a defined area a value representing the distance to the nearest edge pixel. The result is a series of contours corresponding to different radii of dilation. The area occupied at a chosen dilation radius corresponds to the number of pixels with values equal to or less than that radius. The advantage is that this is a circular dilation. Adler and Hancock [60] proved this method to be faster than sequential dilation and also suggested a correction to compensate for overlaying the dilation on an orthogonal grid.

There are many pitfalls in fractal analysis and none of the techniques discussed here has overcome them all. Different methods give different results. Results can be greatly influenced by choice of starting point. The range of resolution (step length, grid spacing, width of dilation element etc.) is limited by digitisation at one end of the scale and by the size of the image at the other. At large step lengths there is the problem of closing the polygon with a smaller step. Many real particles can be "semifractal" or "multifractal" - terms coined by Kaye to describe cases where the Richardson plot is linear in segments only. In short, anyone choosing to calculate the fractal dimension of a profile will have many decisions to make, all affecting the final result. Graf [61] gave some recommendations on resolution limits and the presentation of Richardson plots. Wright and Karlsson [62] compared three of the methods and arrived at some fairly bleak conclusions about the whole idea of using fractal dimension as a characterisation parameter. Orford and Whalley [63] discussed the problem of locating the two (or more) linear regions on the Richardson plot. In studying biological objects, Rigaut [64] found that he was getting upper convex plots and derived empirically a new mathematical formulation to fit his data. He questions the wisdom of fitting straight lines rather than accepting a continuously varying fractal dimension.

Allen, Brown and Miles [65] reviewed the documented techniques for measuring boundary fractal dimensions and concluded that *ultimately the best fractal analysis*

method is that which is both suited to the computational facilities available and provides results of sufficient accuracy. They felt that most inaccuracies result from poor use of the methods rather than poor choice of method. They also gave some recommendations for authors so that published results from different techniques could be compared more easily.

Given that there are difficulties associated with all methods of shape measurement, these problems do not make fractal analysis any less attractive and it continues to gain momentum and produce off-shoots, one of which is the use of shape descriptors based on fractal harmonics, also called **polygonal harmonics**. Clark [66] pointed out that fractal analysis cannot describe reliably the macroscopic particle shape, and introduced the idea of describing the ability to construct within the profile two diametrically opposed points (2nd harmonic), equilateral triangles (3rd harmonic), rhombuses (4th harmonic) etc., within certain geometric constraints. These are simple harmonics, and exist if a sequence of steps around the boundary produces a closed polygon with all sides equal to the step length. Complex harmonics are those which require more than one traverse of the edge to achieve closure. Clark noted that the range of step lengths over which a particular harmonic exists is related to particle shape and he defined the persistence of a harmonic as the ratio of the upper value of step length to the lower value of step length for the existence of that particular harmonic. Reilly and Clark [67] measured persistences of the second to sixth harmonics, and the ruggedness of the boundary, for a variety of shapes, including some computer-generated shapes. They also carried out Fourier analysis on some of the objects and compared persistences with the Fourier coefficients. There was no clear relationship between them. Clark, Gabriele, and Shuker [68] found that the persistence of the sum of the second harmonics of three views of the particle correlated with the drag coefficient for pebbles and gravel settling in water.

Young et al [69] observed that, for complex shapes, harmonics can exist for a range of step lengths, then disappear and then prevail again for a while, with occasional jumps to complex harmonics. Thus, a particular harmonic might not exist exclusively over its full range. This causes difficulties in measuring persistence so Young et al

suggested organising the data into a distribution of harmonics over a defined range of step lengths, and identifying those harmonics that have a high probability of occurring. Since the choice of starting point can affect the results, the distributions of harmonics at twenty equally-spaced points on the particle boundary were calculated and averaged. This characterisation scheme was applied to synthetic fractal shapes and real adsorbent particles. For the fractal particles it was found to give a good description of macroscopic shape, as well as being sensitive to subtle shape details. The results for real particles proved to be much more complex, but the technique still provided an acceptable shape analysis.

Maeder and Clark [70] later refined the idea of persistence of a harmonic to give a new shape descriptor - harmonic endurance. This places more weight on low order harmonics and factors out the impurity of high order and complex harmonics within the ranges.

Another technique which involves stepping around the boundary of a profile is Piper's shape analysis technique [71]. Each step is seen as a vector and the angle between each vector and the next is recorded. A frequency plot of the distribution of angles provides an indication of the roughness of the profile. Pickett, Clark and Shuker [72] adapted this technique. Having found the first angle, they used the same step length to find another angle starting at the next point after the starting point. This is repeated so that every point is used in the analysis and there is no dependence on choice of starting point. By analysing a wide range of shapes in this manner they demonstrated how measured roughness varies with step length, and how a plot of average angle versus step length gives information on the variation of roughness over a range of scales.

A variation on Piper's analysis is Delta analysis, proposed by Clark and Meloy [73]. They chose to find the angles between two vectors separated by a small distance. A frequency plot over the range of angles measured helps to distinguish between particles of different roughness. By varying the distance between the lead vector and the following vector, the roundness of the fine structure on the particle edge can be measured.

2.3.4 Other Methods

Several other innovative methods of shape characterisation that have been reported in the literature are worth mentioning. Kaye et al [74] showed how a facet signature waveform can be generated by plotting the length of chord spanning a particular number of points of a profile boundary against the starting point of the chord. Corners on the profile are represented by dips on the graph, giving a measure of sharpness. Beresford and Lloyd [75] also developed a corner counting method. It was based on the radius of curvature of the profile at various angles. Plots of the radius of curvature against angle showed the corners as troughs. Since diamond particles have a faceted surface, and therefore have corners, these two corner counting methods are interesting and are explored further in Chapter 3.

Kaye [76] has also suggested the use of Feret diameter signature waveform as a shape characterisation parameter. The waveform is obtained by plotting the projected diameter in a given direction against angle as a particle is rotated about a selected pivot point.

Kaye, Naylor and co-workers [77] attempted shape characterisation using optical technology. In Shape Analysis by Diffraction Originated Waveform (SHADOW) the silhouette of a particle is used to generate a Fraunhofer diffraction pattern using laser light. A wave is generated by rotating a disc, from which a V-shaped sector has been cut, in front of a photocell. This wave is treated as the signature waveform for the description of the particle.

Clark, Reid, and Kaye [78] used laser diffraction to measure an asymmetry factor on aerosol particles. They developed an instrument similar to those used for particle sizing, but separated the scattered light so that both size and shape could be measured. They then compared results from spheroidal iron oxide particles, with size and aspect ratio obtained by image analysis. The results were significantly different, with the light scattering method giving broader distributions in both cases. This was explained by inappropriate calibration of the diffraction instrument, and the fact that the

particles were presented to the laser beam in random orientation as opposed to stable orientation for image analysis.

Staniforth and Rees [79] developed a shape factor, *shah*, designed specifically for re-entrant particles. It is calculated as the number of downward pointing projections, e , in a sample set of particles, divided by the number of particles, n , in the sample. Since *shah* gives no indication of the basic geometric form of the particles, Staniforth and Rees [80] combined it with the Heywood shape factor, f/k , where f is the volume coefficient and k is the surface coefficient. They drew up a schematic combination diagram, which gives an intuitive representation of shape according to the combination of measurements.

Meloy [81,82] studied particles resulting from fracture of brittle materials and proposed a particle characterisation scheme based on counts of faces, edges, and points. He derived three simple equations relating these numbers, and giving a frequency distribution of the sizes of the faces.

Bandemer and Kraut [83] showed how fuzzy theory can be applied to shape analysis of a quartz particle. From a greyscale image a sympathy function with respect to a suitable family of planar shapes is computed.

If particles in a sample from a population are characterised in terms of p parameters then each particle can be represented as a point in p -dimensional feature space. Cluster algorithms or discrimination algorithms can then be used to analyse the data. An example of this type of analysis is given by Heidenreich and Muller [84] in an investigation of the flowability of wheat and oats. Bonifazi and colleagues used pattern recognition techniques to classify mineral particles [85,86]. This leads on to the possibility of using artificial intelligence techniques to see if table sorted diamond can be classified with combinations of shape factors. Chapter 5 details the application of an expert system and a neural network.

2.4 A REVIEW OF SHAPE ANALYSIS OF DIAMOND

The preceding sections gave an overview of the possibilities for shape measurement in general but work has also been carried out specifically for diamond particles. This section summarises past efforts by De Beers and others to quantify diamond shape.

Custers and Raal [87] described a method of calculating average volume shape factors of diamond grit samples. The total projected area of a known number of particles was measured by photo extinction, and the mean projected diameter, d , of the sample was calculated. The sample was then weighed and the average volume, V , was calculated from the mass, density, and number of particles. Heywood's volume shape factor, V/d^3 , was then found.

A simple visual classification scheme, called the Shape Count method was developed for natural industrial diamonds by Dyer in 1952. Particles were assigned to one of four classes - blocky, less blocky, needle-like, and flats and needles. These classes had values 1 to 4 respectively, and an average value for a sample could be found. Dyer and Wedepohl [88] further developed this method into the Utility Index method. This involved making triaxial measurements and expressing each of the two shorter dimensions as fractions of the longest. A plot of one fraction against the other was divided into ten zones, indexed 1 to 10, the index of a zone denoting the usefulness of a particle for a particular grinding operation. The mean index for a sample could then be calculated. In practice the method was time-consuming so operators were trained to assign indices on sight.

Bakon and Szymanski [89] studied the crystal habit/internal structure, and surface structure of synthetic diamond from five different manufacturers, including De Beers, and presented a qualitative morphological classification in 1982. Both optical and scanning electron microscopes were used. This classification was intended as a guide for toolmakers for selecting appropriate diamond abrasives. De Beers saw grits generally came under the headings of regular monocrystals, or uneven monocrystals, with flat, smooth faces or flat, rough faces.

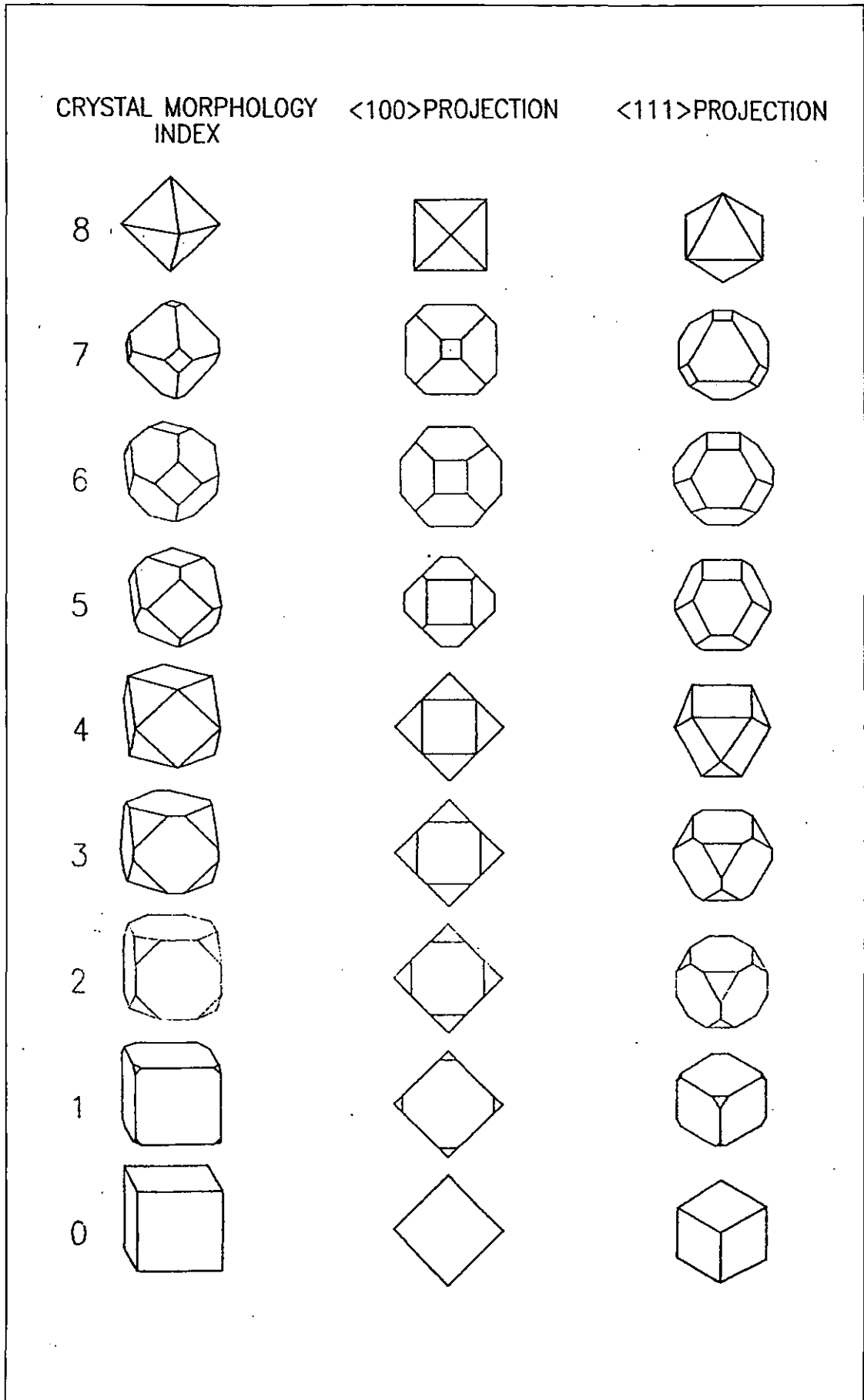
The scanning electron microscope (SEM) can be used for crystal morphology studies. The angles between planes lying in the zone defined by the direction of the electron beam can be determined from the secondary electron image by measuring the angles between their straight-line projections. A goniometer facilitates alignment of the crystals. Addition of a cathodoluminescence detector allows differentiation of the $\{100\}$ and $\{111\}$ faces. Cathodoluminescence is light emitted when a fast moving electron strikes a dense material. Woods and Lang [90] have shown that the growth sectors in synthetic diamond cathodoluminesce in this way. The $\{100\}$ faces appear green and the $\{111\}$ faces appear deep red. Cathodoluminescence of diamond is concisely reviewed by Davies [91]. Pipkin [92] studied the morphologies of a number of interesting crystals (macles, twins, and irregular crystals) using SEM techniques. These are very useful techniques for research applications, but require a high degree of skill and interpretation, and are more qualitative than quantitative.

Returning to more simple techniques, *Figure 2.1* shows a shape characterisation scheme for synthetic diamond developed by De Beers. It is based on ideal forms of cubo-octahedron. Shape 4 is a regular cubo-octahedron with all edges of equal length. Higher numbers signify preferential growth on the $\{100\}$ faces, resulting in a domination of $\{111\}$ faces, and a graduation towards an octahedron (shape 8). Lower numbers show greater tendency towards a cube, with 0 being a perfect cube. Attempts have been made to use this numbering system to characterise diamond samples. The sample is examined under a microscope and each individual crystal is assigned a number. The numbers are averaged to give an average morphology number for the sample. Particles which do not fit into any of the classes are noted as unassigned and the proportion of unassigned particles is quoted as part of the result. The standard deviation of the distribution of classes gives an indication of the spread of shapes within the sample.

The obvious problems with this scheme are :

- ♦ it is a slow and tedious operation,
- ♦ ideal shapes are rare in practice so classification is very subjective,

Figure 2.1 : Synthetic diamond morphology index



- a large proportion of unassigned particles renders the average morphology number meaningless.

GE (General Electric) Superabrasives, manufacturers of synthetic diamond, recently published details of a similar characterisation scheme, which has been automated using image analysis [93,94]. They define a shape property, tau (see *Figure 2.2*), which is 0 for an octahedron and 1 for

a cube, with a continuous range in between for intermediate shapes. The image analysis algorithm fits templates to the inner and outer outlines of a crystal to determine the value of tau. Standard shape parameters, circularity and aspect ratio, are used to characterise those crystals which do not conform to the

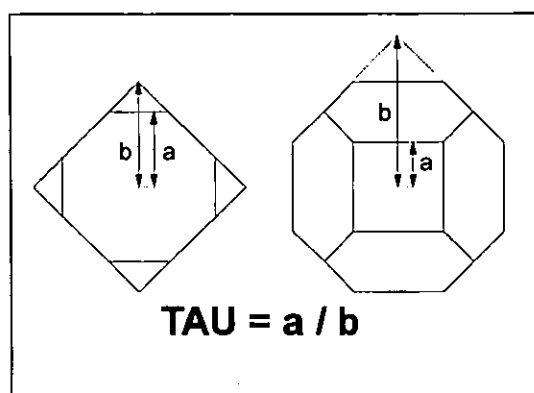


Figure 2.2 : Definition of GE's tau

regular cubo-octahedral structure. The average greyscale value, normalised by the background grey-level, gives a measure of the clarity of the crystals. Clarity is a function of light-scattering inclusions, defects, and surface roughness, all of which may contribute to a particle's performance.

Dubious claims are made for this method of analysis. The benefits quoted are [93]: the ability to better sort and classify products, the ability to develop products with narrower shape ranges, the ability to test and match specific shapes to specific applications. The practicalities must be questioned, however, because sorting diamond grit by measurement of individual particles would be time consuming and expensive. Even using sampling, the number of particles suggested [94] is 300, and at time of publication these were being analysed 25 at a time.

Of course, arguments like these will apply to all forms of individual particle analysis and it is impractical to suggest any such method for use in the production of synthetic diamond, given that batches can contain millions of carats (5 carats=1 gram). However, quantitative analysis of samples can be very useful for comparing batches,

comparing competitor products, optimisation of tabling parameters, and studying the relationship between shape and other properties.

2.5 SUMMARY

The trend in shape measurement over the last sixty years or so has been to move away from tedious mechanical methods and take advantage of every development in computer hardware and software, cameras, lasers, and digital technology. From crude triaxial measurements of pebbles, to tracing enlarged silhouettes with a digitiser, to scanning a photograph into a computer, it is now a trivial matter to obtain a live image of a population of particles on a computer screen. Complex mathematical manipulations can be performed in a fraction of a second at the click of a button.

The increasing ease of acquiring data, and the increasing speed of processing it, have led research away from the concept of shape factors and sphericity to less intuitive methods, and the use of cameras for obtaining images has concentrated the effort on two-dimensional analysis. It could be argued that these are regressive steps, and that techniques like Fourier analysis and polygonal harmonics do not provide parameters that are any more useful than a simple measurement of roundness. More emphasis needs to be placed on application of new methods, and their practical relevance for real particle problems. There is a danger of being seduced by interesting mathematical theories and principles and losing sight of the main objective - which is to find meaningful and practical methods of characterising shape. It is also important that shape separation techniques continue to develop in parallel with shape analysis methods.

The future of shape analysis appears to lie in imaging, and it is possible that image analysis instruments will soon include a cybernetic means of physical separation of particles based on the measurements. Shape will remain an important part of particle technology because so many other particle characteristics are influenced by it. It is unlikely, however, that a neat solution, which covers a wide range of applications, will be found. Instead, techniques will become more application-specific as they are refined.

Many of the papers in the literature use particles that differ vastly in shape, to illustrate that methods work. There is little doubt that all of the methods discussed in this chapter could successfully tell the difference between diamond and, say, angular silicon carbide particles. The differences in shape between a diamond sample and another diamond sample are much more subtle and this is why there is a need for application-specific solutions. Some of the methods will be better than others at detecting shape differences within a narrow range for a certain type of material.

The first objective in this thesis is to find those methods that are suitable for characterising diamond.

3 MEASURING THE SHAPE OF DIAMOND

It is clear from the literature review that there are many and varied methods of quantifying shape so it is necessary to eliminate some of the options. Since large numbers of particles will be involved the method cannot be too tedious or time consuming. This rules out triaxial measurements and favours two-dimensional analysis, preferably letting a computer do most of the work. Most image analysis packages can measure shape factors such as roundness and aspect ratio so these can be explored easily. Fourier and fractal analysis can also be investigated once the co-ordinates of the particle boundary are available. Again image analysis packages will provide the starting data.

In this chapter the search for a shape measurement method appropriate to diamond will concentrate on the following areas:

- ♦ 2-D shape factors,
- ♦ Fourier analysis of the boundary co-ordinates,
- ♦ fractal analysis,
- ♦ counting corners.

Some of the advantages and disadvantages of these options have been mentioned in the literature review. Others will come to light as the work progresses.

3.1 IMAGE ANALYSIS

3.1.1 Description Of Equipment

Since all of the methods to be explored require a digital image as a starting point the first step was to set up an image capture system. A review of the market revealed that there were two main types of system on offer. One was a dedicated image analysis instrument, for example the Quantimet 570 from Cambridge Instruments. This controls all the stages from image capture to reporting of results, using hardware to handle much of the processing in real time. Such an instrument would be needed if speed were critical (for example in automation of routine tasks), but was too

expensive to be considered for a research project. At the other end of the scale was the PC-based system. Many companies were offering frame-grabbers and image analysis software for a few thousand pounds. A frame-grabber is a piece of hardware that samples an analogue video signal and converts it into an array of data points that can be stored digitally. It can be inserted into an expansion slot in a PC and software mathematical algorithms can then be used to enhance and process the digital image.

A chalnicon tube scanning camera and a Wild M3Z trinocular microscope with camera adapter were salvaged from an obsolete application and a 486 PC was available so it was not difficult to add a frame-grabber and software to make this into an image analysis system. After considering the possibilities the Vision-EZ frame-grabber and Global Lab Image software package, both from Data Translation, were chosen as a low-cost option with all the required basic functions. The software allows display on the computer monitor of both the image and the menus but this was found to be cumbersome and a Sony analogue monitor for separate display of the image was added later.

Synthetic diamonds have a degree of transparency to white light and their flat faces are highly reflective. For the purposes of inspection and quality control they are viewed under low magnification with a stereomicroscope. The particles are scattered in a petri dish and illuminated from above at an angle. Black, white or red backgrounds are used, depending on the attributes being examined. Similar conditions were tried for camera imaging but it was found that reflected light is not suitable because of the shine from reflecting faces. Transmitted light is better because the angled faces appear dark, while the background and co-planar faces are bright. This means the particle outlines can be identified and the shape of the top face can be analysed, if required. Diffused light from a fluorescent lightbox gave the best results.

The complete system is shown in *Figure 3.1*, comprising of a lightbox, a microscope, a camera, a computer with frame-grabber and software, an analogue monitor, and a printer.

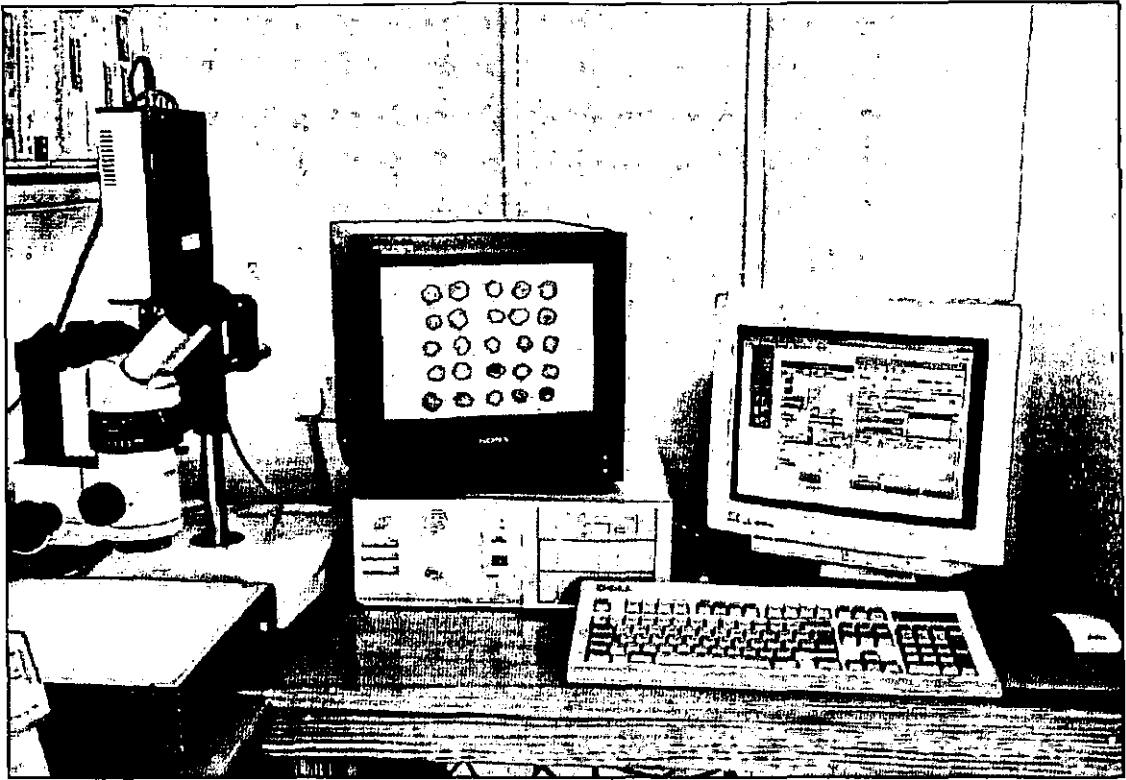


Figure 3.1 : Image analysis equipment

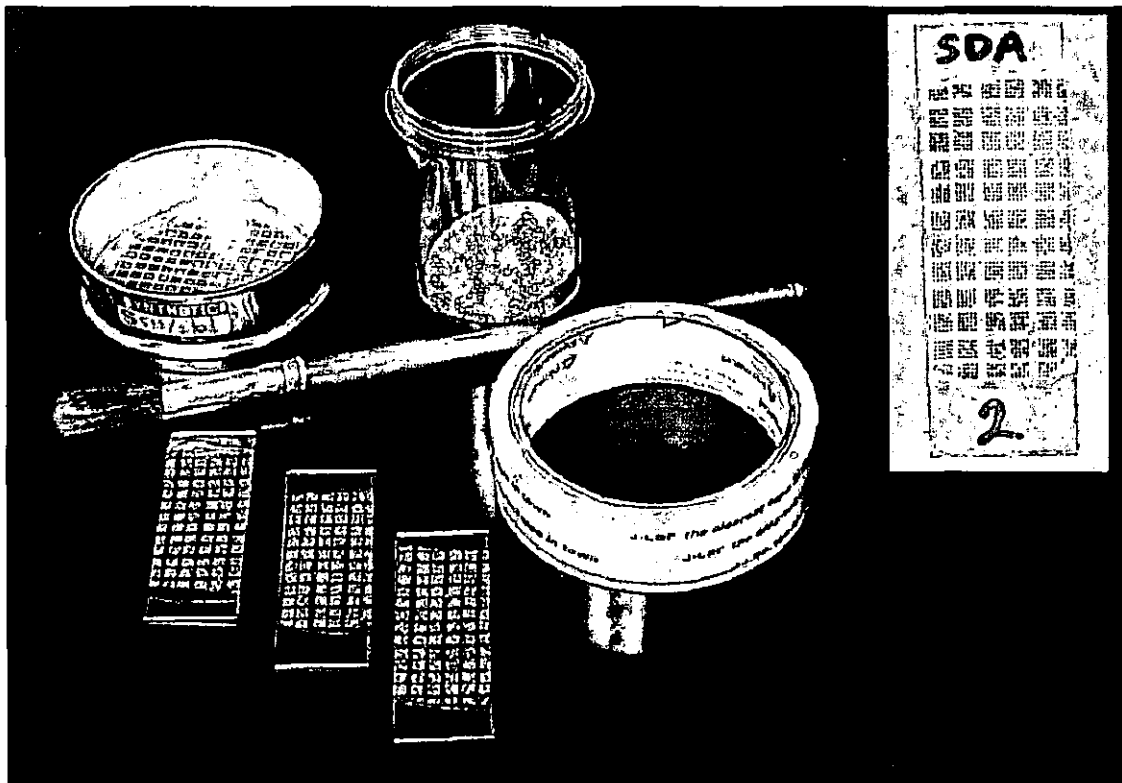


Figure 3.2 : Prepared slides

3.1.2 Sample Preparation

The quickest and easiest way to prepare a sample for analysis is to scatter a few carats¹ into a petri dish, but with this method it is impossible to avoid having particles touching each other. This means relying on the operation of software segregation algorithms, which are not always successful. To get around this problem a De Beers technique for separating particles was modified. It uses an electroformed sieve with apertures just large enough to allow all the particles through. A strip of clear sellotape (trade name J-Lar) is stuck to the underside of the sieve. The diamonds are poured into the sieve and brushed across the taped region, where they stick, separated by the wire grid. Excess particles are shaken out, the tape is peeled off and placed, diamond side up, on a glass microscope slide. A second piece of tape is used to cover the particles and protect the exposed sticky areas from dust. The result is an array of particles, separated from each other and nicely arranged in groups. The method is reasonably quick and straightforward and removes some of the difficulties in processing the image later. The choice of sieve aperture size is important because the apertures must be large enough to allow any particle through and so avoid discrimination but small enough so that two particles will not fit in one aperture. For size 40/45 grits, it was found that a 522 μm sieve with octagonal apertures gave the best results of all available sieves. (522 μm is the nominal diameter of the inscribed circle in these octagonal apertures.) Some prepared slides are shown in *Figure 3.2*.

Slides with regularly spaced sticky patches can be purchased to provide a faster and neater way of achieving good separation. They are called tacky dot slides and come in a range of dot sizes and spacings [95]. T. Allen [96] describes how they can be used in an application where the weight of a known number of particles is required. Slides with 150 μm diameter dots spaced at 1,000 μm centre to centre were tried with 40/45 diamond particles (diameters approximately 500 μm). Double occupancy of dots was found to be a problem and the wide spacing meant few particles in the field of view at the chosen magnification. Consequently, the sieve and tape method was preferred.

¹ Diamonds are usually weighed in carats. 5 carats = 1 gram

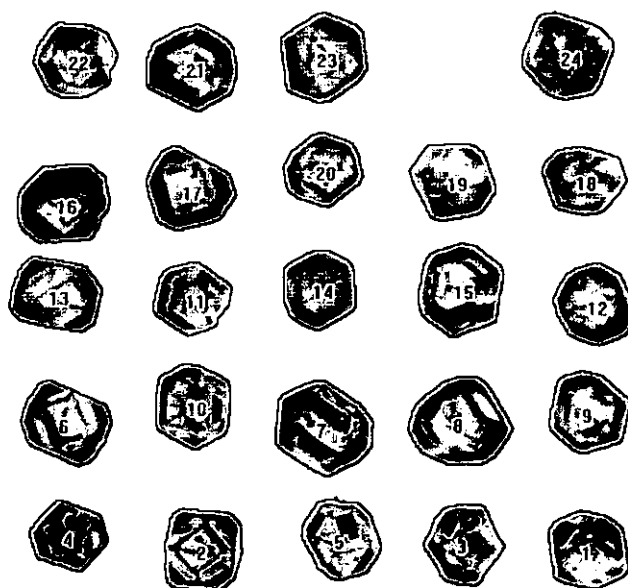
3.1.3 Image Capture And Analysis

The slide is placed directly onto the lightbox and a real time image appears on the analogue monitor. Magnification and focus are adjusted on the microscope to give a clear picture of a group of particles. For size 40/45 the particles are grouped in blocks of 25 (the blocks are defined by the supporting grid on the sieve) and a magnification of x16 means that a 5x5 array of particles fills the field of view. All analysis reported here was carried out at x16 magnification.

Contrast and brightness can be adjusted from within the image analysis software. The digitised image has a range of grey-levels from 0 to 255, where 0 is black and 255 is white. With transmitted light the background is white and the particles contain various shades of grey. A grey-level threshold must be set so that particles can be distinguished from the background. In most cases a value of 200 works. The software identifies sets of connected pixels which have grey-level values between 0 and 200 and which have neighbours with grey-levels greater than 200. These sets are the particle outlines. *Figure 3.3* shows an example of an image and particle identification.

The software offers a range of parameters calculated from the co-ordinates of the outlines. The user selects some or all of these to be reported and then chooses the

Figure 3.3 : Image of diamond particles with particle outlining



'*Find Particles*' option. The software identifies the particles, and outlines and numbers them on the monitor. This enables the user to check for errors, such as two particles being identified as one. A list of the selected parameters is presented with values for each numbered particle and statistics for the field. All reported data can be stored in a file.

To analyse more particles the slide is moved by hand to reveal the next block of particles and the '*Find Particles*' button is pressed again. The new data can be appended to the file. This process is repeated until the required number of particles has been analysed. Since there is no facility in the software to work with or graph the data, the data file is imported to a spreadsheet for further manipulation.

Once the sample preparation, image capture, and data storage techniques were in place the next step was to provide some diamond particles to work with. A sample of bulk 40/45 SDA material was tabled such that it spread more or less evenly into twelve bins. Samples were taken from each of the bins and slides were prepared.

3.2 2-D SHAPE FACTORS

3.2.1 Identification Of Relevant Shape Factors

The software package offers 56 parameters. These were assessed to identify those that could be used to describe tabled grit in a way that is both meaningful and relevant. Some parameters could be eliminated immediately, for example those that are orientation dependent, such as the angle between the major axis of the particle and the x -axis, or those that depend on the position of a particle in the field, such as the x and y co-ordinates of the centroid, leaving approximately twenty parameters to be investigated. Examples are perimeter, roundness, area, maximum radius, average radius and average grey-level.

By default the unit of length used by the software is the pixel. To calibrate the system for actual length in microns a graticule can be viewed at the required magnification and the software calculates a conversion factor. Since SDA had not been analysed particle by particle in this way before, the system was calibrated to give actual

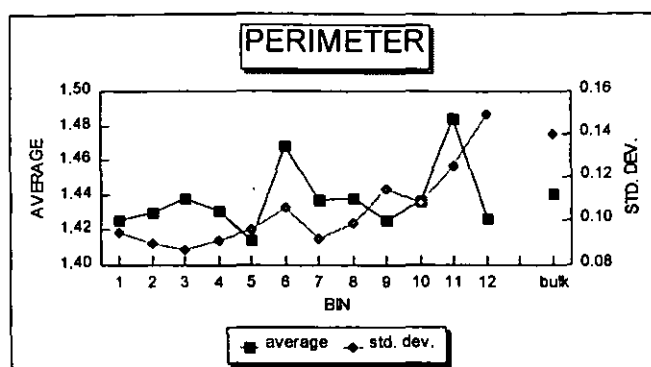


Figure 3.4

Variation of perimeter with bin number

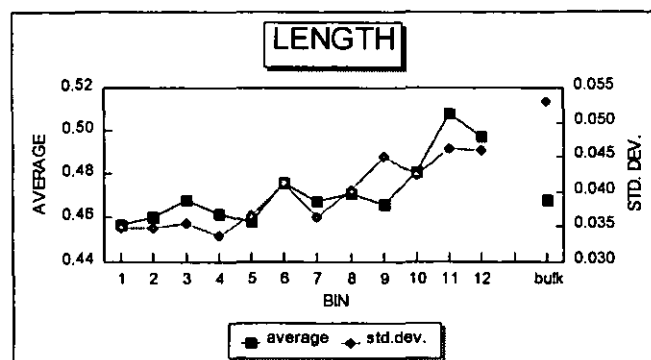


Figure 3.5

Variation of length with bin number

dimensions rather than pixel counts. At x16 magnification one pixel was found to be equivalent to $6.9\mu\text{m}$. Of course, for dimensionless shape factors this calibration will not affect the results.

100 particles from each of these slides were analysed and the results for all of the potentially interesting parameters were recorded. Graphs of average and standard deviation versus bin number were plotted and examined. Some parameters varied randomly across the bins, for example the perimeter (*Figure 3.4*). These were discarded immediately. Others showed an overall trend but not a smooth one, for example length (*Figure 3.5*). A few displayed a smooth curve with a gradual change from bin 1 to the middle bins and then a more pronounced change in the upper bins. These parameters were:

- roundness - defined as $4\pi A/P^2$, where P is the perimeter and A the area,
- radius ratio - the minimum radius divided by the maximum radius, where radius is measured from the centre of area to the perimeter,
- axis ratio - the ratio of the minor axis to the major axis of an ellipse having the same second moments of area as the particle,

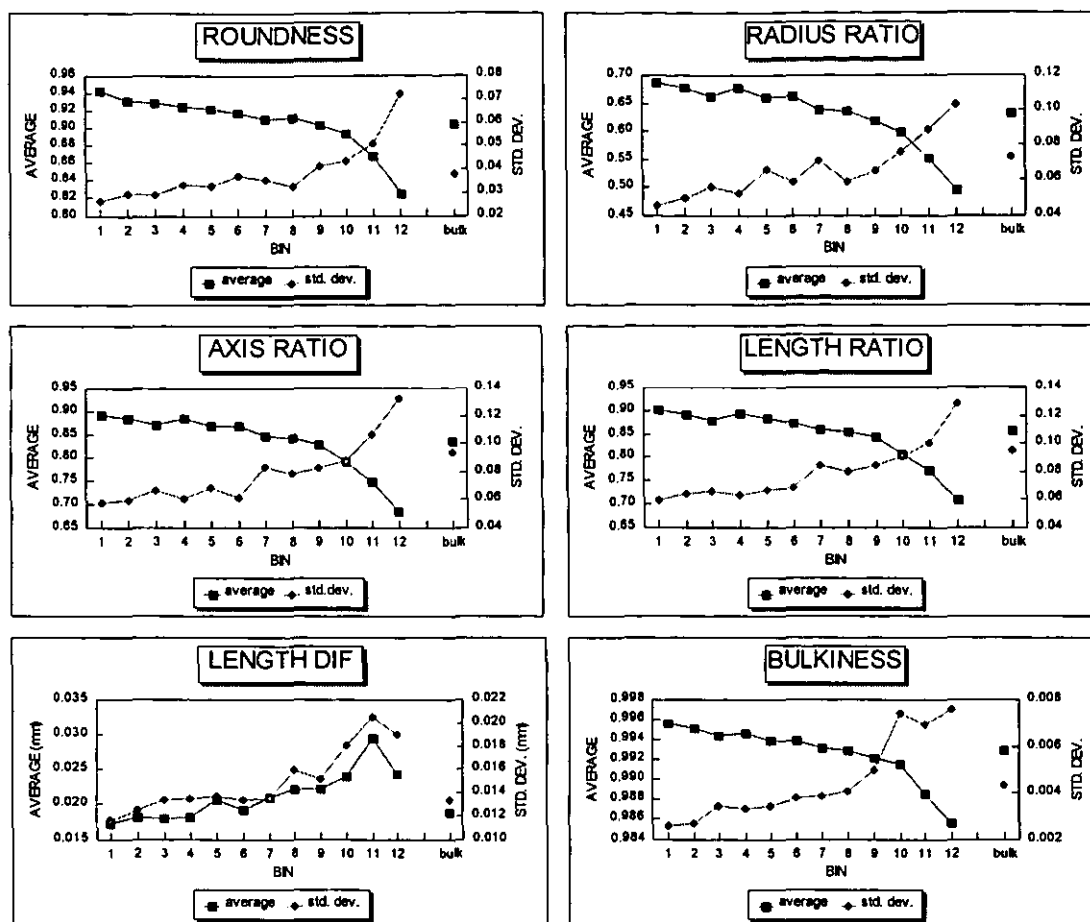


Figure 3.6 : Six parameters showing trends with bin number

- ♦ length ratio - the width divided by the length, where width and length are those of the bounding box oriented along the major axis,
- ♦ length dif - a measure of symmetry computed as the distance along the major axis from the centre of the bounding box to the centre of area.

The associated plots are shown in *Figure 3.6*. Of these, roundness showed the smoothest relationship with bin number. The shape that has the minimum perimeter for a given area is a circle, which has a roundness of 1. All other shapes have roundness less than 1. The reciprocal of roundness is commonly called circularity.

The three ratio parameters represent slightly different aspects of particle shape. The radius ratio gives a measure of deviation from a circle. A circle has the maximum allowed ratio of 1 and a square has a lower ratio. The radius ratio is also low if there are large concavities and/or protrusions on the particle outline. Image capture or

digitisation errors, or errors in determining the particle outline, could add spikes and thus influence the radius ratio.

Axis ratio is clearly defined using an ellipse for comparison and is based on the well-understood concept of moments of area from rigid body dynamics. It gives a measure of elongation and of symmetry. A maximum value of 1 implies symmetry about the principal axes. Blocky particles have high axis ratios and elongated particles have low axis ratios. It is the reciprocal of Medalia's anisometry [28] which he found to be a good general descriptor for both simple and complex shapes, especially when bulkiness is also measured. Bulkiness was defined by Medalia as the ratio of the area of the equivalent ellipse to the projected area of the particle. It can be derived from major axis, minor axis and area, and is included in *Figure 3.6*.

$$\text{bulkiness} = \frac{\frac{\pi}{4} \times \text{major axis} \times \text{minor axis}}{\text{area}} \dots\dots\dots (12)$$

Length ratio is a form of aspect ratio derived by enclosing the entire particle in a box oriented on the axes of the equivalent ellipse. It becomes less useful as shapes become more complex. As with radius ratio, protrusions will influence the results, so small image capture errors could have large effects on the length ratio.

Length dif gives a measure of symmetry. A value of 0 means the particle is symmetric about its minor axis. From the analysis carried out so far the range for length dif is approximately 0 to 12 pixels or 0 to 80 μm for the particles being studied.

It was decided to dismiss two of the three ratio parameters. Radius ratio and length ratio were rejected in favour of axis ratio, the latter being the most promising of the three because it is less dependent on accuracy of digitisation. This left four parameters thought to be worthy of further investigation - roundness, axis ratio, bulkiness and length dif.

Plotting distributions rather than averages gives a better indication of the overlaps between the bins. The cumulative undersize graphs in *Figure 3.7* suggest that roundness is the parameter that best describes the shape fractions, since it shows the least overlap.

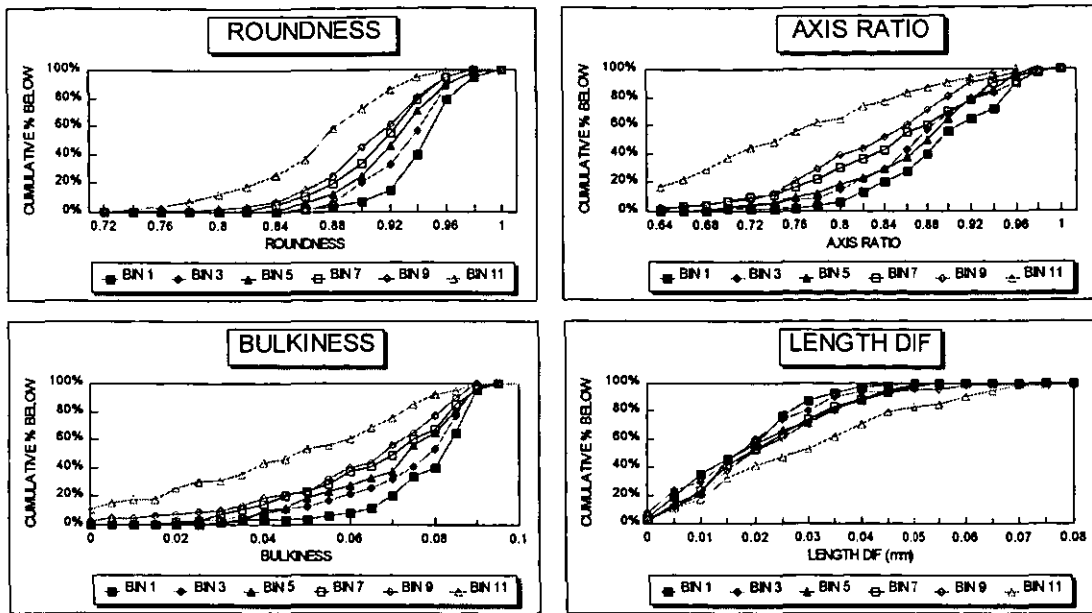


Figure 3.7 : Cumulative distributions

Since it is hoped that the chosen shape factor will relate not only to behaviour on a sorting table but also to behaviour in sawing applications it is a requirement that the shape factor would show some correlation with grit properties perceived to be shape related. Diamond particles in a saw blade must break down in a controlled manner so that fresh cutting edges are generated and an adequate protrusion from the bond is maintained. Holding is usually mechanical rather than chemical so shape and surface texture are important but the dominant factor is the friability or, in other words, the strength of the diamond particles. The choice of grit for an application is usually based on size and strength, taking into account the workpiece material and the compatibility of the metal bond in terms of its abrasion resistance.

In general, crystals from the good shape end of the table have a higher resistance to fracture under load than poorly shaped crystals which are easily stressed by point loading. Strength is certainly the most important shape-related property and to some extent table sorting gives strength classes as well as shape classes. However, strength is a complex issue, as will be discussed in the next section.

3.2.2 Relationship Between Shape Factors And Strength

The strength of synthetic diamond can be quantified by subjecting a sample to an impact crushing test and expressing the weight of unbroken crystals as a percentage of

the original weight. The test is called the *Friatest*. A known weight of diamond is vibrated with a hardened steel ball in a hardened steel capsule under controlled conditions and then the diamond is sieved to separate the broken from the unbroken crystals. The percentage by weight retained on the sieve is called *UB*. Stronger products have higher *UB* values. The specifications for *UB* play an important role in the processing of sawgrits and Friatest strength is considered to be an important characteristic of the final products.

The impact strength of a single particle is influenced by its:

- size,
- shape,
- non-diamond inclusions,
- surface texture.

For a collection of particles the distribution of these properties will determine the results of the crushing test. Size is taken into account by specifying the sieves to use for each grit size before and after crushing, and comparing only grits of the same size. In general, for any given sawgrit product *UB* increases as size decreases.

Non-diamond inclusions act as weaknesses in the particle structure, causing stress points for crack initiation. Most of the inclusions are the solvent/catalyst metals used in synthesis. Their magnetic properties can be exploited to obtain a measure of the amount of included metal. The magnetic measurement parameter is called *M* and is related to the magnetic susceptibility of the sample.

It is known that surface texture and, in particular, surface flaws such as cracks, have some influence on the way an individual diamond particle will break. At present there are no established means for quantifying this effect and it is usually assumed when dealing with a collection of particles that the average surface effect is less significant than the other factors. Since it is beyond the scope of this project to find a surface texture measurement, the same assumptions will be made here.

Within a given size, such as 40/45, this leaves shape and inclusions as the main quantifiable factors contributing to the strength of a sawgrit. An investigation of the relationship between shape and strength will therefore have to take magnetic properties into account.

Thirty-three samples were taken from various lots of material after shape sorting. Based on measurement of the magnetic parameter, M , each sample was assigned to one of four magnetic categories, which will be called $M1$, $M2$, $M3$ and $M4$, where $M4$ is the most magnetic. The shape parameters of interest were measured by image analysis and the averages for 100 particles were obtained for each sample. The strength values, UB , were estimated from a knowledge of the specifications for the products.¹

The shape averages are plotted against UB in *Figure 3.8*. All four parameters show a trend with increasing strength but the clearest relationship within magnetic fraction is seen in the axis ratio plot. A linear regression was carried out for each parameter, using UB as the outcome, and the parameter and M-number as the predictor variables. *Figure 3.9* shows the predicted outcomes versus the specification values. The roundness and length dif graphs show higher degrees of scatter than the other two. The best results were achieved with axis ratio and the following regression equation:

$$UB = 100(3.9549 * axisratio - 0.0524 * M - 2.2786) \dots\dots (13)$$

This gave a correlation coefficient of 0.94 and a standard error in outcome estimation of 2.7%, the range of UB values being 40% to 85%.

The conclusion of the exercise is that when the M-fraction is known, axis ratio has a strong relationship with strength of synthetic diamond material and can be considered to be the most suitable choice of shape factor at this stage.

¹ Ideally a strength test would have been carried out on each of the samples. Valid strength results can only be ensured if the test is carried out by a trained operator. Resources for 33 tests were not available at the time of this experiment. Since the objective was merely to identify possible relationships it was felt that estimates of strength would be adequate.

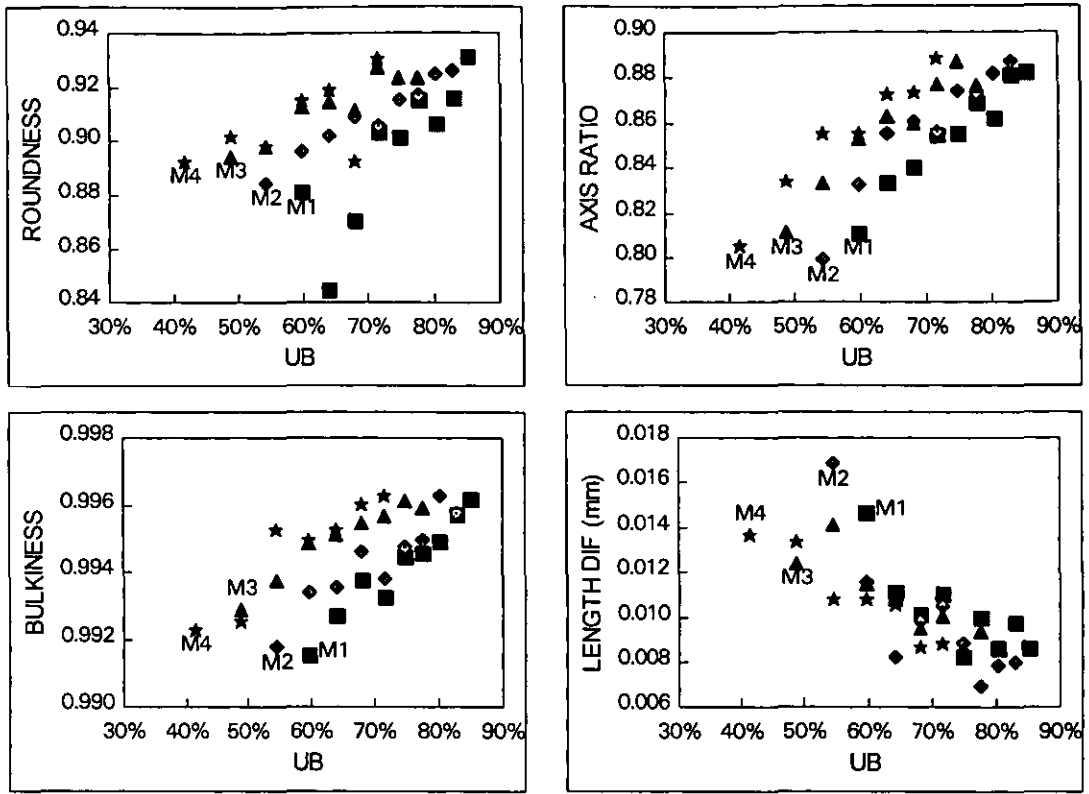


Figure 3.8 : Shape parameters related to strength parameter

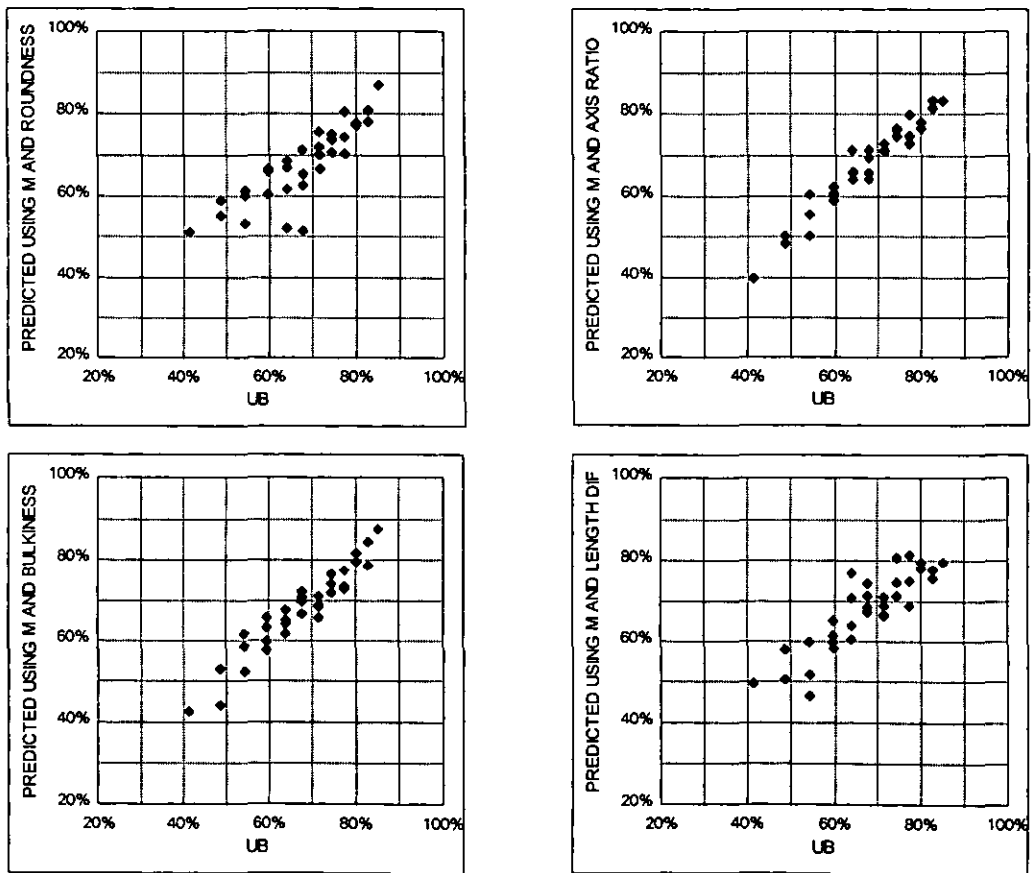


Figure 3.9 : UB predicted from shape parameters

3.3 FOURIER ANALYSIS

The use of a Fourier series to describe shape was introduced in Section 2.3.2. This type of shape analysis was popular among researchers in the late '70's and early '80's but never managed to find a real industrial use. Because it could not deal with re-entrant angles it was deemed to be suitable only for subtle differences between smooth, rounded particles. Computers and imaging systems at that time would have been slow and cumbersome to use and the handling of large amounts of data was very time-consuming. Paradoxically, as the task of data manipulation became easier, a new problem was introduced. More data could be generated more quickly, but to make any sense or practical use of it, ways of reducing it back to single parameters had to be found. In real applications it was usually easier to work with simple shape factors from the beginning. The connection between Fourier coefficients and shape could be seen, and shape parameters were defined, but the complexity of the method, and the large amount of data generated, made it impractical.

Despite the advances in computing power this is still the case today but it was felt that the Fourier analysis method was worth an investigation, partly because it forms a large part of the history of shape analysis and therefore should be included in any shape study, and partly because of the suitability of the diamond shape for this type of analysis. There are no re-entrant angles on the diamond particles in this study and the shapes are quite smooth and rounded.

3.3.1 Theory

The outline of a particle can be considered to be a periodic function, $R(\theta)$, with a period of 2π , and can be expanded as an infinite trigonometric series in the form

$$R(\theta) = A_0 + \sum_{n=1}^{\infty} (a_n \cos n\theta + b_n \sin n\theta) \quad \dots\dots\dots (14)$$

or
$$R(\theta) = A_0 + \sum_{n=1}^{\infty} A_n \cos(n\theta - \alpha_n) \quad \dots\dots\dots (15)$$

where
$$A_n = \sqrt{a_n^2 + b_n^2}, \quad \alpha_n = \tan^{-1}\left(\frac{b_n}{a_n}\right) \quad \dots\dots\dots (16)$$

The coefficients A_0 , a_n and b_n can be found when there is some knowledge of $R(\theta)$. A_0 is found by integrating both sides of the equation between 0 and 2π and rearranging to give

$$A_0 = \frac{1}{2\pi} \int_0^{2\pi} R(\theta) d\theta \dots\dots\dots (17)$$

To find a_n both sides of the equation are multiplied by $\cos(m\theta)$ and integrated between 0 and 2π . Similarly for b_n both sides are multiplied by $\sin(m\theta)$ and integrated. Using the orthogonality relations

$$\int_0^{2\pi} \sin m\theta \cos n\theta d\theta = 0 \dots\dots\dots (18)$$

$$\int_0^{2\pi} \sin m\theta \sin n\theta d\theta = \begin{matrix} 0, & m \neq n \\ \pi, & m = n \neq 0 \end{matrix} \dots\dots\dots (19)$$

$$\int_0^{2\pi} \cos m\theta \sin n\theta d\theta = \begin{matrix} 0, & m \neq n \\ \pi, & m = n \end{matrix} \dots\dots\dots (20)$$

this gives, for all n ,

$$a_n = \frac{1}{\pi} \int_0^{2\pi} R(\theta) \cos n\theta d\theta \dots\dots\dots (21)$$

$$b_n = \frac{1}{\pi} \int_0^{2\pi} R(\theta) \sin n\theta d\theta \dots\dots\dots (22)$$

3.3.2 Determining The Fourier Coefficients

The display was thresholded to give the particle pixels a value of 0 (black) and the background pixels a value of 255 (white). The scripting facility in the image analysis software was then used to set up a routine to scan a chosen single particle with its surrounding area and write the grey values of each pixel to a file. A QuickBASIC program was written to extract the co-ordinates of the edge pixels from these grey-level files. The program begins by identifying particle pixels (as opposed to background pixels) and finding the centroid. Having located an edge pixel, an edge-finding algorithm searches eight neighbouring pixels to find the next edge pixel and continues around the particle counting the number of edge pixels as e . For the purposes of the search, an edge pixel is defined as a black pixel with at least one white

pixel among its four off-diagonal neighbours. The Cartesian co-ordinates of the edge pixels are written to a file.

The program for calculating the Fourier coefficients begins by reading the edge co-ordinates from the edge file and converting them to polar co-ordinates with the centroid as origin. To remove size effects the radii are normalised by the average radius. The first N coefficients of the series must then be found. Since the angles are not evenly spaced numerical methods of integration like Simpson's rule cannot be used. If the number of coefficients required is less than half the number of edge points then the coefficients can be found by solving a set of simultaneous equations using a technique such as Gaussian elimination. Another option is to fit parabolas to each set of three successive points and numerically integrate them. An easier alternative is to connect the points with straight lines, as was done by Ehrlich and Weinberg, [33] so that at the i th edge point

$$R_i(\theta) = \frac{(R_{i+1} - R_i)\theta + R_i\theta_{i+1} - R_{i+1}\theta_i}{\theta_{i+1} - \theta_i} \dots\dots\dots (23)$$

and $\sum_{i=1}^e \int_{\theta_i}^{\theta_{i+1}} R_i(\theta) d\theta$ is used to estimate $\int_0^{2\pi} R(\theta) d\theta$ in the calculation of the coefficients. The latter option is used here. A selection of the Luerkens/Beddow/Vetter descriptors [38] is also calculated and reported along with the coefficients. As a check on the results, the program regenerates the radii from the angles and coefficients, and compares the regenerated profile with the original. The error in regeneration is

calculated as the root mean squared difference in radii. Full program listings of the edge-finding program and the Fourier program are given in *Appendices 1 and 2*.

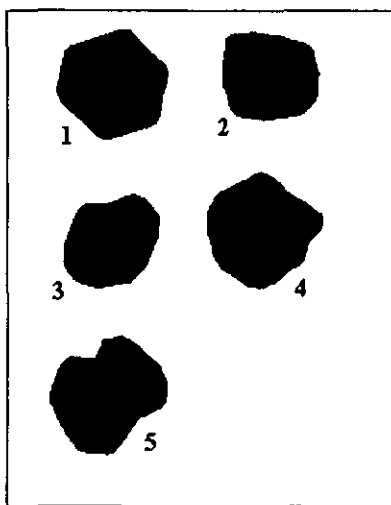


Figure 3.10 : Five diamond profiles

A selection of five particles is shown in *Figure 3.10* and the errors for regeneration with 20, 50, 100, 200, and 500 coefficients are plotted in *Figure 3.11*. The errors decrease as more coefficients are used, and with 500 coefficients the error is 0.2% or less for each of the particles. *Figures 3.12 and 3.13*

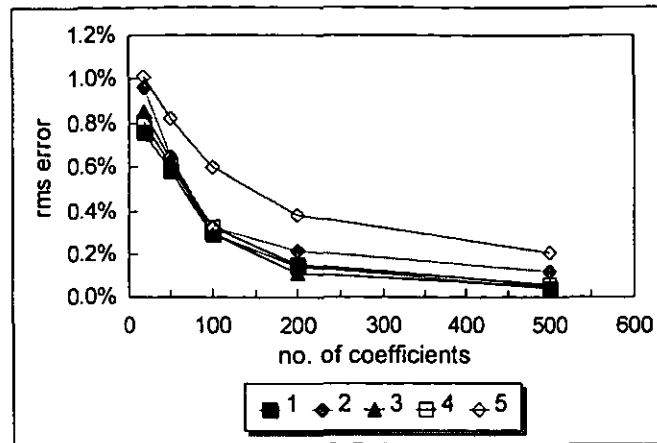


Figure 3.11 : Regeneration errors for particles 1-5

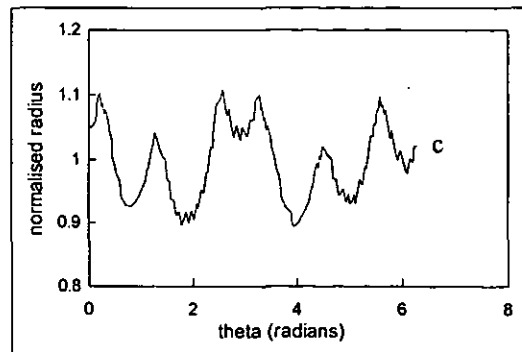
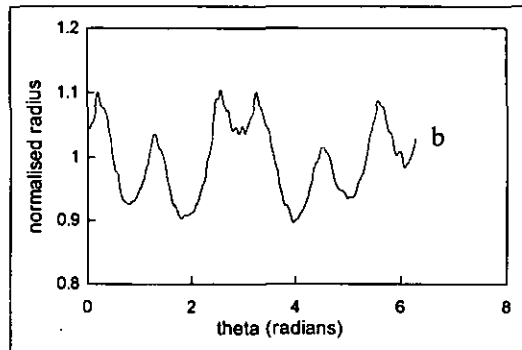
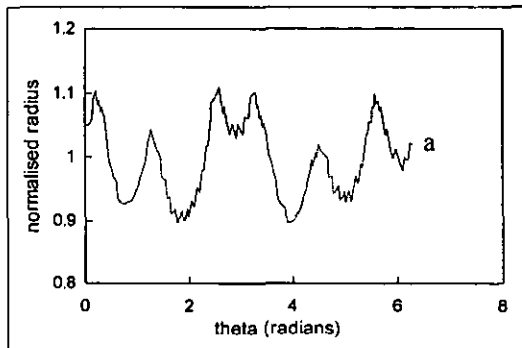


Figure 3.12 : Particle 1, (a) original, (b) regenerated using 50 coefficients, (c) regenerated using 500 coefficients

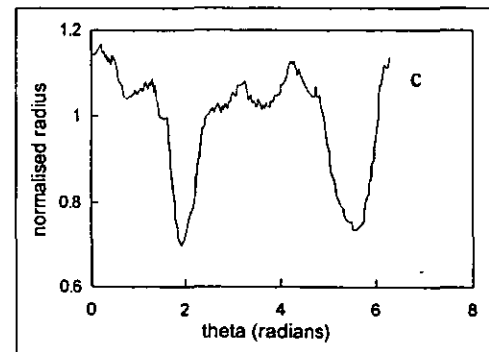
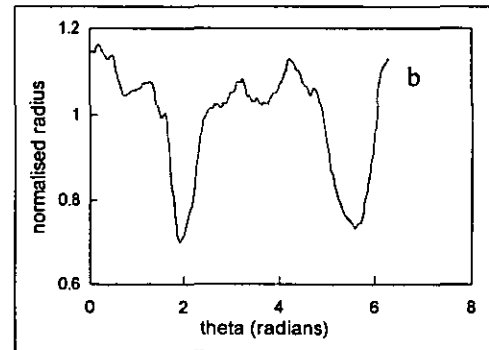
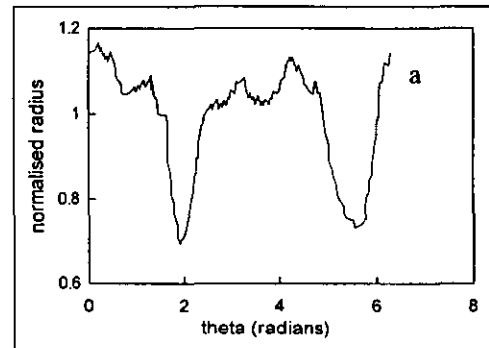


Figure 3.13 : Particle 5, (a) original, (b) regenerated using 50 coefficients, (c) regenerated using 500 coefficients

show original and regenerated profiles for particles 1 and 5, representing the best and worst fits respectively. When 50 coefficients are used the parts of the profile with small oscillations are smoothed in regeneration but the macro shape is a very good representation of the original. These small oscillations are characteristic of digitisation on a square grid, rather than a feature of the diamond particles. The conclusion is that 50 coefficients are more than enough to describe the macro shape, while 500 coefficients will accurately reproduce every undulation in the profile.

The morphological Fourier descriptors proposed by Luerkens, Beddow and Vetter take all of the calculated coefficients into account (N appears in the equation for R_0). The cited advantage of these descriptors is that they are rotationally invariant. However, the coefficient A_n is not dependent on particle orientation. If it is not necessary to reproduce the profile then only the first few coefficients need to be calculated and they can be used as shape descriptors in their own right, eliminating the problem of deciding on a suitable value for N .

3.3.3 Fourier Analysis Results

24 particles from bin 2 and 24 particles from bin 9 are shown in binary form in *Figures 3.14* and *3.15*. These are fields of view chosen at random from two slides from a tabling of bulk 40/45 SDA material. The images were stored with the contrast set to maximum to give black particles on a white background. The script routine was used to produce a grey-level file for each particle and then the edgfinder program extracted the co-ordinates of the edge pixels. Finally the Fourier program calculated and reported the coefficients A_0 , $a_1b_1...a_{10}b_{10}$, and the Luerkens, Beddow and Vetter (LBV) shape terms R_0 , L_0 , and $L_2(1)...L_2(5)$ (equations 5, 6, 7 from chapter 2).

The method was validated by rotating the bin 9 binary image by 90° and repeating the analysis for five of the particles in the rotated image. Some of the results are compared with those of the original in *Table 3.1*. The coefficients a_n and b_n vary with rotation, as expected, while A_n and the LBV shape factors do not. Any discrepancies can be attributed to slight alteration of the particle outline by the software during rotation. The A_n terms proved to be more consistent with rotation than the LBV shape factors in this exercise.

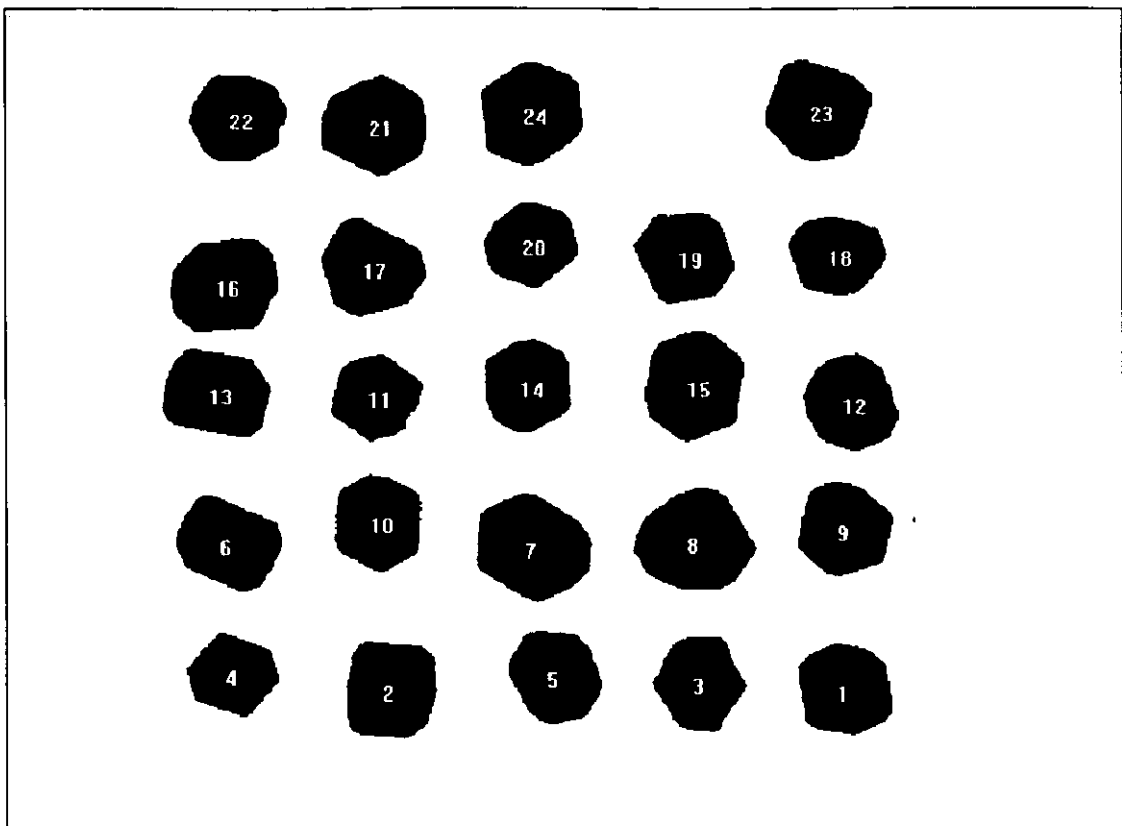


Figure 3.14 : Profiles of 24 particles from bin 2

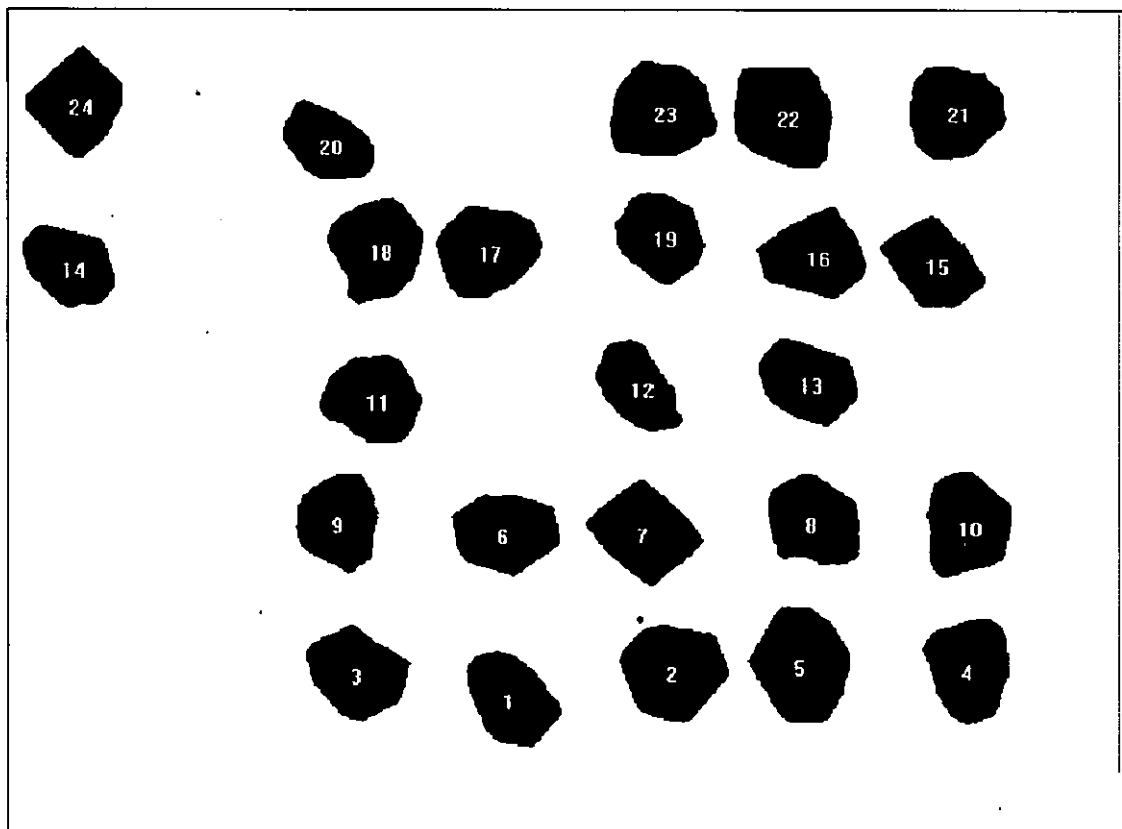


Figure 3.15 : Profiles of 24 particles from bin 9

Table 3.1 : Fourier coefficients for rotated particles

	3	3	9	9	11	11	18	18	20	20
points	178	178	176	176	181	181	188	188	159	159
A0	0.9861	0.9861	0.9928	0.9928	0.9947	0.9946	0.9924	0.9924	0.9681	0.9681
a1	-0.0018	0.0069	-0.0078	-0.0025	0.0059	-0.0050	0.0052	-0.0065	-0.0073	0.0086
a2	0.0669	-0.0669	-0.0808	0.0808	0.0670	-0.0670	-0.0574	0.0574	0.0910	-0.0910
a3	0.0425	0.0303	-0.0730	0.0038	-0.0638	-0.0094	-0.0034	0.0601	0.0520	-0.0074
a4	0.0455	0.0455	-0.0152	-0.0152	0.0201	0.0200	0.0131	0.0131	-0.0145	-0.0145
a5	-0.0021	-0.0244	0.0355	-0.0032	-0.0056	0.0218	-0.0157	-0.0272	-0.0198	0.0132
b1	-0.0069	-0.0018	0.0025	-0.0078	0.0049	0.0060	0.0065	0.0052	-0.0086	-0.0073
b2	-0.1010	0.1010	-0.0002	0.0002	-0.0442	0.0441	0.0031	-0.0031	-0.1863	0.1863
b3	0.0303	-0.0425	0.0038	0.0730	-0.0095	0.0640	0.0601	0.0034	-0.0074	-0.0520
b4	-0.0095	-0.0095	0.0177	0.0177	0.0058	0.0057	-0.0506	-0.0506	-0.0312	-0.0312
b5	0.0244	-0.0021	0.0032	0.0355	-0.0216	-0.0055	0.0272	-0.0157	-0.0132	-0.0198
A1	0.0071	0.0071	0.0082	0.0082	0.0076	0.0078	0.0083	0.0083	0.0113	0.0113
A2	0.1211	0.1211	0.0808	0.0808	0.0803	0.0802	0.0575	0.0575	0.2074	0.2074
A3	0.0522	0.0522	0.0731	0.0731	0.0645	0.0647	0.0602	0.0602	0.0525	0.0525
A4	0.0465	0.0465	0.0233	0.0233	0.0209	0.0208	0.0523	0.0523	0.0344	0.0344
A5	0.0245	0.0245	0.0357	0.0357	0.0223	0.0225	0.0314	0.0314	0.0238	0.0238
R0	0.9916	0.9916	0.9964	0.9964	0.9980	0.9979	0.9955	0.9955	0.9806	0.9806
L0	0.9945	0.9945	0.9964	0.9964	0.9967	0.9967	0.9969	0.9969	0.9873	0.9873
L2(1)	0.0000	0.0000	0.0000	0.0000	0.0000	0.0000	0.0000	0.0000	0.0001	0.0001
L2(2)	0.0072	0.0075	0.0032	0.0033	0.0032	0.0032	0.0016	0.0017	0.0207	0.0224
L2(3)	0.0013	0.0014	0.0027	0.0027	0.0021	0.0021	0.0018	0.0018	0.0013	0.0014
L2(4)	0.0011	0.0011	0.0003	0.0003	0.0002	0.0002	0.0014	0.0014	0.0006	0.0006
L2(5)	0.0003	0.0003	0.0006	0.0006	0.0002	0.0003	0.0005	0.0005	0.0003	0.0003

Studying the sets of coefficients for the 48 particles it was noted that, in general, A_2 was the dominant coefficient and that the magnitude of the coefficients dropped after A_6 . Many of the papers on this subject point out that A_2 represents elongation, A_3 represents triangularity and A_4 represents blockiness, but none have illustrated the fact. *Figure 3.16* shows the relative proportions of the coefficients A_1 to A_6 for the two sets of particles from *Figures 3.14* and *3.15*. After studying these graphs in conjunction with the particle images there can be no doubt about the fact that the Fourier coefficients contain shape information. This will be demonstrated in the following discussion.

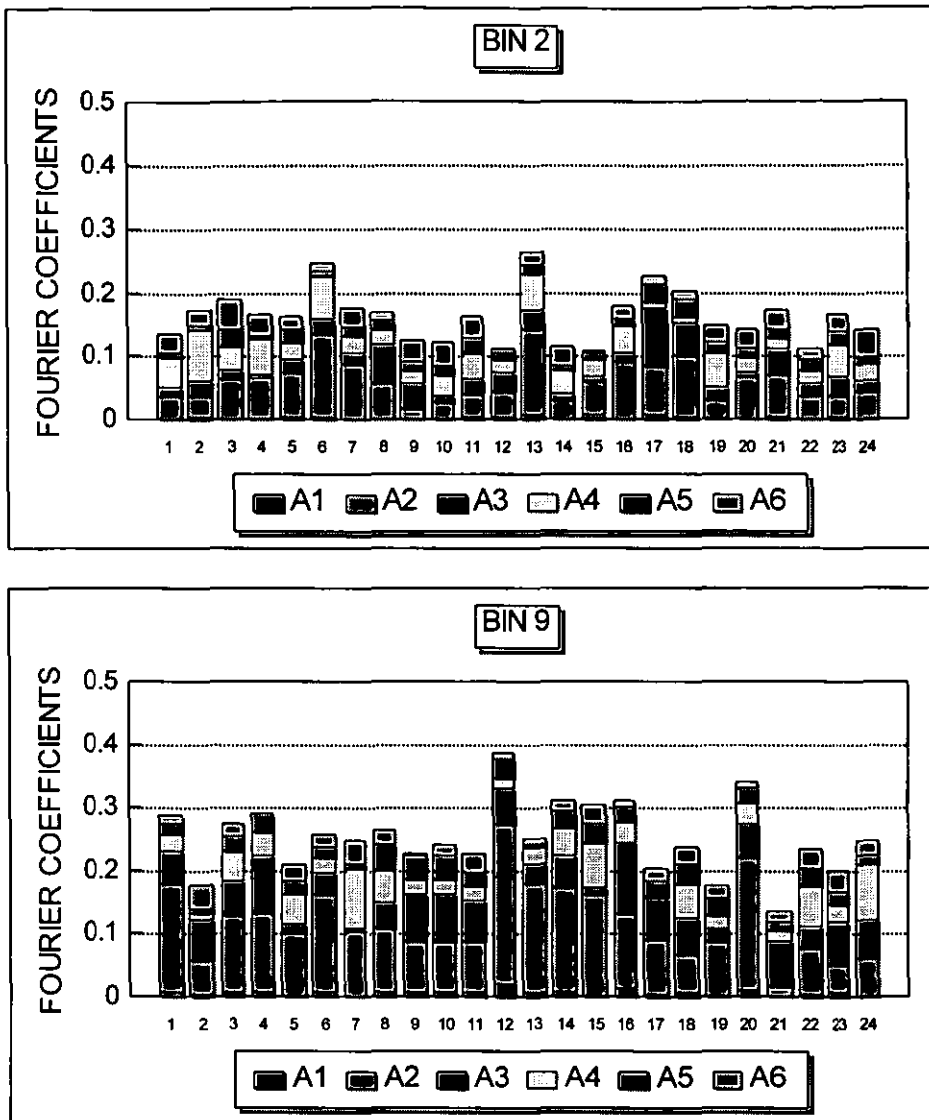


Figure 3.16 : Magnitudes of Fourier coefficients

Considering only the graphs and concentrating on A_2 , A_3 , and A_4 to start with, the following suggestions can be made.

For bin 9:

- ♦ the most triangular particle is no.16 (highest A_3),
- ♦ the blockiest is no.7 (highest A_4 , low A_3), next is no.15
(no.24 is also blocky but has a larger triangular component than nos.7 and 15),
- ♦ the most elongated are nos.12 and 20 (high, dominant A_2),
- ♦ no.6 is also elongated (dominant A_2),
- ♦ particles 9 and 10 have identical shape.

For bin 2:

- ♦ the most triangular particle is no.17 (high A_3),
- ♦ the blockiest is no.2 (high, dominant A_4),
- ♦ nos.6 and 13 are blocky but also elongated (high A_2 and A_4),
- ♦ particles 10 and 14 are similar in shape.

These suggestions are all confirmed by looking at the particle images and using the human ability to assimilate shape.

The other coefficients are not as easily related to the perception of the different shapes. It would be expected that the particles with hexagonal outlines would have a higher A_6 than other particles. Looking at the bin 2 particles it can be seen that this is the case for particle 3. However, particle 24 also has a high A_6 but is not an obvious hexagon, while particle 15 looks reasonably hexagonal but has a very small A_6 . It quickly becomes clear that a single coefficient can provide the correct sense of the macro shape for some particles, but will not be relevant on its own for others. For example, if the particles to be studied were triangular in nature, then the magnitude of A_3 might be useful as a shape descriptor. Particles deviating greatly from a triangle would be described only as "poor triangles" and there would be no clue to the actual shape, unless other coefficients were also considered.

It can be seen in *Figure 3.14* that particle 4 is a hexagon. It has strong even coefficients and its odd coefficients are very small. Particles 16, 14 and 10 from the same bin show a similar dominance of the even coefficients. This represents a regularity or symmetry in the particle outline. Note that the pattern of coefficients for particle 7 of bin 9 is almost identical to that of particle 4 from bin 2, even though the former is a rectangle and the latter a hexagon.

The more circular particles, for example particles 12, 5 and 22 in bin 2, tend to have A_2 as the dominant coefficient, with subsequent coefficients either decreasing steadily or having equal magnitude. Meloy plotted A_n versus n on a log-log graph [34] and proposed a law of morphological coefficients, with slope, intercept and scatter about the fitted line as three shape parameters. He stated the law as follows:

$$A_n = A_1 \left(\frac{1}{n}\right)^s \dots\dots\dots (24)$$

or $\ln A_n = \ln A_1 - s \ln n \dots\dots\dots (25)$

where A_1 is the intercept and $-s$ is the slope.

To see if diamond particles follow this law the first 100 coefficients were calculated for three particles of different appearance - Particle 12 from bin 2 (circular), particle 4 from bin 2 (hexagonal), and particle 7 from bin 9 (rectangular). The log-log plots are shown in *Figure 3.17*. *Table 3.2* gives the values of slope, intercept and scatter.

Table 3.2 : Slope, intercept and scatter for A_n v's n

<i>particle</i>	<i>shape</i>	<i>s (slope)</i>	<i>A₁ (intercept)</i>	<i>σ_m (scatter)</i>
12, bin 2	circular	0.96	0.0355	0.43
4, bin 2	hexagonal	1.07	0.0461	0.51
7, bin 9	rectangular	1.12	0.0822	0.25

Meloy pointed out that particles with high aspect ratios have higher slopes than rounder particles. This is indeed the case. The increasing values of A_1 also represent increasing deviation from a circle. The scatter parameter is the unbiased estimate of variance. Following Meloy's example the first eight coefficients were omitted in its calculation.

$$\sigma_m = \frac{1}{91} \sum_{n=9}^{100} (\ln \bar{A}_n - \ln A_n) \dots\dots\dots (26)$$

It is difficult to see the use of the scatter parameter, except to say that the scatter should always be low if the law of morphological coefficients is true! In fact, the macro shape is defined by the lower order coefficients and these do not fit the relationship very well. The higher order coefficients are related to the roughness or fine detail of the profile. If the first eight coefficients are omitted from the calculation of scatter then it has very little to do with macro shape. The rectangular particle has the lowest scatter and is therefore smoother than the others.

From this brief analysis it seems that there is some value in the slope and intercept in quantifying a degree of circularity, but the law of morphological coefficients is

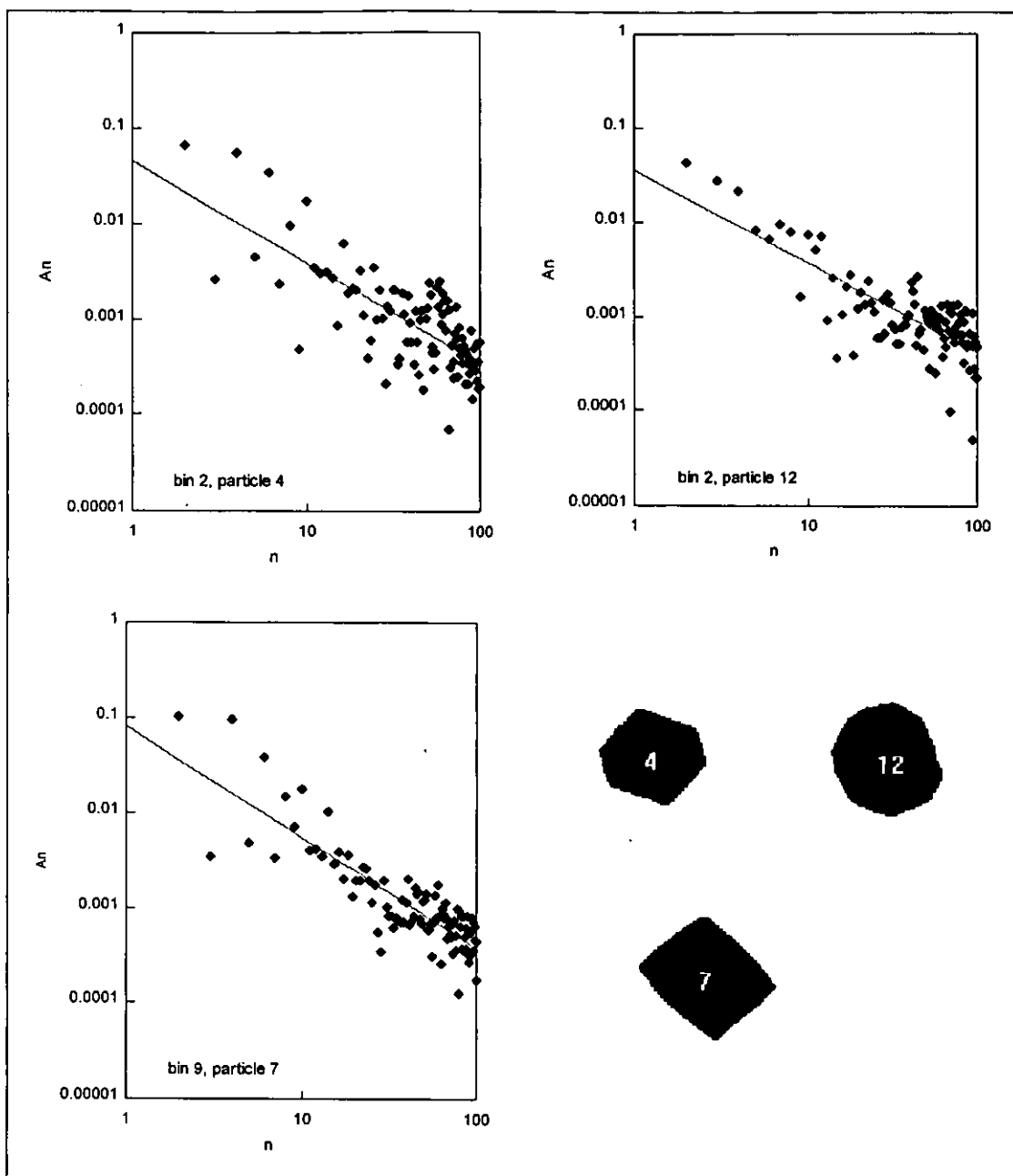


Figure 3.17 : $\ln(A_n)$ v's $\ln(n)$ for the three particles shown. Lines were fitted by least squares method.

artificial. It relies too much on the fact that the higher order coefficients are always smaller than the lower order coefficients and ignores the fact that the more important lower coefficients are off the fitted line. (When A_2 to A_8 are included the scatter increases to 0.47, 0.69 and 0.38 respectively. A more universally recognised measure of the scatter is the correlation coefficient, R^2 , which is 0.61, 0.57 and 0.74 respectively. These are all regarded as poor fits.)

3.3.4 Comparison Of Bin 2 With Bin 9 Using Fourier Coefficients

So far the particles have been examined individually and it has been demonstrated that the lower order coefficients are related to macro shape. Also of interest is the question of discrimination. Can the coefficients be used to distinguish bin 2 particles from bin 9 particles?

The relative magnitudes of the coefficients should say something about the shape, so A_2 , A_3 and A_4 were plotted on a triangular graph (Figure 3.18). It was hoped that two obvious clusters would be seen but this was not the case. It would be very difficult to identify the origin of a particle from its place in this graph. $L_2(2)$, $L_2(3)$ and $L_2(4)$ were plotted in a similar way but gave little improvement (Figure 3.19). This simply shows that the particles all belong to the same family, or that they are a small subset of the set of all possible shapes. It is likely that this type of graph would distinguish between diamond and another abrasive, silicon carbide for example, but it is not suitable for discrimination within one family.

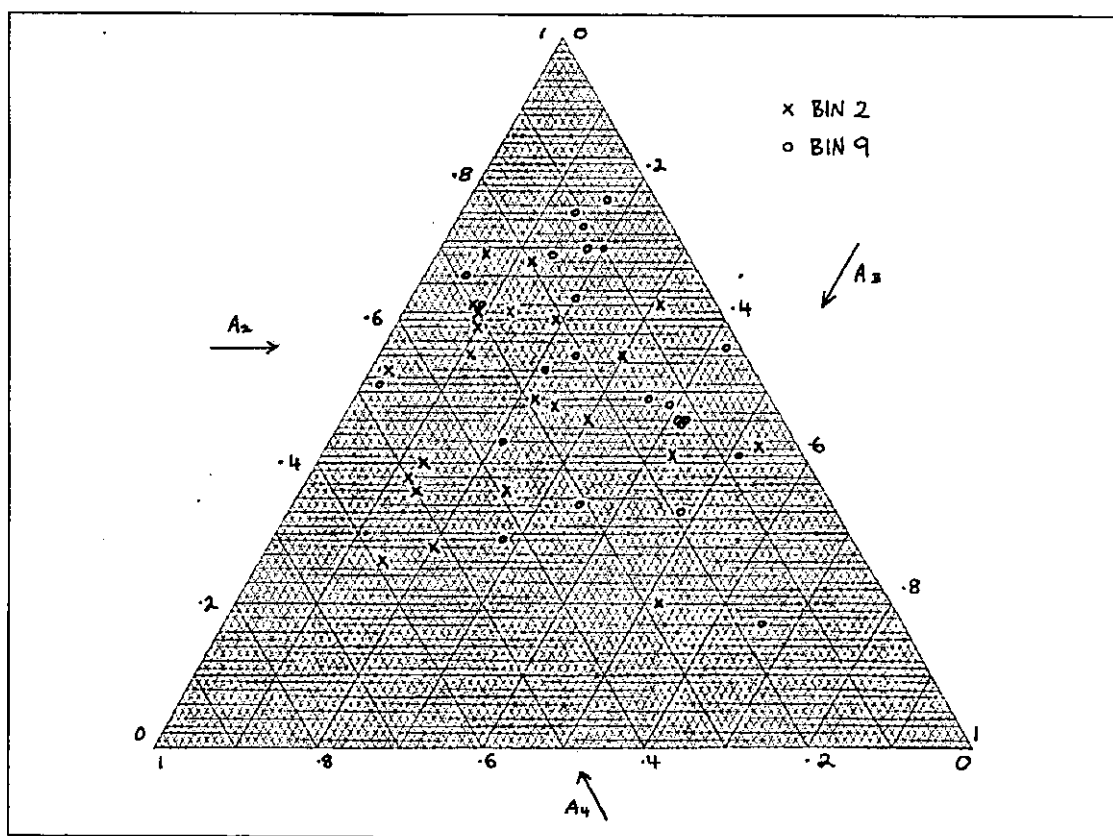


Figure 3.18 : Triangular graph of Fourier coefficients A_2 , A_3 , A_4

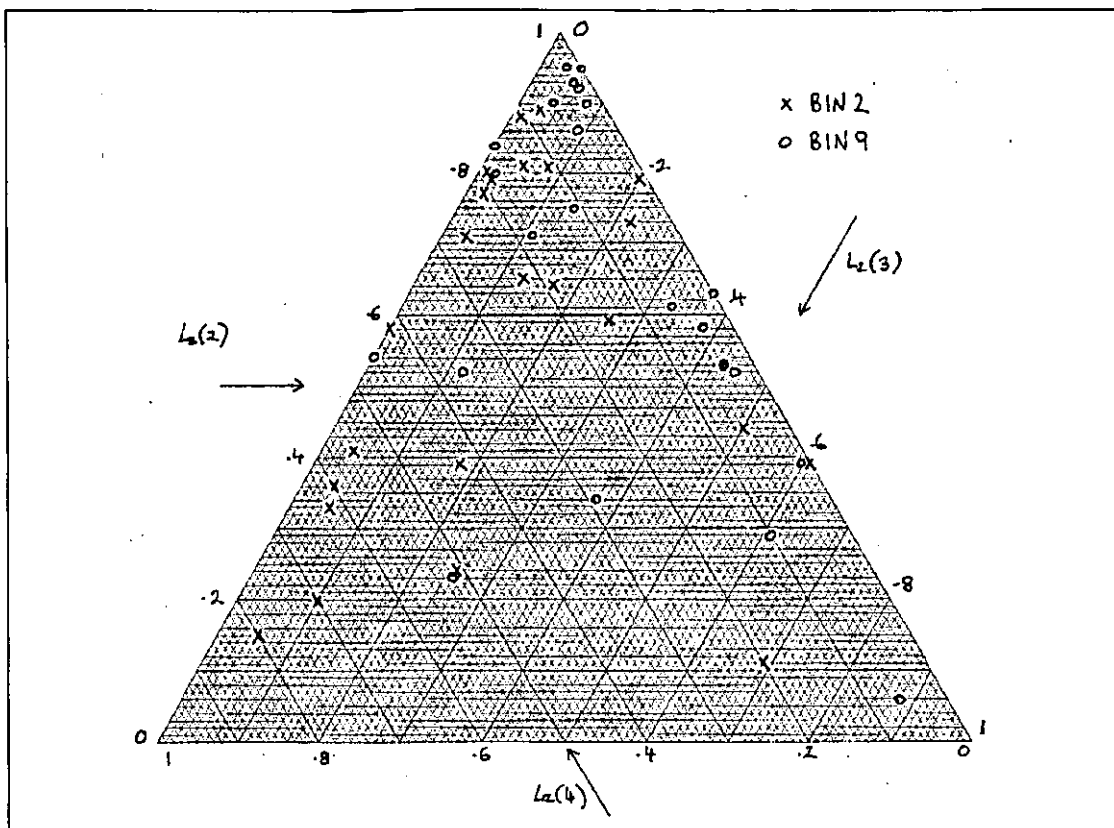


Figure 3.19 : Triangular graph of $L_2(2)$, $L_2(3)$, $L_2(4)$

Looking back at *Figure 3.16* (page 56) it is obvious that there is a difference in absolute magnitude of the lower order coefficients. In general, the sum of the first six coefficients is higher for bin 9 particles than for bin 2 particles. This sum is plotted for the two groups of particles in *Figure 3.20*. There is a large degree of overlap between the two populations, which makes classification of individual particles impossible. However, a t-test on the means of the two populations shows that they are significantly different with more than 99% confidence. This means it would be possible to distinguish between a group of particles from bin 2 and a group of particles from bin 9, using the mean sum of the first six coefficients.

Since A_2 is the dominant coefficient in most of the particles this was tested in the same way and once more the two populations (*Figure 3.21*) were found to differ with more than 99% confidence.

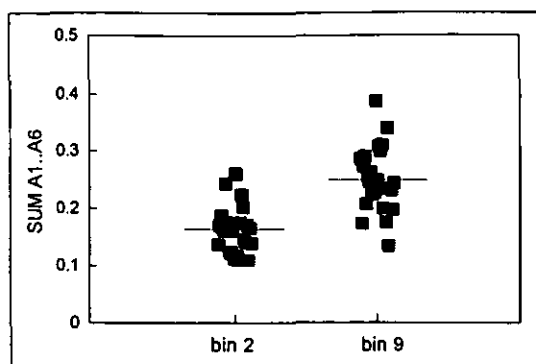


Figure 3.20 : Sums of first 6 coefficients

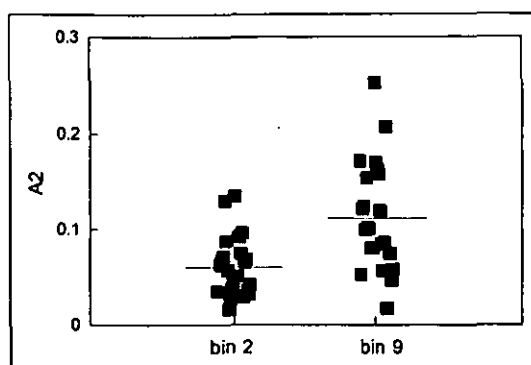


Figure 3.21 : Second coefficient

3.3.5 Discussion Of Fourier Analysis Results

The work on Fourier analysis shows that the shape is fully described by the A_n coefficients. All the information is there, although extraction of the parts that are most relevant, and development of a simple shape descriptor are difficult tasks. Some applications from the literature were tried on diamond particles, which have profiles ideally suited to this type of analysis. No advantage could be seen in using the LBV shape factors over the A_n coefficients, and Meloy's method of plotting A_n versus n on log scales did not appeal. In the end the simple approach of comparing the means of the low order coefficients gave the most promise as a potential tool for classification.

A classification of individual particles would be much preferred and the Fourier analysis has not come any closer to that target than the direct measurement of shape factors by the image analysis software. The average A_2 value of a group of particles may point to the bin of origin, but so does the average axis ratio. Axis ratio is much easier to measure with the current resources. Which is better? It turns out that they correlate very well, giving a straight line when plotted against each other (*Figure 3.22*).

This is an encouraging discovery. It proves that an aspect-ratio-type shape factor is an appropriate choice. It also proves the integrity of Fourier analysis, while supporting the earlier selection of axis ratio as a relevant parameter.

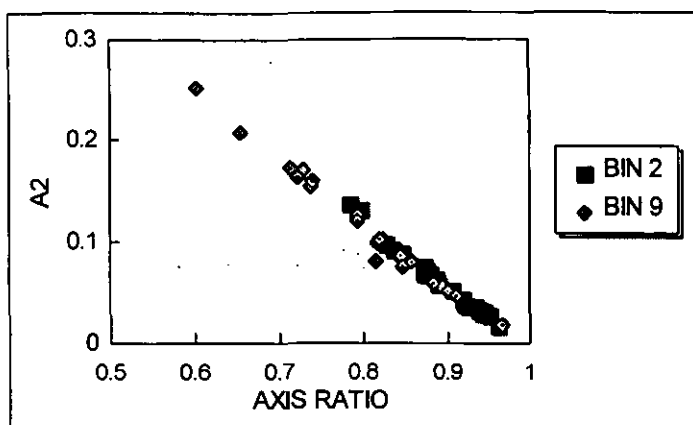


Figure 3.22

Second Fourier coefficient plotted against axis ratio for particles from bin 2 and bin 9

3.4 FRACTALS AND POLYGONAL HARMONICS

Fractal analysis was developed by Kaye and others for the description of rugged boundaries, such as fumed particles or flocculates. Diamond particles have mostly smooth, sharp edges so fractal analysis is not really appropriate, but it was included in this study as a step to polygonal harmonics.

3.4.1 Boundary Fractal Analysis

The draw facility in the software was used to create an image of the boundary of a square and a hexagon, for use as diamond-like reference shapes. A representation of a Koch triadic island was scanned in from [51] as a fractal reference shape (see *Figure 3.23* overleaf). This has an infinite perimeter and a fractal dimension of 1.2618. Following Flook's description [59], these three shapes were dilated successively twenty times by a cross-shaped dilation element three pixels wide. This meant that the width of the boundary was one pixel initially, and increased by two pixels with each dilation. The software reported the pixel area each time, and then the length, $L(w)$, of the perimeter could be estimated by dividing the area by the width, w , of the boundary. $L(w)$ and w were normalised by the maximum Feret diameter, and plotted on a Richardson plot (*Figure 3.23*).

There are no obvious linear portions in the data for the square and the hexagon. This is not surprising because these are not rugged shapes, and do not have the characteristic of self-similarity. Neither are the curves flat, because there is overlap of

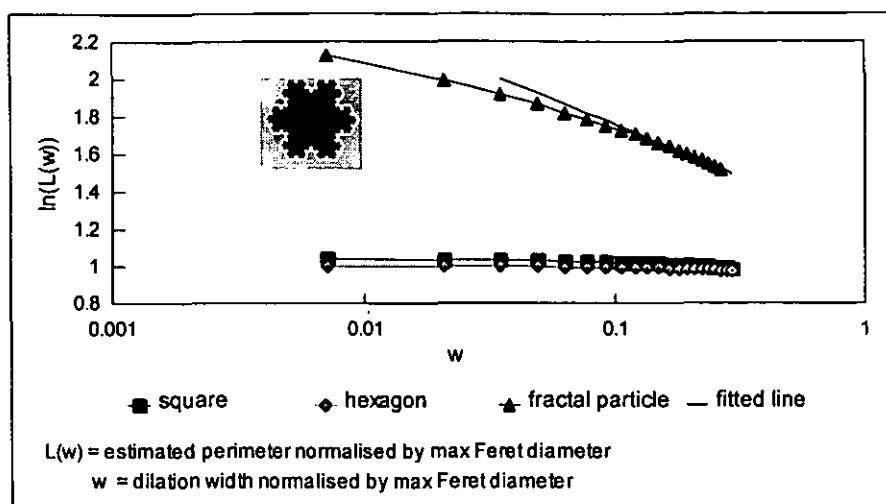


Figure 3.23 : Richardson plot of computer drawn shapes

the extra pixels when the corners are dilated. A similar effect would be seen in stepping around the boundary, where bigger steps cut across the corners. A square has sharper corners than a hexagon so its curve drops more steeply. The fractal particle gives a linear plot after eight dilations. Fitting a straight line to these points gave a slope of -0.2610 , and hence a fractal dimension of 1.2610 . The small difference between this and the published value of 1.2618 can be attributed to the fact that the analysis was carried out on a scanned image of a Koch triadic island, rather than a mathematically generated one. It is close enough to show that the technique can be applied using the available equipment.

The five particles depicted in *Figure 3.10* (page 51) were then analysed in the same manner. The binary images were dilated once and then XORed² with the corresponding undilated images to give white outlines of the particles on a black background. These outlines were dilated twenty times, and the area of the boundary was reported each time. The perimeters were estimated as before and then normalised by the major axis. The Richardson plot is shown in *Figure 3.24*. Straight lines were fitted to any linear portions that could be found, and the resulting fractal dimensions are presented in *Table 3.3*.

² In a digitised image with discrete pixels the boundary must have a minimum width of one pixel. A decision must be made to take as the boundary either the outermost pixels of the particle or the background pixels immediately surrounding the particle. The former is achieved by erosion and the latter by dilation. The logical XOR operator compares two images and sets to white all pixels which differ, leaving the rest black. In this case dilation was chosen because the area of the boundary is inclined to underestimate the perimeter.

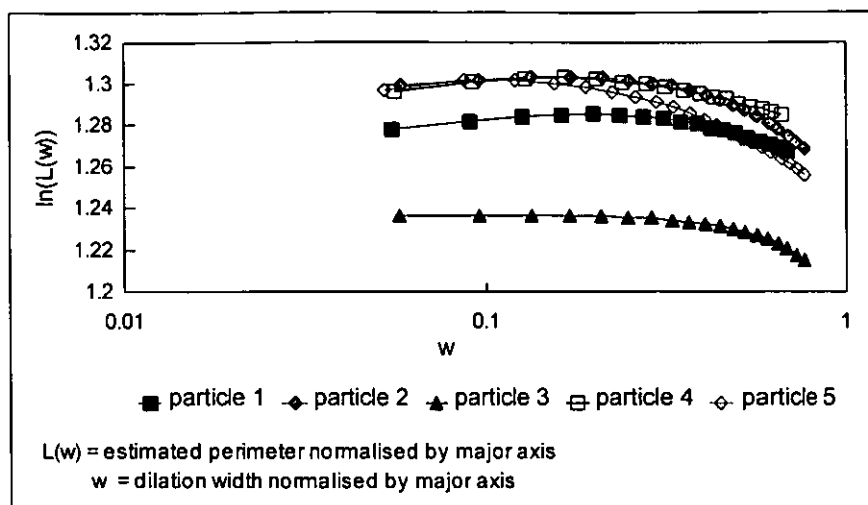


Figure 3.24 : Richardson plot for five particles

Table 3.3 : Fractal dimensions for five particles

Particle	Linear Portion 1	Linear Portion 2	Fractal Dimension 1	Fractal Dimension 2
1	none	-	-	-
2	w=19-25	-	1.03	-
3	w=9-15	w=15-23	1	1.01
4	w=17-25	w=27-35	1.01	1.02
5	w=9-15	w=19-27	1.01	1.03

The curves show a drop in perimeter length with increasing width of dilation, but are far from being "ideal" fractal curves. Some of them rise at the beginning, and most have more than one linear segment. The fractal values range from 1.00 to 1.03, so this proves that the particles are not rugged enough for this type of analysis.

3.4.2 Polygonal Harmonics

Regular diamond crystals have square or hexagonal profiles so a method involving polygons should be appropriate. The technique of polygonal harmonics was described in Chapter 2 (page 26). It borrows the idea of stepping around a boundary from fractal analysis but it describes macroshape rather than roughness. For a given step length an n th harmonic is said to exist if taking n steps around the boundary from a defined starting point produces a closed polygon. Harmonics can persist over a range

of step lengths and the persistence is defined as the ratio of the upper to the lower limits of the range. In a triangular particle the persistence of the third harmonic is high, while the persistence of the fourth harmonic is low.

A QuickBASIC program was written to step around the profiles of the bin 2 and bin 9 diamond particles from *Figures 3.14* and *3.15* (page 54). The program is listed in *Appendix 3*. It uses the same files of edge co-ordinates as the Fourier program.

A protocol is required for the choice of start point because this choice can affect the results. Reilly and Clark [67] found the longest diameter and chose the end with the lower y -co-ordinate as the start point. Young et al [69] averaged results from twenty different start points. Another option is to pick an arbitrary point from which to take the first step and continue stepping until locked into a repeating pattern of steps. Then the original start point can be discarded in favour of one of these points. This latter option was chosen here, with a first start point at angle 0° .

An exact method of stepping (rather than the popular but less accurate hybrid method) was chosen because the available computing power is more than adequate. Steps are taken in an anticlockwise direction, simply because the data points in the files of edge co-ordinates are stored in order of increasing angle. Closure of the polygon is assumed if a step ends at a point less than 0.01 pixels from an old point. If closure is not obtained after 100 steps the search is abandoned.

The initial aim was to measure persistences (ratio of the upper to the lower value of the range of step lengths where the harmonic exists [66]) but it was found that the relative importance of persistences is dependent on step length. For example, a harmonic that exists between step lengths of 40 and 50 has the same persistence (1.25) as a harmonic that exists for step lengths of 4 and 5 only. A second problem with persistence is the existence of other harmonics within the range of a harmonic. Maeder and Clark [70] overcame these problems by factoring out the impurities and placing more emphasis on the lower order harmonics. They defined harmonic endurance as the pure range normalised by the maximum diameter. However, this is

much the same as recording the number of occurrences of each harmonic and so offers little advantage over the standard approach of plotting a frequency histogram.

An example of the findings of the program is shown in *Table 3.4* below. The particle analysed is particle no. 8 from bin 2 (from *Figure 3.14* page 54). The first column gives the step size. The program begins with a step length of ten pixels and increases by one pixel until it can no longer land on the particle (that is, when the step size is longer than the maximum diameter). The second column is the number of steps taken before closure. This is also the number of sides of the polygon and the order of the harmonic. Where this is blank no harmonic was found after 100 steps. The third column shows the number of traverses of the particle outline before closure. If this is greater than one the harmonic is a complex harmonic.

Table 3.4 : Determining the polygonal harmonics for particle 8, bin 2

<i>step length</i>	<i>steps</i>	<i>traverses</i>	<i>step length</i>	<i>steps</i>	<i>traverses</i>	<i>step length</i>	<i>steps</i>	<i>traverses</i>
10	-	-	30	36	5	50	4	1
11	-	-	31	7	1	51	4	2
12	-	-	32	27	4	52	19	5
13	69	4	33	13	2	53	11	3
14	16	1	34	44	7	54	7	2
15	15	1	35	-	-	55	7	2
16	14	1	36	6	1	56	33	10
17	-	-	37	23	4	57	3	1
18	-	-	38	11	2	58	3	1
19	-	-	39	27	5	59	3	1
20	11	1	40	-	-	60	3	1
21	-	-	41	5	1	61	3	1
22	-	-	42	5	1	62	3	1
23	67	7	43	-	-	63	6	3
24	-	-	44	14	3	64	3	2
25	-	-	45	9	2	65	3	2
26	59	7	46	22	5	66	8	3
27	8	1	47	13	4	67	5	3
28	31	4	48	29	7	68	2	1
29	15	2	49	4	1	69	2	1

The third simple harmonic persists over a range of step lengths from 57 to 62 - a persistence of 1.088. The second, fourth and fifth harmonics each last for two step lengths but have different persistences (1.015, 1.020 and 1.024 respectively). Since these are the only occurrences of these harmonics there are no impurities to be filtered out. However, the endurance parameter will at least give the same result for the second, fourth and fifth harmonics, as does a frequency count. *Figure 3.25* shows the frequency histogram for this particle (simple harmonics only).

Rather than plotting individual histograms for the 48 particles from bins 2 and 9, stack bar charts were chosen to plot the relative frequencies of the second to sixth harmonics in *Figure 3.26*. In this format it is easy to compare the results with those from Fourier analysis given previously in *Figure 3.16* (page 56). Each frequency is expressed as a percentage of the total range of step lengths for the particle. For example, from *Table 3.4*, the third harmonic appears for 6 of the 60 step lengths, which is 10%.

Some similar observations can be made when looking at these plots as were made when studying the plots of Fourier coefficients. Particles 2, bin 2, and 7, bin 9 have the highest 4th harmonic contributions and are the most square in appearance. Particles 17, bin 2, and 16, bin 9 still come out as the most triangular. Particle 12 bin 9 is by far the most elongated of all the particles, and so on. There are also some differences though. Particle 21 was the only particle in the bin 9 set to have a very low A_2 but in the polygonal analysis particles 11, 16, 17 and 21 have low second harmonics. There is also a much stronger suggestion of triangularity for particle 17 by this method than there was by Fourier analysis.

Contrary to expectations, there are no obvious squares or hexagons but the general rules seem to hold. The rounder particles have fewer harmonics than those with corners - for example particles 8 and 12 compared with particles 3 and 4, all in bin 2.

To round off this section the second harmonic is plotted against axis ratio in *Figure 3.27*. The relationship is not as good as the one between axis ratio and the second Fourier coefficient.

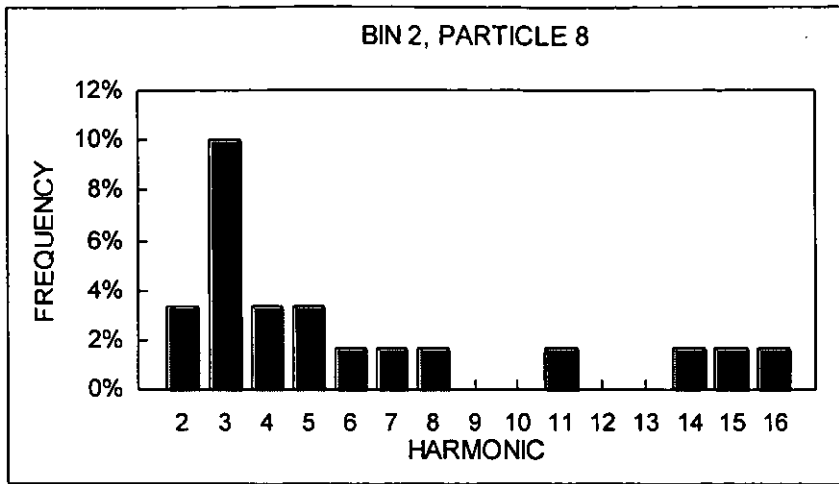


Figure 3.25 : Harmonic frequency histogram

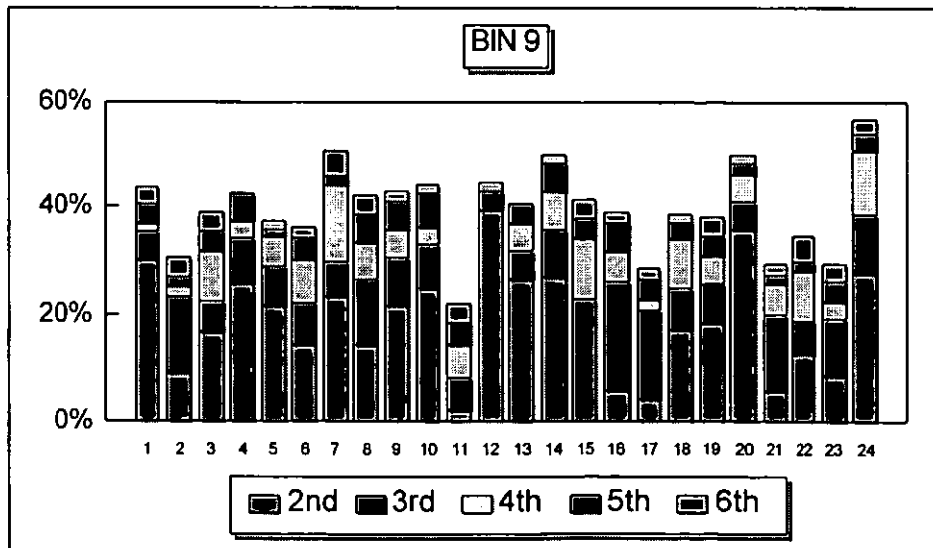
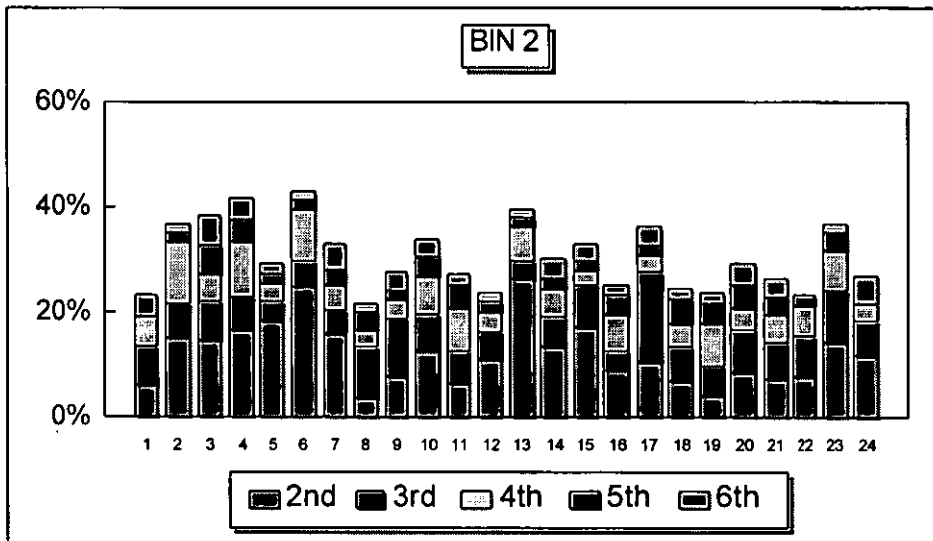


Figure 3.26 : Polygonal harmonic frequencies

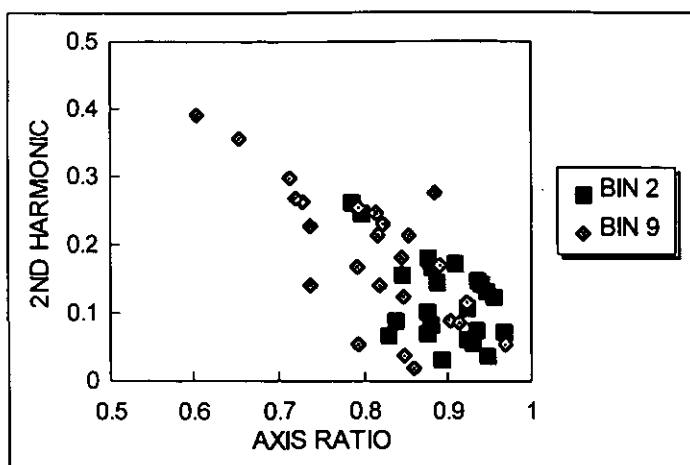


Figure 3.27

Second polygonal harmonic plotted against axis ratio for particles from bin 2 and bin 9

Finally, just out of curiosity, the stepping algorithm developed for polygonal harmonics was adapted so that the perimeter could be estimated for various step lengths, leading to calculation of the fractal dimension. The procedure was tried on the edge co-ordinates of some of the bin 2 and bin 9 particles. The largest value obtained was 1.0295. This was for particle 12, bin 9. To compare the dilation method with the stepping method the same particle was dilated as described previously and the boundary fractal dimension came out to be 1.0291; a surprisingly good correlation!

3.5 COUNTING CORNERS

An important property of abrasive particles in cutting tools is the number of exposed cutting edges. This property can possibly be quantified by counting the corners on a two-dimensional projection of a particle. Two corner identification methods have been reported in the literature. Both operate on lists of edge co-ordinates. They can be described briefly as follows:

Spanning Chord Method [74]

A step length, n , is chosen. The distance from each point, i , to the next n th point is calculated and plotted against i . Chords tend to shorten as they cross corners, producing dips in the graph.

Radius of Curvature Method [75]

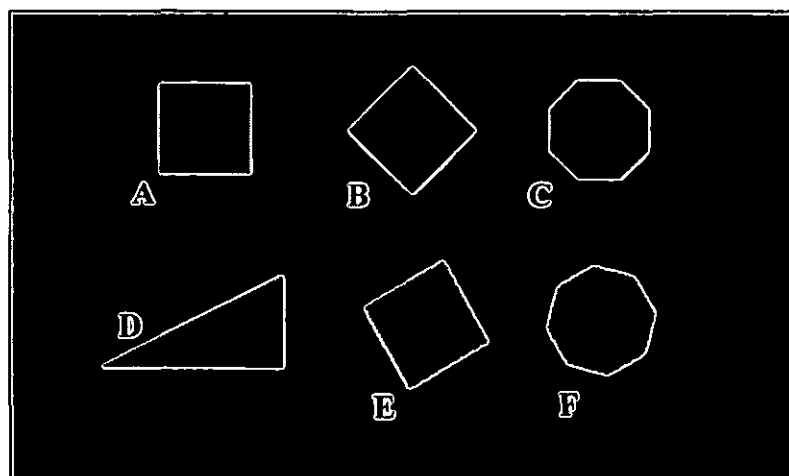
The equation of a circle is solved for radius, r_i , for each set of three points (x_{i-s}, y_{i-s}) , (x_i, y_i) , (x_{i+s}, y_{i+s}) and r_i is plotted against i . The resolution is governed by the spacing, s , between the points. Where the radius is infinity, or very large compared to any radius of the particle, a chosen maximum value is used. Corners have shorter radii and are represented by dips in the graph.

Before attempting to analyse real diamond particles, the methods were tested and compared using the shapes shown in *Figure 3.28*. These shapes were drawn in Microsoft Windows Paintbrush and are described as follows:

- A) a square 55x55 pixels,
- B) the square rotated by 45° giving edges of 40 diagonally connected pixels,
- C) an octagon with sides of 26 pixels or 18 diagonally connected pixels,
- D) a right angled triangle with short sides of a ratio of 2:1,
- E) the square rotated through 30°,
- F) the octagon rotated through 30°.

The square provides right angles and straight edges aligned with the digitisation grid. The square rotated by 45 degrees has straight edges at an angle of 45 degrees to the grid, providing lines of diagonally connected pixels. The octagon is a combination of the two and introduces 135 degree angles. The triangle has angles less than 90 degrees and an edge with a less straightforward arrangement of pixels. Rotating the

Figure 3.28 : Test shapes generated by computer



square and octagon by 30 degrees gives lines that do not easily fit into the digitisation grid, having both side and corner connected pixels within each straight section, and losing definition at the corners. The sizes were chosen to give roughly the same area as the real particles (approximately 3000 pixels per particle).

3.5.1 The Spanning Chord Method

A right angle gives a good illustration of the principle of the spanning chord method (Figure 3.29). Taking an arbitrary step length of 10, the chords have a length of 10

until the corner is reached. As the chords begin to traverse the corner they become shorter. The shortest chord spans from five points before the corner to five points after the corner, giving a length of 7.071. They then lengthen until the beginning of the chord has reached the corner, at which point the length is 10 again.

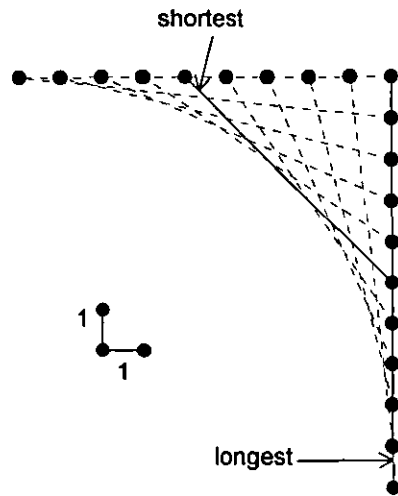
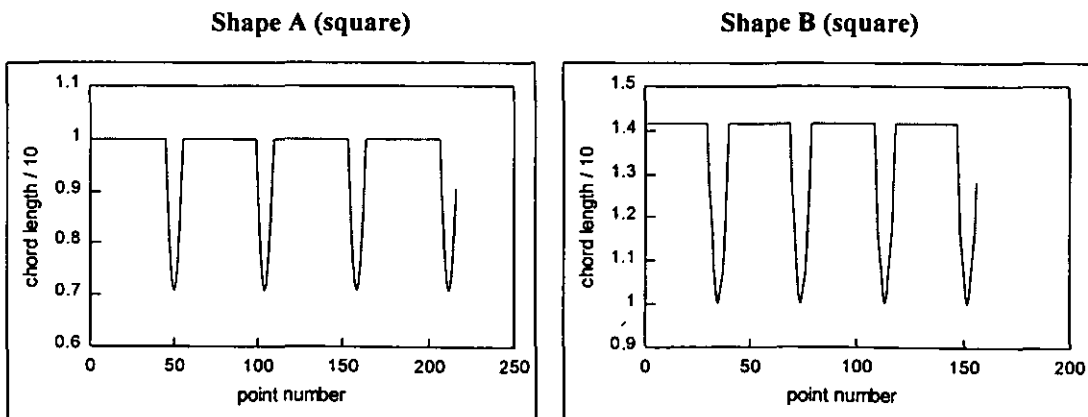


Figure 3.29 : Spanning a corner

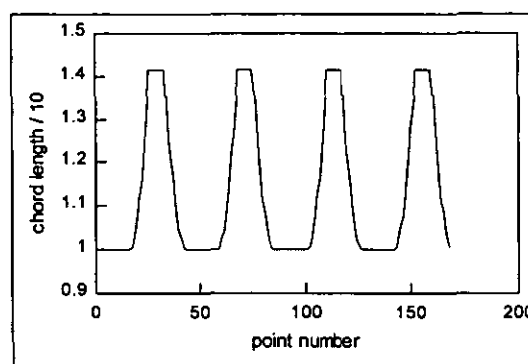
The plots of chord length against starting point for shapes A and B with a step length of 10 are shown in Figure 3.30. The analysis was conducted by beginning at the left topmost pixel and stepping clockwise with a step length of n . The chord length is the actual distance from point P_i to point P_{i+n} in the list of edge co-ordinates. The QuickBASIC program for calculating the chord lengths is listed in Appendix 4. Shape B gives the same pattern as the shape A but the distance from point P_i to point P_{i+10}

Figure 3.30 : Spanning chord plots for shapes A and B, step length 10



along a straight edge is 14.1421 and not 10, because the pixels are diagonally connected. This is not a problem when all of the pixels are diagonally connected but it highlights a flaw in the application of the method. Kaye et al [74] refer to an "equipaced" exploration of the profile. The edge pixels in shape C are not evenly spaced because some are connected edge to edge and some are connected diagonally corner to corner. Stepping 10 pixels gives a chord length of 10 on the edges aligned with the digitisation grid, and a chord length of 14.1421 on edges at a 45° angle to the grid, even though they are all "straight.". Chords spanning the corners have lengths between these two values. The plot is shown in *Figure 3.31*. The maxima and minima represent the sides of the octagon and the corners are lost in the transitions.

Figure 3.31 : Spanning chord plot for shape C (uneven spacing of points)



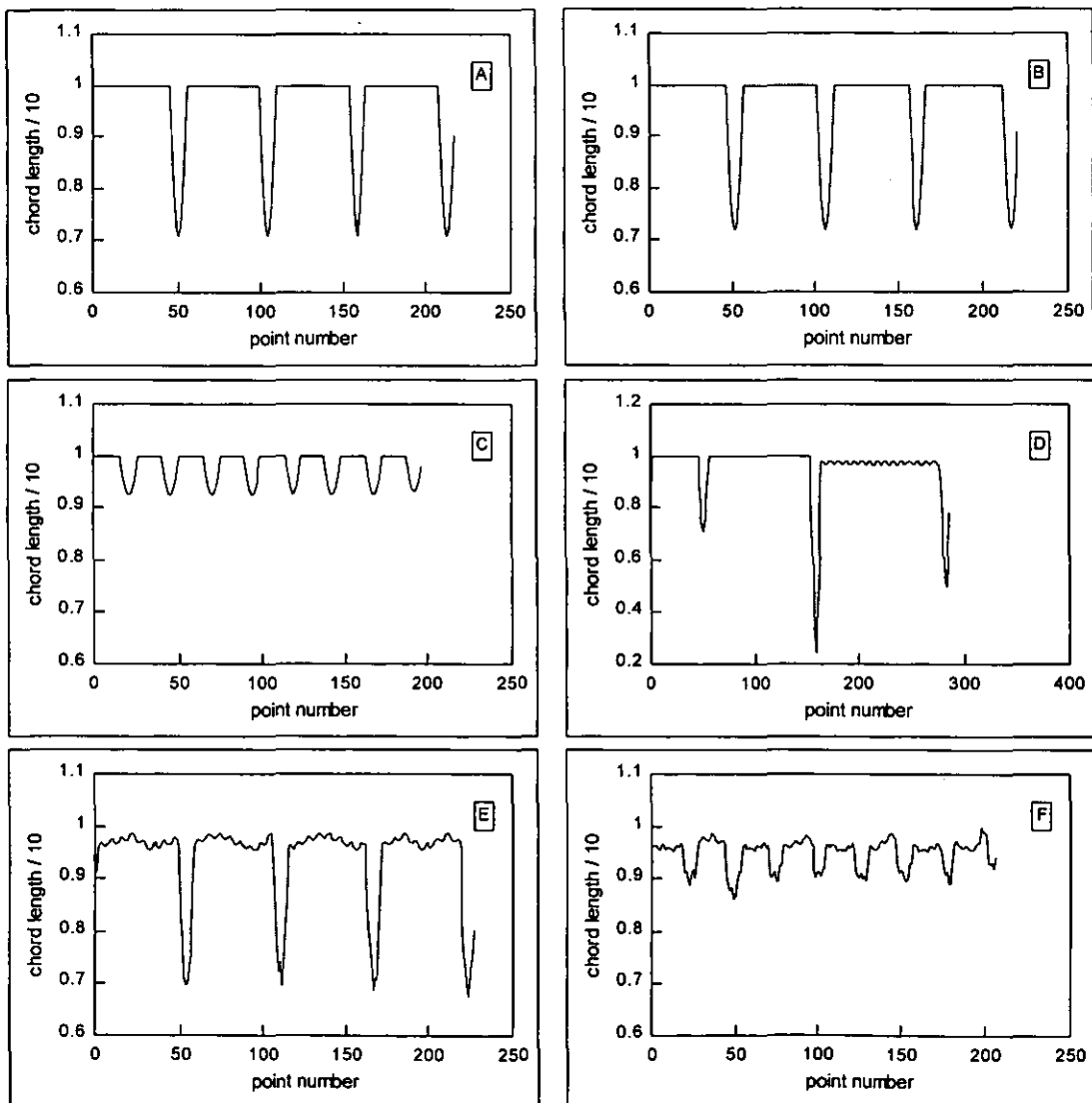
Clearly, the data is not of a suitable format for use with this method. Kaye et al rotated a vector from the centroid to the periphery at constant angular velocity to obtain a set of equiangular co-ordinates. Equiangular does not necessarily mean equally spaced along the boundary but serious problems would only be encountered if the profile contained long spikes or sharp concavities.

(A puzzling feature of the Kaye et al paper [74] is the wavy nature of the plots in Figure 7b(i) and (ii). Whether the boundary points are obtained by equiangular steps or simply taken as the co-ordinates of the outermost particle pixels, the points are equally spaced for a square and the plot should look like *Figure 3.30*. Also, if the points are equally spaced the chord length can never be longer than the step length. One can only assume that the shapes analysed by Kaye et al had more fuzzy edges than depicted and that the points were not equally spaced.)

To apply the method correctly a routine was written to interpolate between the points in the edge co-ordinate files and produce a new list of points, such that the spacing from any point to its neighbour is a fixed value. A spacing of 1 was chosen. The program is listed in *Appendix 5*. The effect of running this routine is to slightly smooth the profile while also increasing the number of points in the list. The octagon, shape C, now gives a much better plot showing eight corners of equal sharpness. The other synthesised shapes also give good results (*Figure 3.32*). Note the three different angles in the triangle, the sharpest angle having the deepest trough.

In all cases the chord lengths were normalised by the step length. The choice of a step length of 10 was made after experimenting with different values. As the step length

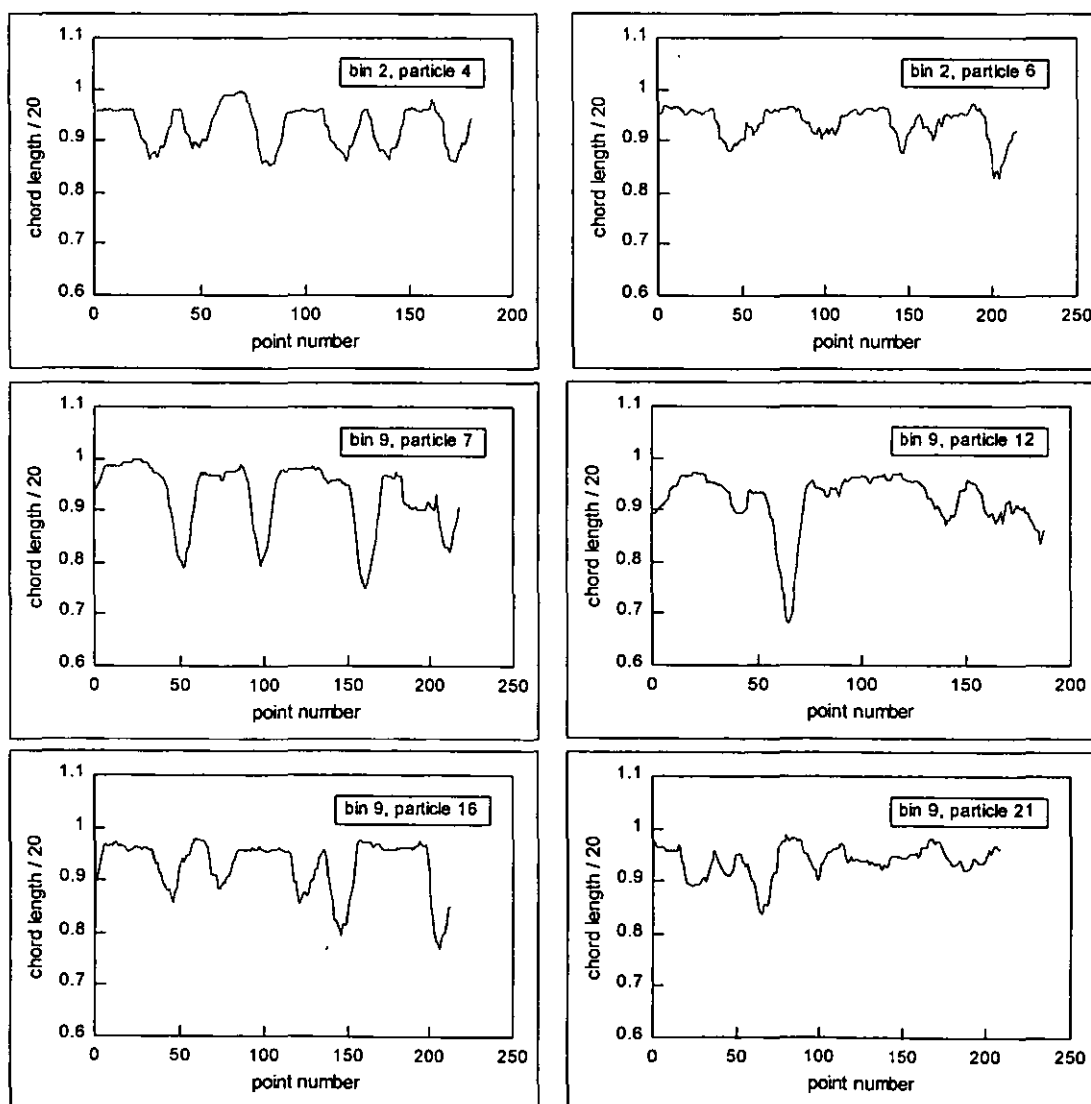
Figure 3:32 : Spanning chord plots for shapes A to E with evenly spaced points



increases the troughs broaden and there are fewer chords of maximum length. If the steps are too big some detail is lost and if they are too small the plots contain unwanted noise.

The edge co-ordinate files for the 48 particle set representing bin 2 and bin 9 were then converted and the spanning chord program was run. Because these profiles are more irregular and noisier than the synthetic shapes the step length was considered afresh and after some experimentation it was decided that 20 was suitable. Plots of some selected shapes are shown in *Figure 3.33*.

Figure 3:33 : Spanning chord plots for particles from Figs 3.14 and 3.15



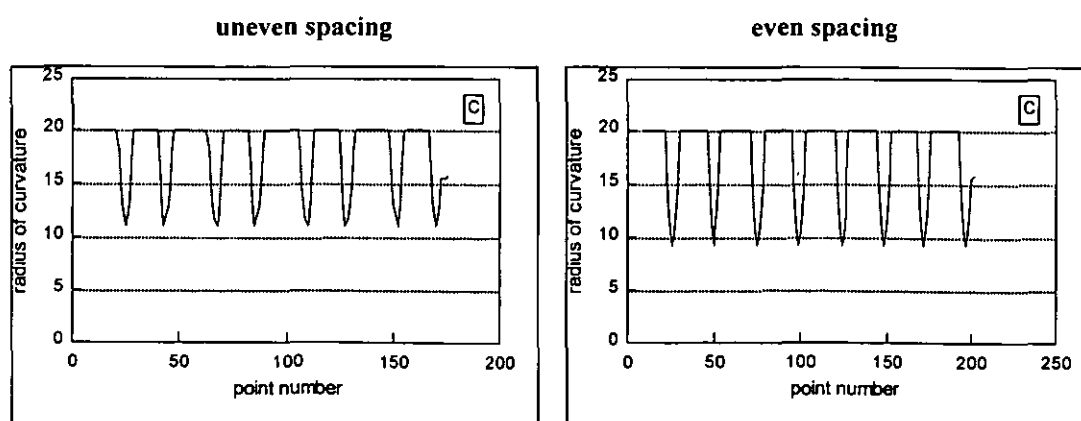
3.5.2 The Radius of Curvature Method

In this method a circle is fitted to three points and the radius is plotted against the list position of the middle point. Different levels of resolution are obtained by varying the spacing, s , between the points used for fitting the circle. For example, $s=1$ means fitting to three consecutive points, giving high resolution and showing up every undulation in the profile. Larger values of s smooth the results. The other variable to be considered is the maximum radius value allowed in the plot.

Once again QuickBASIC was used for programming (*Appendix 6*). Beginning with the synthetic shapes, the method was tried on both the original edge co-ordinates files and the new equally spaced co-ordinates files. It was found that equal spacing is not as critical as it is for the spanning chord method. The octagon shows eight corners no matter which file is used but it can be seen from *Figure 3.34* that better results are obtained with the latter. When the original set of co-ordinates is used the distance between the troughs relates to the number of pixels along the edge rather than the actual length of the edge.

By comparing the results from various values of s across a selection of real and synthetic particles $s=7$ was chosen for the plots in *Figure 3.35*. Values as low as 2 work well with the synthetic shapes but the real particles need a lower resolution to smooth out the noise. The choice of maximum value is arbitrary. Ideally the data for each particle should be plotted with a high maximum. An appropriate cut-off point can then be chosen by observation, depending on the level of detail required. For

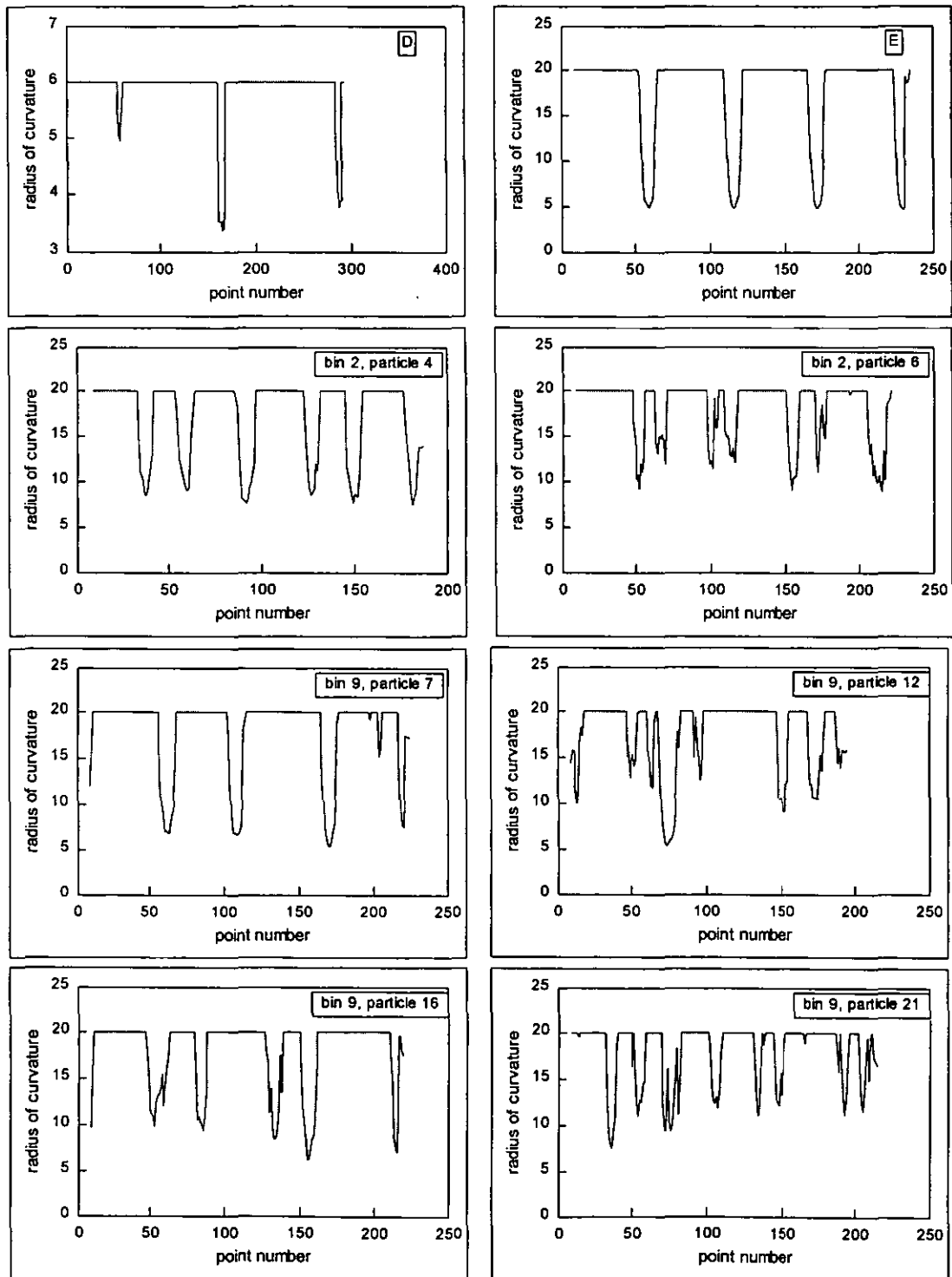
Figure 3.34 : Radius of curvature plots for shape C ($s=7$)



example, particle 7 from bin 9 would only show the four main corners if the threshold was reduced to 15.

It must be noted that no provision was made in the calculation of radius to recognise cases where the three points made a concave curve instead of a convex curve in

Figure 3.35 : Radius of curvature plots for selected shapes



relation to the centre of the particle. For re-entrant particles this would be a serious omission because there would be no differentiation between protrusions and concavities. However, for diamond particles it is not considered to be a problem.

3.5.3 Comparison Of Corner Counting Methods

Both the spanning chord method and the radius of curvature method are capable of identifying corners on diamond particles, provided the points of the profile are equally spaced, and appropriate choices of the variables are made. There is little to choose between the two methods. The plots differ slightly in appearance but give the same information. The fact that straight lines give an infinite radius makes the radius of curvature method a little untidy, so perhaps the spanning chord method is more attractive.

3.6 SUMMARY OF SHAPE EXPLORATION

At this point enough of the methods from the literature have been examined to give a good indication of the best way to proceed.

The first hypothesis of this thesis is restated:

Hypothesis 1: There exists a shape quantifier that describes meaningfully the table sorting of synthetic diamond sawgrit particles.

It has been shown in this chapter that the shape of a diamond particle can be described in many ways. Of all the methods explored the shape parameters measured by the image analysis software seem to offer the best solution in terms of ease of measurement and relevance to tabling. Axis ratio showed the best correlation with the Friatest results and is chosen as the shape quantifier that proves the first hypothesis.

Perhaps the most interesting (or at least the most gratifying) result was the way that some of the particles could be described by the relative magnitudes of the Fourier coefficients in *Figure 3.16* (page 56). However, in terms of application, it was found that the method is too complex. Interpretation of the charts in *Figure 3.16* requires some effort. The fact that only 48 particles and 2 bins were studied, compared with

hundreds of axis ratio measurements, shows that the method was time-consuming and tedious to apply. No doubt it could be automated and speeded up, but once it was discovered that the A_2 coefficient correlated with axis ratio, it was thought unnecessary to develop the method to measure the Fourier coefficients of the other bins.

Fractal analysis is unsuitable because diamond particles are not rugged.

Simple polygonal harmonics were found to exist and shape information could be gleaned from *Figure 3.26* (page 69). Again only 48 particles were analysed and problems with time and effort required are similar to those of Fourier analysis.

Methods of counting corners were explored briefly and gave good results for diamond. To make proper use of the results the analysis would have to be taken a step further. Graphical output per particle is not practical and the results for only a few of the particles could be shown here. Ideally the program would use thresholds of depth and sharpness of the troughs to come up with a number (or numbers) to describe the particles. This was not done here. One reason was that there was no obvious way to pick appropriate thresholds and a lot of guesswork, trial and error, and subjective decisions would be required. The other reason was that axis ratio offered more promise as a parameter on which to base a model, and for much less work.

The axis ratio parameter will be analysed in more detail in the next chapter, and will be used for modelling the tablesort.

4 MODELLING DIAMOND TABLING

4.1 INVESTIGATING THE MEASUREMENT OF AXIS RATIO

The initial work on axis ratio suggests that it is a suitable parameter to describe tabling. However, before attempting to use it for modelling, it was thought necessary to:

- verify the calculation of axis ratio by the software,
- investigate the effects of changing image capture conditions such as brightness, contrast, magnification and focus,
- establish an appropriate sample size.

4.1.1 Verification Of Axis Ratio

This action was thought to be necessary because a bug had been found in the software and several inaccuracies were noted in the software manual.

The twenty four bin 2 particles from *Figure 3.14* (page 54) were used to verify the software calculations. For each particle a file was opened to hold the raw greyscale data - a series of numbers where 0 represents a black pixel and 255 represents a white pixel. A QuickBASIC program was written to calculate axis ratio from these files. The details of the calculation are given in *Appendix 7* and the program listing can be found in *Appendix 8*. The program assigns the grey-level data to a two-dimensional array in x and y , with a value of 1 for pixels with a grey-level less than 20, and a value of 0 for the rest. It then calculates the centroid and the sums of the squared co-ordinates, uses the transformations from *Appendix 7* to find the moments about the principal axes of the particle, and reports the axis ratio.

The values for axis ratio reported by the image analysis software were compared with values calculated by the QuickBASIC program for the twenty-four particles. Over a range of 0.785 to 0.965 the average difference between the two methods was 0.001, with a maximum difference of 0.005. The differences arise from the definition of particle pixels. Around the edges of the particles there are pixels which are neither

black nor white and the choice of 20 as the cut-off grey-level for inclusion in the program calculations was arbitrary. The total number of pixels in a particle determined by the program was never exactly the same as reported by the image analysis package.

There is sufficient agreement between the "automatic" and "manual" methods to have confidence in the software and its measurement of axis ratio.

4.1.2 Effects Of Image Capture Conditions

Repeat measurements were made on one field of twenty-five particles from bin 2 under different lighting, focus and magnification conditions. It was found that changing the lighting by adjusting the brightness, via the software or by the aperture control on the microscope, affected readings of individual particles in the third decimal place. Refocusing, or changing the magnification between x6.5 and x25 along with refocusing, affected the second decimal place. It was concluded that focus adjustments can make a difference and that care must be taken to ensure that the image is as sharp as possible before making measurements. Brightness and contrast adjustments are not critical within a certain range, and the appearance of the image on the monitor can be used to set them correctly.

It can be concluded that individual readings of axis ratio are repeatable to two decimal places when there is reasonable attention paid to focusing the image. This corresponds to an uncertainty of ± 0.005 .

4.1.3 Choice Of A Sample Size

The average axis ratio from repeat measurements of the same field of 25 particles was also repeatable to two decimal places. Other fields of a similar number of particles on the same slide were measured but the average values from field to field agreed only in the first decimal place. Clearly, a sample of 25 particles is not sufficiently large.

To get repeatability in the mean to two decimal places the mean deviation must be 0.005 or less. The mean deviation for a normal distribution can be related to the sample standard deviation, σ , and sample size, n , by the following equation.

$$0.005 = \frac{\sigma}{\sqrt{n}} \dots\dots\dots(27)$$

By definition axis ratio has an upper limit of 1, which truncates the distribution curve. A normal distribution cannot be assumed in the lower bins where axis ratios are high. A simple exercise was undertaken to find an appropriate sample size for bin 2. Axis ratios for a total of 1040 particles from two bin 2 slides were measured, giving an average of 0.88 and a standard deviation of 0.06 (see *Figure 4.1*). The axis ratios were pooled into groups of n consecutive measurements, for various values of n between 100 and 500, and the averages of the groups were compared. 400 particles were sufficient to get an average of 0.88 every time. Looking back at *Figure 3.6* (page 43) it can be seen that the standard deviation is fairly consistent up to bin 6, so a sample size of 400 particles is appropriate for these bins.

At the upper end of the table the standard deviation is higher and larger samples will be necessary. Since the average axis ratio is further from the truncation value, the axis ratio distributions are closer to normal in these bins. The British Standard for measuring particle size distributions [97] recommends a sample of 625 particles. From equation 27 the mean deviation for a standard deviation of 0.135 (bin 12, *Figure 3.6*) and a sample size of 625 particles is 0.0054. This is a worst case example so it was concluded that 625 is an appropriate sample size for most cases of axis ratio measurement.

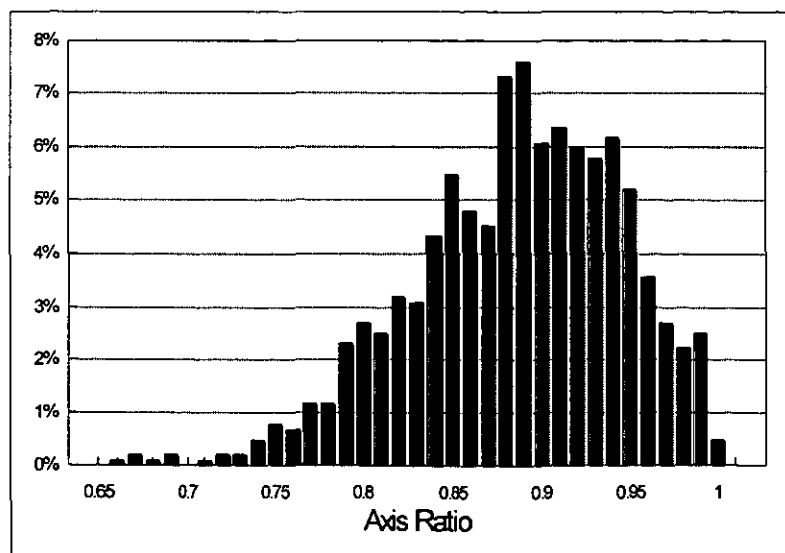


Figure 4.1
Axis Ratio Distribution
1040 particles from bin 2

average = 0.88
 std. dev. = 0.06

In summary, if the image capture conditions are set so that the image is reasonably sharp and the threshold for distinguishing particle pixels from background pixels is chosen with care, then a sample of a minimum of 400 particles will give the required precision of two decimal places in the mean axis ratio in the lower bins. For very poorly shaped material a much larger sample may be needed but a sample size of 625 particles should be adequate to give the required precision in most cases.

With this decided, the next task was to ensure that the sample is representative of the population.

4.2 SAMPLING

It is generally accepted by those involved in processing diamond that representative samples of sized and tabled fractions can be obtained using a spoon or spatula. This is because these fractions are considered to be reasonably homogeneous after sorting. However, no statistical evidence could be found to back up this assumption, so it was decided to test it for the specific case of axis ratio measurements.

4.2.1 Sampling Experiment 1

An experiment was carried out to compare the spooning sampling method with spinning riffler sampling. Given that there is a much wider range of axis ratio in the upper bins than in the lower bins, it was expected that sampling would be more critical at the poor shape end of the table. A requirement of the sampling experiment, therefore, was that the methods be compared for both good and bad shapes.

1,000 carats (200g) of bulk 40/45 grit were tabled and bins 2 and 9 were chosen as examples of good shapes and bad shapes respectively. The contents of bin 2 were divided into twenty samples using a spinning riffler. Two of these were set aside and labelled 2RA and 2RB. The others were recombined in the bin and then two samples were taken with a spoon. These were labelled 2SA and 2SB. The samples were cleaned in water in an ultrasonic bath for approximately ten minutes and then rinsed with alcohol and dried. Two slides of each of the A samples and one slide of each of

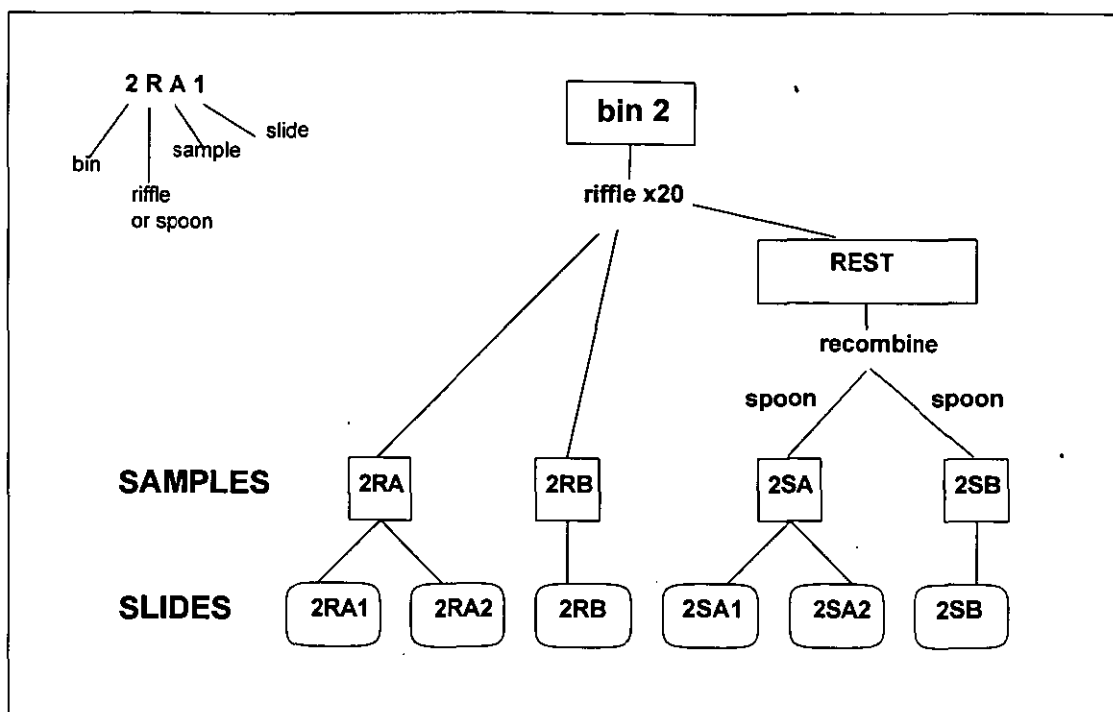


Figure 4.2 : Bin 2 sampling plan

the B samples were made up. This gave six slides, allowing the following comparisons:

- ♦ repeat measurements of one slide
- ♦ 2 slides from the same sample (2RA1 vs. 2RA2, 2SA1 vs. 2SA2)
- ♦ 2 riffled samples (2RA vs. 2RB)
- ♦ 2 spooned samples (2SA vs. 2SB)
- ♦ riffle vs. spoon (2R vs. 2S)

The diagram in *Figure 4.2* shows the sampling process and the designations of the slides.

A similar exercise was carried out for bin 9, giving six more slides. There was a slight difference in method because there was a much smaller quantity of material in the bin. The contents of five riffle tubes were combined to make each of the 9R samples, and the remaining material was recombined and divided equally between two sample jars to make the 9S samples.

Axis ratios of a minimum of 625 particles were measured on each slide and were then imported to a spreadsheet file for analysis. Using a spreadsheet t-test function, each

slide was compared with each of the others in turn. The results for bin 2 are shown in *Table 4.1* and *Table 4.2*. Where a slide is listed twice, a repeat measurement was carried out.

Table 4.1 : Axis ratios for bin 2

SLIDE	AVERAGE	STANDARD DEVIATION
2RA1	0.871	0.065
2RA1	0.868	0.067
2RA2	0.868	0.069
2RB	0.873	0.065
2SA1	0.869	0.066
2SA2	0.870	0.065
2SB	0.865	0.065

Table 4.2 : T-test results for bin 2

	2RA1	2RA1	2RA2	2RB	2SA1	2SA2	2SB
2RA1	-	0.55	0.41	0.51	0.63	0.90	0.12
2RA1	0.55	-	0.81	0.21	0.90	0.63	0.35
2RA2	0.41	0.81	-	0.14	0.72	0.48	0.50
2RB	0.51	0.21	0.14	-	0.25	0.43	0.03
2SA1	0.63	0.90	0.72	0.25	-	0.72	0.29
2SA2	0.90	0.63	0.48	0.43	0.72	-	0.15
2SB	0.12	0.35	0.50	0.03	0.29	0.15	-

Note : The values in the table are the probabilities, p , such that the null hypothesis ($\bar{x}_1 = \bar{x}_2$, where \bar{x} is the mean) can be rejected with $100(1-p)\%$ confidence. To conclude that two sample means are different with at least 95% confidence, p must be <0.05 . The shaded cells highlight the pairs of samples found to be different by this test.

At a 95% confidence level the uncertainty in the mean of a sample of size n is approximately $2\sigma/\sqrt{n}$, where σ is the population standard deviation. Assuming a worst case and taking the highest standard deviation value from *Table 4.1* gives an uncertainty of ± 0.006 . Only the averages at either end of the range in *Table 4.1* differ by more than this. The t-tests verify this, with 2SB and 2RB being the only pair

shown to be different. Clearly then, sampling is not critical for this particular shape mix, and one slide from one spooned sample can be considered to be representative.

The bin 9 results are given in *Table 4.3* and *Table 4.4* below:

Table 4.3 : Axis ratios for bin 9

SLIDE	AVERAGE	STANDARD DEVIATION
9RA1	0.734	0.112
9RA1	0.739	0.114
9RA2	0.755	0.106
9RB	0.748	0.115
9SA1	0.685	0.147
9SA2	0.691	0.152
9SB	0.698	0.139
9SB	0.699	0.141

Table 4.4 : T-test results for bin 9

	9RA1	9RA1	9RA2	9RB	9SA1	9SA2	9SB	9SB
9RA1	-	0.45	0.00	0.04	0.00	0.00	0.00	0.00
9RA1	0.45	-	0.01	0.19	0.00	0.00	0.00	0.00
9RA2	0.00	0.01	-	0.21	0.00	0.00	0.00	0.00
9RB	0.04	0.19	0.21	-	0.00	0.00	0.00	0.00
9SA1	0.00	0.00	0.00	0.00	-	0.53	0.11	0.11
9SA2	0.00	0.00	0.00	0.00	0.53	-	0.35	0.33
9SB	0.00	0.00	0.00	0.00	0.11	0.35	-	0.94
9SB	0.00	0.00	0.00	0.00	0.11	0.33	0.94	-

see note under Table 4.2

It appears from these results that there is a difference between riffling and spooning for bin 9. All of the rifflled samples have been found to be significantly different from all of the spooned samples by the t-tests. From *Table 4.3*, the spooned samples have lower averages and higher standard deviations than the rifflled samples. From *Table 4.4*, there is less agreement among the rifflled samples (top left quarter of the table) than among the spooned samples (bottom right quarter).

Although it was anticipated that a difference between riffling and spooning would show for bin 9, these results were not expected. It seems strange that a set of samples obtained from a spinning riffler would give less consistent results than a set of spooned samples. It would also be expected that, if spooning were selective, the spooned samples would contain a smaller range of axis ratios and have lower standard deviations.

A random selection of particles from samples 9RB and 9SB were viewed in a scanning electron microscope and a visual difference between the two was noticed. The spooned sample, 9SB, contained many more small fragments and broken crystals, along with more polycrystalline particles. Two possible explanations for this were considered. The first was that, because of a shortage of material in bin 9, the spooned samples were not actually obtained by dipping the spoon in once and removing a spoonful, but involved scraping the bottom of the bin and tilting the bin to help the material onto the spoon. At the time of sampling this was not considered to be invalid because, after riffling, the half that was put back into the bin should have been the same as the half in the R samples, and the only concern was to divide what was in the bin into two samples without riffling. Even if some difference was introduced in this way, the disagreement between the various riffled samples is not explained, particularly the difference seen when two slides from 9RA were compared (9RA1 and 9RA2).

The second possibility was that the ultrasonic cleaning was not consistent. Samples in individual beakers were placed four at a time in the ultrasonic bath and removed one at a time. The order in which they were cleaned was not recorded, but it is possible that the four riffled samples were cleaned together, and then the four spooned samples. Cleaning times were not equal so perhaps the four S samples were vibrated for longer and broke up more. Grit from this end of the table tends to contain twinned crystals and polycrystals, which can be broken up.

Either way, it was felt that the results from bin 9 needed to be confirmed, by repeating the exercise for bad shapes.

4.2.2 Sampling Experiment 2

A new sample of bulk was obtained and tabled. A larger bulk sample (1500 carats) and a choice of bin 8, which contained enough material for sampling, would avoid the first problem discussed above. The second could be investigated by comparing ultrasonically cleaned samples with uncleaned samples.

Sampling was carried out in a similar way to before. Two riffled and two spooned samples were taken and one slide of each was made up and analysed. 8RA and 8SB had the highest and lowest average axis ratio respectively, so these two were chosen for further analysis. Repeat measurement was carried out on these slides and then the remaining material in these two samples was cleaned in an ultrasonic bath and slides 8RAus and 8SBus were made up and analysed. The results of the axis ratio measurements and the t-test comparisons are given in *Table 4.5* and *Table 4.6*.

Looking at *Tables 4.2, 4.4* and *4.6*, the first observation is that there are more differences among these bin 8 samples (*Table 4.6*) than there were among bin 2 in the previous experiment (*Table 4.2*), which does suggest that sampling is more critical at the bad shape end of the table.

Table 4.5 : Axis ratios for bin 8

SLIDE	AVERAGE	STANDARD DEVIATION
8RA	0.830	0.085
8RA	0.827	0.088
8RAus	0.814	0.090
8RB	0.822	0.082
8SA	0.820	0.086
8SB	0.811	0.089
8SB	0.814	0.086
8SBus	0.815	0.091

Table 4.6 : T-test results for bin 8

	8RA	8RA	8RA us	8RB	8SA	8SB	8SB	8SB us
8RA	-	0.54	0.00	0.09	0.04	0.00	0.00	0.00
8RA	0.54	-	0.01	0.30	0.16	0.00	0.01	0.02
8RA us	0.00	0.01	-	0.12	0.26	0.54	0.98	0.86
8RB	0.09	0.30	0.12	-	0.69	0.03	0.11	0.18
8SA	0.04	0.16	0.26	0.69	-	0.08	0.24	0.35
8SB	0.00	0.00	0.54	0.03	0.08	-	0.55	0.44
8SB	0.00	0.01	0.98	0.11	0.24	0.55	-	0.84
8SB us	0.00	0.02	0.86	0.18	0.35	0.44	0.84	-

see note under Table 4.2

Secondly, in all cases where a repeat measurement was made on a slide (2RA1, 9RA1, 9SB, 8RA and 8SB) the comparisons passed the t-test. The two measurements were never carried out one after the other - they were on different days, or several other samples were analysed in between. This meant that the imaging conditions were set up anew for the repeats and gives some confidence in the repeatability of the measurement method.

Apart from the cleaned riffled sample, the bin 8 results come quite close to supporting the bin 9 results. The average axis ratios are generally higher for the riffled samples, and the differences found to be significant by the t-tests all involve riffle vs. spoon pairs.

Looking at the question of the ultrasonic cleaning it would appear from sample 8RA that the cleaning did indeed cause the average axis ratio to fall. Before it was cleaned this sample was out of line with the others, having a higher axis ratio. After cleaning it fitted into the set of results much better. On the other hand, 8SB was not affected by cleaning at all. One conclusion that can be drawn from this is that there really was something different about 8RA, which was solved by cleaning. Two possible sources of contamination are the tube on the spinning riffler and the sample jar. An alternative conclusion is that the range of averages obtained over a series of measurements at this end of the table will always be this large and any apparent

relationships between averages and sampling method and/or cleaning are just coincidence.

Either way, it was not proved that using a spinning riffler gives more representative samples, or that cleaning the diamond before measurement improves the accuracy. The only conclusion that can be drawn from the bin 9 and bin 8 results is that spooned samples give more consistent results than riffled samples, without seeming to lose anything. It was decided that uncleaned spooned samples would suffice for the modelling exercise.

4.3 MODELLING

4.3.1 Basis For A Model

In the literature previous attempts at modelling tabling were based on imaginary particles and assumptions about their movement on the table. Endoh [7] treated a particle as a point and numerically solved equations for three modes of motion; no relative motion, forward or backward sliding, and flight. Vibration and frictional forces determined which mode of motion applied at any particular time. The input variables were intensity of vibration, inclination of the table, and coefficient of friction of a particle on the table. The conclusion from simulations using the model was that particles with different frictional properties, e.g. spherical and non-spherical, could be separated at low vibration rate or low inclination angle.

Meloy, Williams and Rulke [13] viewed a shape-sorting table as a rectangular two-dimensional network of cells. Particles of type i had transfer functions, T_i . This was the probability that a particle of type i would move to the next cell on the right. $1-T_i$ was the probability that a particle would move down one cell. The probability that a particle would exit at a particular point at the right or bottom edge of the table could be calculated, given T_i and the number of cells along these edges. Plots of the outputs for various mono-property particle feeds were presented. Improved separation of particles with different transfer functions was predicted by increasing the number of cells. Since the cells are virtual, it was suggested that it was not necessary to increase the size of the table, but that the number of cells could effectively be

increased by tuning of the table settings. The authors admit that the model is highly simplified, in that diagonal and backwards movements are not allowed and all cells are considered to be the same. The final remark in the paper is that *...the need for the measurement of the residence times and transfer functions of particles on tables will require new and productive table experiments.*

The aim now is to construct a model based on real particles and real data. What makes this possible is the ability to assess the output of a tabling operation by quantifying the shape of individual particles. Whiteman and Ridgeway [15] characterised tabled material by measuring shape factors of individual particles, but did not go as far as using these to model the sorting. It is proposed that the table can be viewed as one cell with one input (the feeder) and twelve outputs (twelve bins) and that measurement of axis ratios will provide the data for setting up a model. The advantage of this model over those described above is that it can be applied to real particle sets.

4.3.2 Experimental Data

The results of any tabling are highly dependent on the table settings. Increasing the tilt angle (that is raising the bin 12 end of the table) causes the whole sort to move towards bin 1. Increasing the fore and aft angle (that is raising the back of the deck) causes the sort to close, which means less material gets to the end bins and more to the middle bins. This effect is greater at the bin 12 end. Lowering the back of the deck opens the sort, causing the end bins to fill at the expense of the centre bins. Higher vibration rates speed the passage of the particles over the deck and give a less effective sort because a higher proportion of the transit time is spent in flight (equivalent to reducing the number of cells in Meloy, Williams and Rulke's model). Higher feed rates give rise to more particle-particle interference.

Other variables that affect the sort are material type and particle size. By using only size 40/45 diamond from a specific type of synthesis process, these factors are kept constant. It is assumed for the time being that the bulk material does not vary significantly from batch to batch.

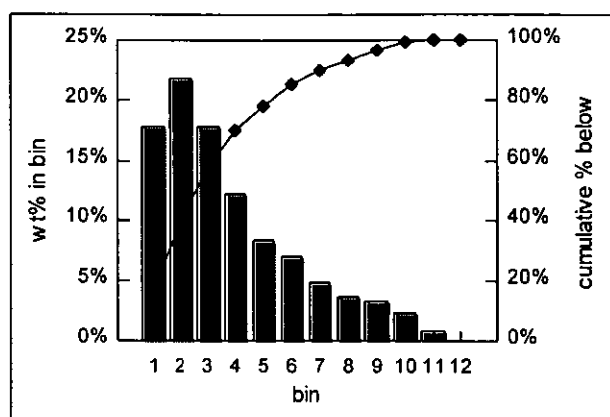
In the production environment the tables are generally set during the first few minutes of operation. Small adjustments are made to the angles until it is deemed that the spread of particles across the deck is even. There is no angle measurement built into the deck so the angles are not usually recorded. Within a size it is not known how much the settings differ from one tabling to another, or from table to table.

Using bulk 40/45 material, two tablings were carried out to give two different distributions in terms of percentage weight per bin. The tables were set up as required and then stopped so that the material which had crossed the table during the setting up adjustments could be returned to the hopper. The deck angles were then measured using a clinometer aligned in a perspex frame designed for that purpose. Feed rate was measured during set-up by catching the feed on a spoon and weighing the amount caught over a time period of one minute. The vibration rate was read from a digital display on the control panel.

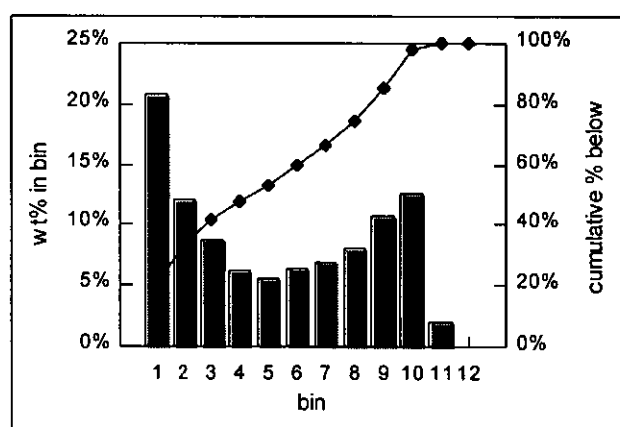
After tabling, the contents of each of the bins were weighed. The table settings and the resulting weight distributions are shown in *Figure 4.3*. These tablings will be referred to as *tb1* and *tb2*.

In the first tabling the material was biased towards the bin 1 end and in the second the distribution was opened. The distributions look very different. Assuming the bulk to be consistent it would be expected that the contents of any bin would differ in some way from the contents of the bin with the same number on the other table.

Spooned samples of the bulk material and of each of the bins were taken (except bin 12, which contained no material in both cases) and slides were made. Axis ratios of 625 particles on each slide were measured by image analysis and the data files were imported to a spreadsheet for analysis. The axis ratio distributions from bins 1, 5 and 9 of *tb1* and *tb2* are compared in *Figure 4.4*. T-tests showed that these distributions are significantly different with more than 99% confidence when compared table to table. This proves that differences between the bin contents for the two sets of tabling conditions can be quantified by measuring axis ratio. The average axis ratios and standard deviations are plotted against bin number in *Figure 4.5*. At the bin 1 end of

Figure 4.3 : Weight% distributions for *tb1* and *tb2**tb1*

material	bulk 40/45
load	1,000 carats
feedrate	14 carats/min
vibration	5.07g
tilt angle	6.32 degrees
f&a angle	4.05 degrees

*tb2*

material	bulk 40/45
load	1,500 carats
feedrate	13 carats/min
vibration	5.18g
tilt angle	6.55 degrees
f&a angle	3.55 degrees

the table *tb1* gives better discrimination on averages but most of the way across the table the distributions within the bins are tighter in *tb2*. This kind of information could be very useful in setting up a table if something is known of the desired output in terms of axis ratio distributions.

4.3.3 Setting Up The Models

There are large overlaps in axis ratio distributions from bin to bin. Given only the axis ratio of a particle it is not possible to say with certainty from which bin it came, or to which bin it would go if tabled again. However, it can be said that it is more likely to go to some bins than to others, based on the knowledge that some bins contain more particles of this axis ratio than others. In other words, for a given axis ratio there is a probability associated with each bin as a possible destination.

Figure 4.4 : Axis ratio distributions of selected bins

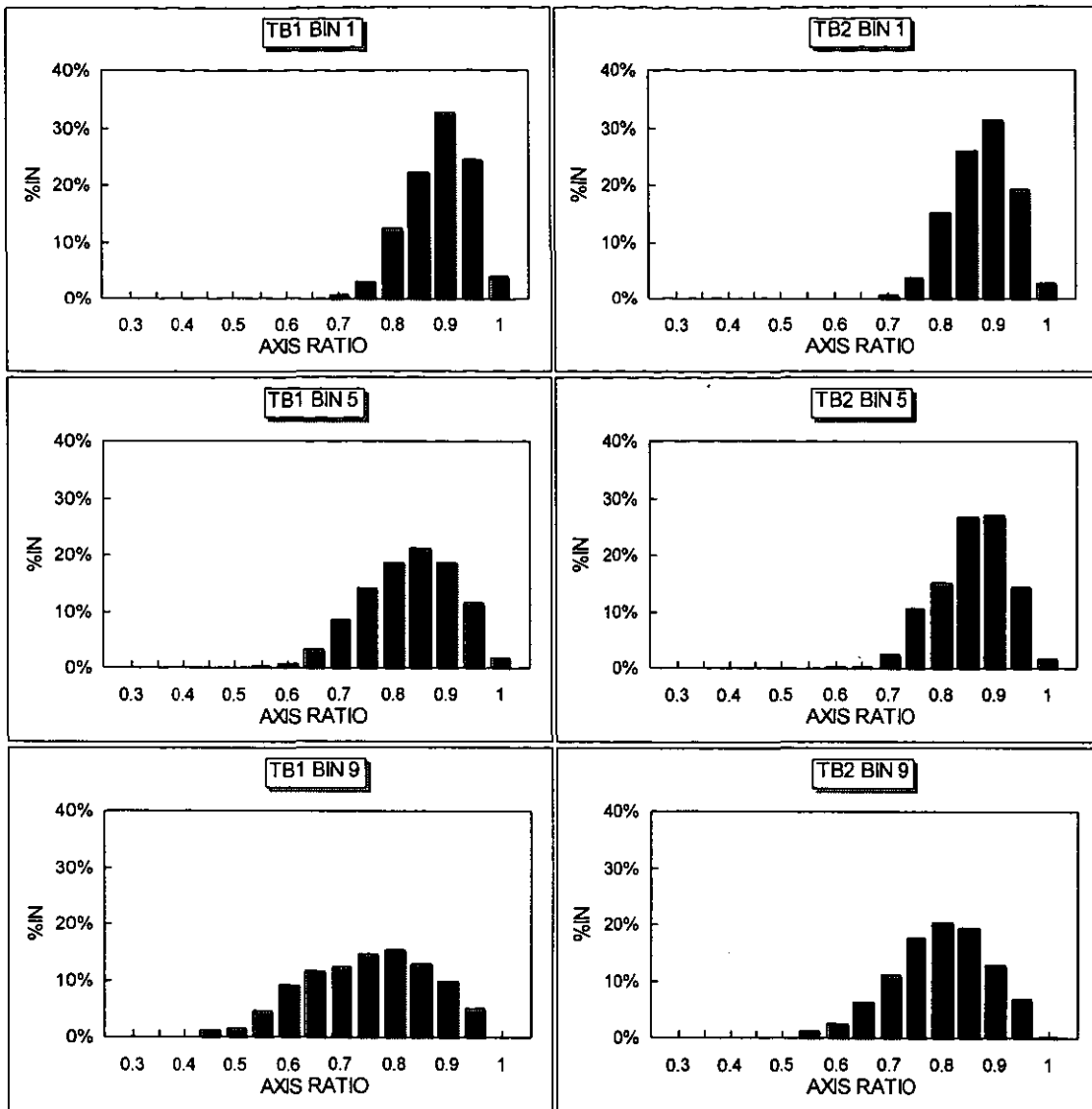
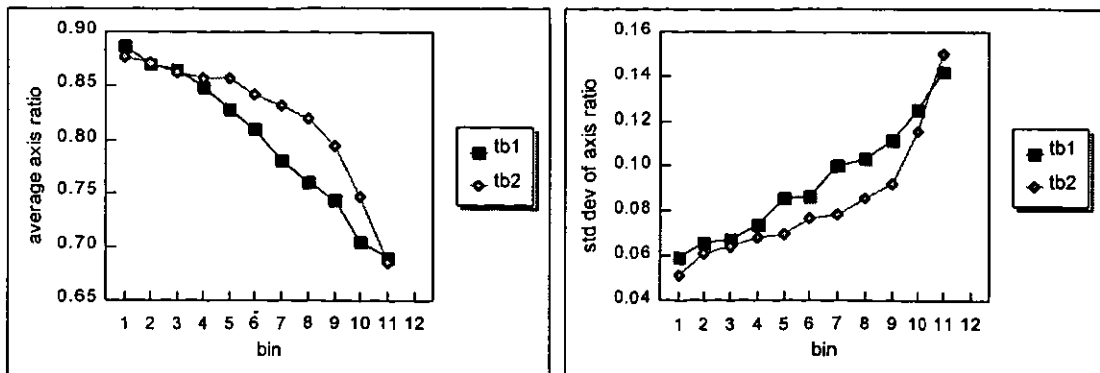


Figure 4.5 : Axis ratio averages and standard deviations for *tb1* and *tb2* compared

(a) average

(b) standard deviation



The calculation of the probabilities to model a particular tabling was carried out as follows. The range of axis ratio values was divided into intervals of 0.05, giving sixteen classes, c_i , with $c_1=0.25$ and $c_{16}=1$. These are the values at the centre of the interval so, for example, 0.5 means the interval 0.475 to 0.525. (The exception is the highest class, which ranges from 0.975 to 1.) For each of the bins the percentage distribution by class was worked out from the 625 measurements and weighted according to the percentage weight of material in the bin. This gave a set of values, w_{ij} , where i is the axis ratio class and j is the bin number. The probability, p_{ij} , that a particle in the i th axis ratio class will land in bin j is then

$$p_{ij} = \frac{w_{ij}}{\sum_{j=1}^{12} w_{ij}} \dots\dots\dots (28)$$

A set of probabilities for *tb1* was derived in this manner, and similarly, a set for *tb2*. As expected, these are quite different. The graphs in *Figure 4.6* compare the probabilities by bin for selected axis ratio classes. From these it can be seen that *tb1* is more efficient at keeping particles with high axis ratios (0.85, 0.95) at the bin 1 end of the table, but that *tb2* is better at sending the low axis ratios (0.55, 0.45) to the other end. For example, a particle with an axis ratio of 0.45 will end up in bin 10 or 11 at *tb2* settings, but could make its way to bin 7 at *tb1* settings. At axis ratios of 0.75, particles can go to almost any bin on either of the two settings, but more of them will be found in the 'good' bins at *tb1* settings, whereas *tb2* settings will send more of them to the 'bad' bins. The crossover in this case is between bins 6 and 7. For higher axis ratios the crossover is nearer the bin 1 end. As the axis ratio decreases the crossover moves towards the bin 12 end.

4.3.4 Testing The Models

One possible use of sets of probabilities is to predict the outcome of tabling for a feed sample of known axis ratio distribution. Thus, for any sample with an axis ratio distribution, b_i , where b_i is the percentage in class i , the percentage, d_j , ending up in the j th bin is

$$d_j = \sum_{i=1}^{16} b_i p_{ij} \dots\dots\dots (29)$$

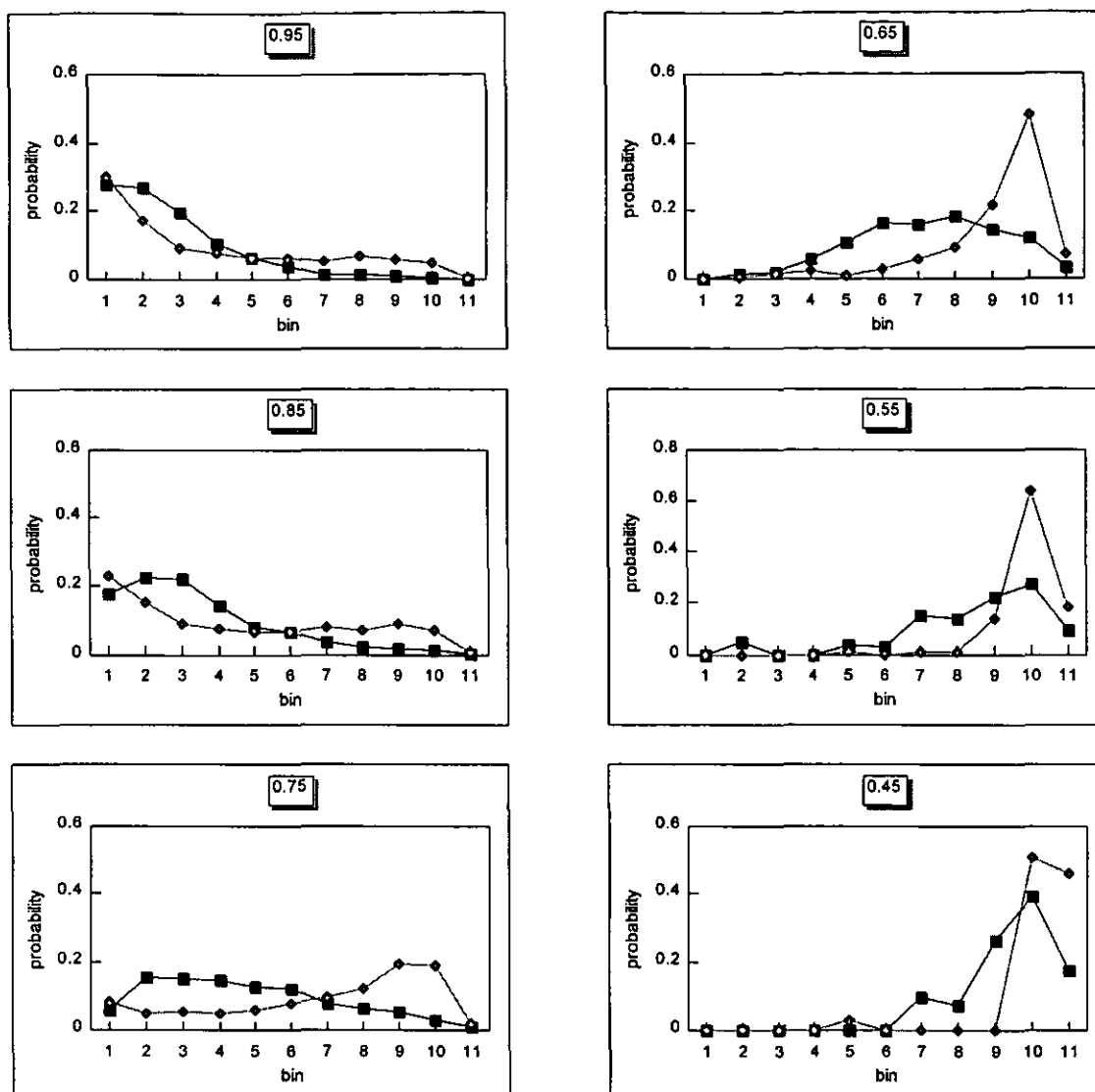


Figure 4.6 : Probabilities for *tb1* (squares) and *tb2* (diamonds) for selected axis ratio classes

One of the characteristics of tabling that has long been a source of puzzlement is the way the contents of one bin, when retabled at the same settings, spread out and distribute themselves in a wide range of bins. In past experiments with synthetic diamond [98] it has been found that the percentage of material returning to the bin from which it came is much higher (up to 80%) at the extreme ends of the table than in the centre (approximately 40%). This gives a U-shaped repeatability curve (percentage returning to original bin plotted against bin number). On the other hand, if the material is recombined and retabled at the same settings the weight distribution across the bins is repeatable to within 2%. These observations could possibly be

explained by the fact that the path of any particle across a vibrating table is based on probability.

Knowing a set of probabilities now makes it possible to retable the individual bin contents by simulation, and predict repeatability curves. Using the measured axis ratio distributions from the bin samples, and the two calculated sets of probabilities, the distributions on retabling were predicted. *Figure 4.7* shows the retabled bin distributions predicted by the two models, and the associated predicted repeatability curves.

The repeatability curves have the characteristic feature of higher repeatability in the end bins but the percentages are all lower than expected. To see what actually happens, bins 1, 5 and 9 from *tb2* were retabled.

To do this it was necessary to reproduce the *tb2* tabling conditions exactly. The first important factor was the table itself. Because of variations in deck surfaces from table to table, and differing characteristics of the accelerometers used for vibration, the same table as before had to be used. The tabling parameters were set to be as close to those of *tb2* as possible. Unfortunately, the controls for the deck angles do not allow fine adjustments so the angles were slightly different. The tilt angle was set at 6.57 degrees (previously 6.55) and the fore and aft angle at 3.56 degrees (previously 3.55). Neither can the feed rate be set precisely. It was measured this time to be approximately 14 carats per minute.

When it was judged that the *tb2* settings had been reproduced as well as was possible, the contents of bin 1 from *tb2* were tabled and the percentage weights in the bins were recorded. A similar exercise was carried out for bin 5 and then bin 9, without changing any of the settings. The actual distributions are shown alongside the predicted distributions in *Figure 4.8*. It is clear that the predictions are a long way from being correct. Much more of the bin 1 and bin 9 material returned to the original bin than was predicted, and the distribution of the retabled bin 5 has a completely different shape than predicted.

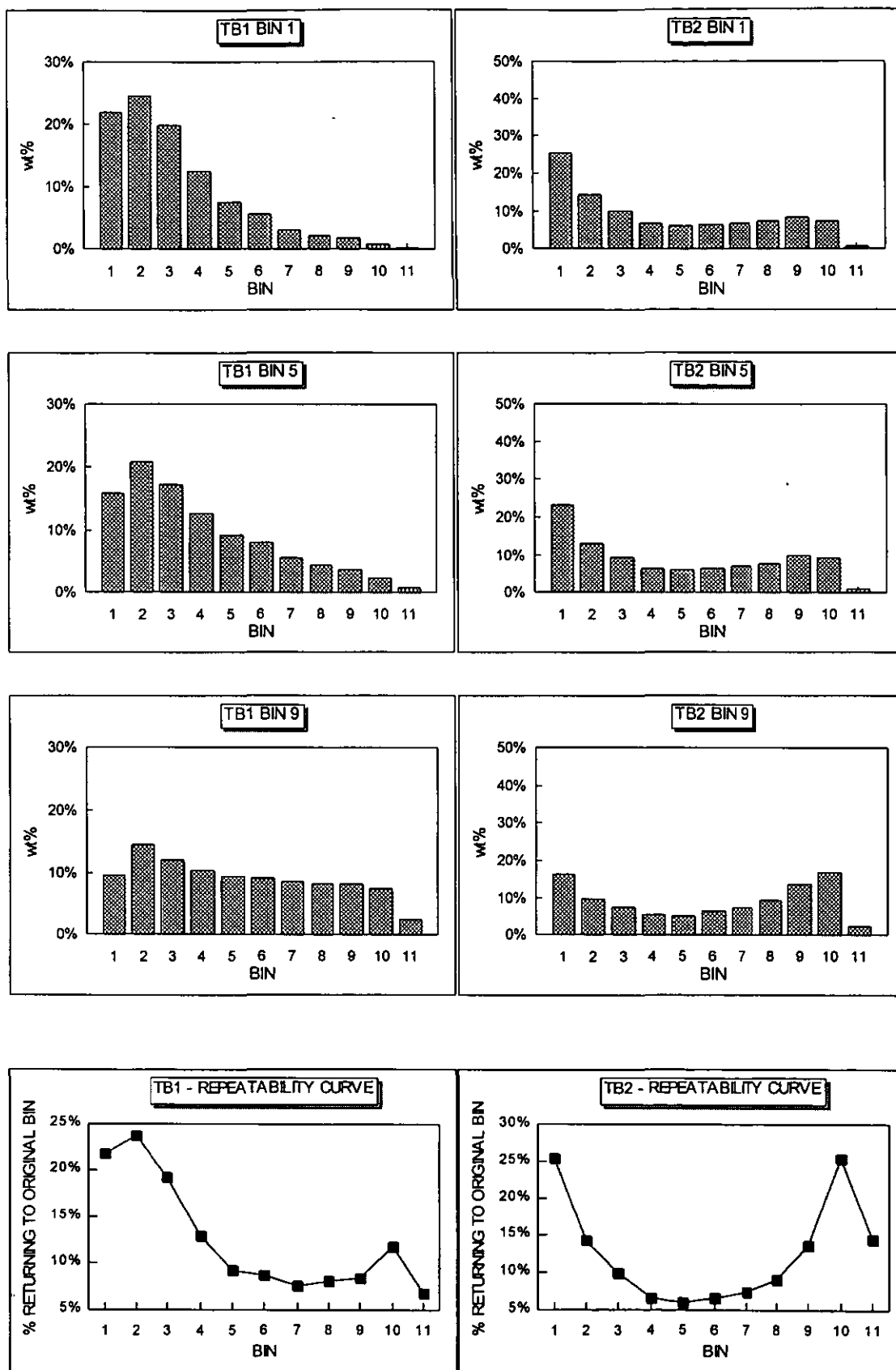


Figure 4.7 : Predicted weight distributions for retabling of selected bins and predicted repeatability curves

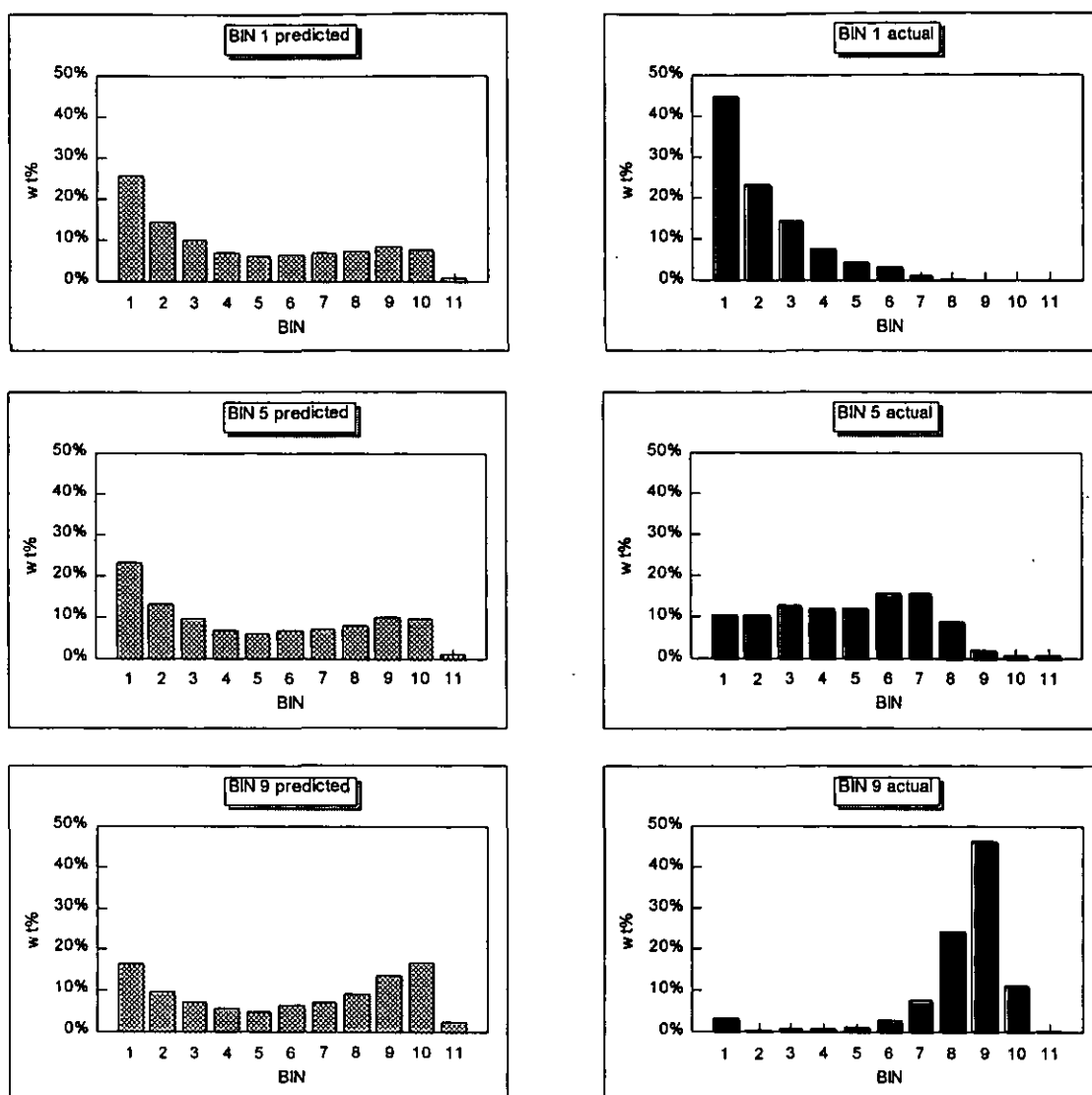


Figure 4.8 : Retabling of *tb2* bins, predicted and actual

4.3.5 Discussion

Two possible explanations for the differences between actual and predicted are:

- ♦ The table settings are so critical that slight differences in the parameters will alter the probabilities, making the model invalid as soon as any settings are changed.
- ♦ The model is too simple because it is based on one empirical result and relies only on axis ratio as the sorting property.

It is likely that the discrepancies arise from a combination of these possibilities and they will each be discussed.

- a) *The table settings are so critical that slight differences in the parameters will alter the probabilities, making the model invalid as soon as any settings are changed.*

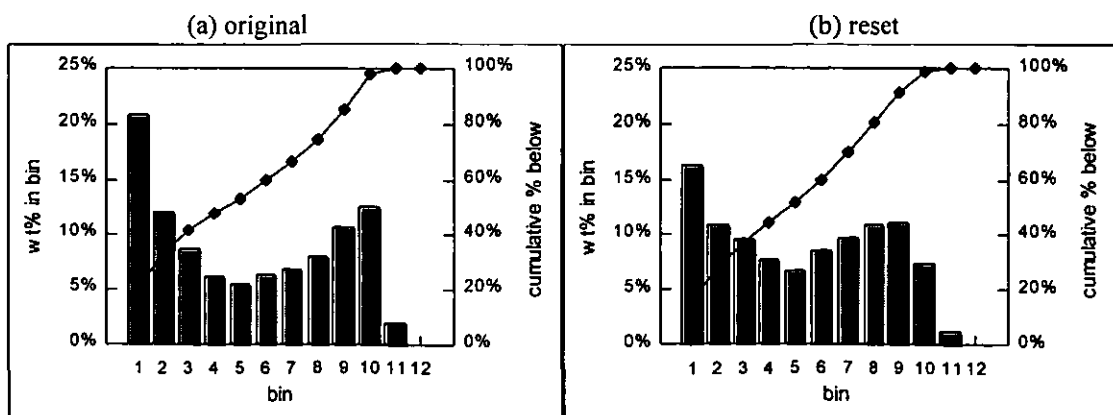
The reproducibility of the table settings was easily investigated by combining all the *tb2* material and tabling it at the current settings. If the settings had not been changed then the distribution by weight across the bins would be expected to be reproducible to within two or three percent. The results are compared graphically in *Figure 4.9*, and the differences are listed in *Table 4.7*.

Table 4.7 : Differences in distribution on retabling *tb2* material at slightly altered settings

bin	retable - original
bin 1	-4.61%
bin 2	-1.01%
bin 3	0.93%
bin 4	1.57%
bin 5	1.19%
bin 6	2.21%
bin 7	2.83%
bin 8	2.82%
bin 9	0.29%
bin 10	-5.27%
bin 11	-0.96%

Although the basic shape of the retabled distribution is similar to the original, the sort has closed slightly (meaning that the middle bins contain more material than before, while the outer bins contain less than before). It is usual on repeat tabling to find that the higher discrepancies are at the extreme ends of the table, but the differences in

Figure 4.9 : Original *tb2* and reset *tb2* distributions by bin



bins 1 and 10 are higher than would be expected on a repeat if the settings had not been altered. Differences of 2% would also be considered high in the middle bins.

The conclusion from *Figure 4.9* and *Table 4.7* is that some reproducibility has been lost because of having to reset the tabling parameters. However, this is only a small contribution to the error and does not explain the fact that the model predicted much lower percentages returning to original bins than were observed.

b) The model is too simple because it is based on one empirical result and relies only on axis ratio as the sorting property.

The real proof of a model is to predict the correct results from data that is completely independent of the data used in setting it up. This model failed the test. Going back a step, it was tested on data similar to the original data but not exactly the same. Axis ratios had been measured on the bulk sample before tabling but the bulk measurements were not used in the calculation of the probabilities.

Using the measurements from the sample of bulk material used in *tb2*, and the set of probabilities for *tb2*, equation 29 was applied to predict the weight distribution across the bins. The actual and predicted values are presented in *Table 4.8*. All of the predictions are within 0.5% of the actual. This shows that the model works when the data is similar to the data used to set it up.

Table 4.8 : Comparison of predicted (p) with actual (a) weight distribution for *tb2*

	bin 1	bin 2	bin 3	bin 4	bin 5	bin 6	bin 7	bin 8	bin 9	bin 10	bin 11
a (%)	20.88	12	8.67	6.16	5.56	6.33	6.86	8.08	10.77	12.59	2.1
p (%)	20.75	11.93	8.72	6.2	5.61	6.41	6.96	8.26	11.07	12.35	1.76
p-a	-0.13	-0.07	0.04	0.04	0.05	0.08	0.1	0.18	0.3	-0.25	-0.34

(Note: The measured bulk axis ratio distribution compared favourably with the distribution derived by adding the weighted axis ratio distributions of all the bins. This fact proves that the measurement of axis ratio is representative and repeatable.)

The probabilities in the model represent the table settings and ideally it would be possible to predict the weight distribution by bin of any feed sample at these settings

using these probabilities. This is where the model fails. It seems that when the feed distribution changes, the paths of the particles across the table are not governed by the same probabilities. This could be because the particle-particle interference is different or, more likely, the model is simply inadequate.

The model assumes that once the table settings are fixed, the only factors influencing the path of a particle are its axis ratio and an associated probability. Axis ratio is a two-dimensional measurement but the movement of a particle is a sequence of events in three dimensions, with rolling, sliding, turning in flight and landing in different orientations all taking place. It was hoped that one parameter and analysis by distribution rather than particle by particle would give enough information to describe tabling behaviour but this was not the case.

However, the model has some validity.

- ♦ It correctly predicts that the contents of a single bin will spread out to other bins when retabled.
- ♦ The reproducibility curve it predicts has the correct shape, showing higher reproducibility in the end bins.
- ♦ Axis ratio measurements show that the bin contents for different table settings differ in shape distribution - compare axis ratio distributions in *Figure 4.4* (page 94).
- ♦ The probability curves for various axis ratios (*Figure 4.6* page 96) give a good graphical description of the different sorting actions of *tb1* and *tb2*.

The latter two items open up some new possibilities for productive table experiments because they provide a new means of comparing different table settings. If the required output is defined in terms of axis ratio averages and standard deviations then these tools and some experimental design would help to find the optimum settings to achieve that output.

In summary, axis ratio measurements have been shown to be both relevant and informative, and the concept of using probabilities based on axis ratio distribution to model tabling at particular settings has some merits. The model goes some way

towards explaining the redistribution of bin contents on retabling, but fails to predict it accurately.

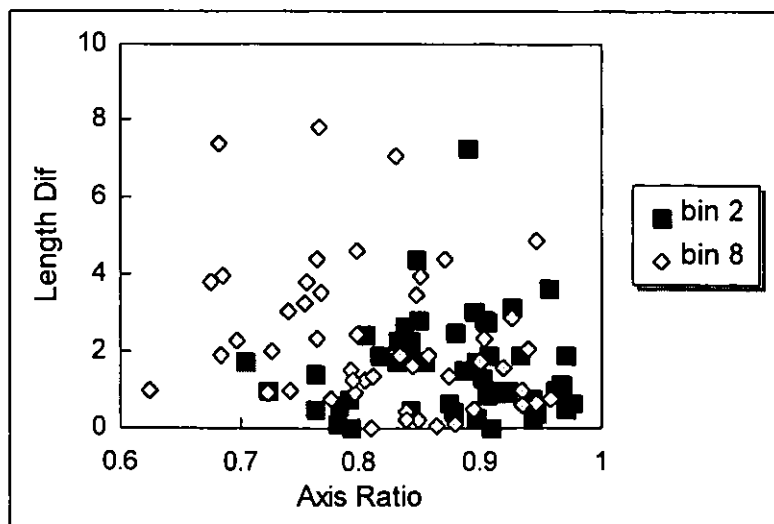
4.3.6 Developing The Model

It was decided to add a second parameter to the model in an attempt to improve its performance. Length dif (see Chapter 2) was chosen as a second parameter. Scatter plots of axis ratio against length dif showed little correlation between the two parameters so they are assumed to be independent. *Figure 4.10* is a plot using approximately fifty particles from bin 2, and the same from bin 8, from the reset *tb2* tabling.

To include length dif in the modelling process the classes had to be defined by a combination of axis ratio and length dif. The simplest way to do this was to double the number of classes by dividing each axis ratio class into two - one with length dif greater than a given value and the other with length dif less than that value. As an initial guess the value chosen was the median of the length dif values of the bulk sample. This value was 1.2.

The model was reconstructed from the bulk tabling data using the larger set of classes and new predictions were made for the retabling of the contents of individual bins. These predictions were not much different from those based on axis ratio alone. Other values for dividing the data on length dif were also tried and the reproducibility

Figure 4.10 : Scatter plot showing length dif and axis ratio to be independent variables



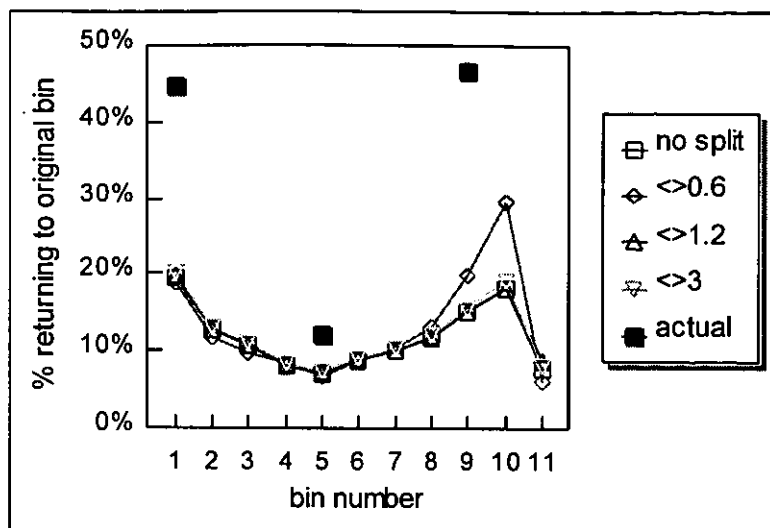


Figure 4.11 : Reproducibility curves for various axis ratio/length dif models

curves are plotted in *Figure 4.11*. Splitting at a higher value, such as 3, failed to give any improvement. Splitting at 0.6 predicted higher reproducibilities for bins 9 and 10, but still fell short of the actual results.

Since this method of modelling was quite cumbersome it was thought to be futile to attempt to complicate it any further by adding more classes or more parameters. By now it was obvious that even though axis ratio is a dominant factor, the movement of a diamond particle on a vibrating table is influenced by many parameters and that prediction of tabling requires a more complex model.

It was decided that it may be more appropriate to apply a data analysis method, such as artificial intelligence, to the problem.

5 ARTIFICIAL INTELLIGENCE

Although there is overlap between table bins when any one parameter is measured there is always the possibility that an appropriate combination of parameters would provide a unique description for each bin. An expert system and a neural network were used to explore this possibility.

5.1 EXPERT SYSTEM

An expert system is a software system in which a set of rules is applied to a set of inputs to make a decision on the outcome. Such systems were designed to imitate an expert in a given field by capturing the expert's knowledge in the rules. Some practical applications include medical diagnosis and machine fault diagnosis. In these applications the inputs would be the answers to questions such as "Does your head hurt?" or "Is the green light on?".

The purpose of this expert system is to classify particles into bins using shape parameters as inputs. A QuickBASIC program was written, following guidelines from a textbook [99].

Using i variables or inputs and allowing j possible outcomes requires an array of rules $r(i,j)$. The predicted outcome for a particular set of inputs, V_i , is the j th outcome corresponding to the highest $d(j)$ where

$$d(j) = \sum_i V_i r(i,j) \dots\dots\dots (30)$$

Initially all the rules are set to zero. The system is trained by presenting sets of inputs and allowing it to guess the outcome. If the guess is wrong the rules are adjusted by adding or subtracting the input values as appropriate. For example, if the correct outcome is $j=W$ but the expert guesses wrongly then V_i is added to $r(i,W)$ and subtracted from any $r(i,j)$ where $d(j)$ was greater than $d(W)$. Training continues until some predetermined stopping criterion is met. The system can then be tested with a new but similar set of data and the percentage of correct outcomes gives a measure of its performance.

5.1.1 Setting Up The Expert System

An existing data set from an unrelated exercise was suitable for experimenting with an expert system and saved the tedium of making image analysis measurements. The data consisted of measurements of four parameters on 600 particles from each of bins 1 and 9 of a standard tabling of size 50/60. The parameters that had been recorded were axis ratio, length dif, roundness and area. The values for each variable were normalised as follows

$$V_{norm} = \frac{V - V_{min}}{V_{max} - V_{min}} \dots\dots\dots (31)$$

so that the range for each variable was 0 to 1. A fifth parameter, the correct outcome, was assigned to each particle; 1 for bin 1 and 2 for bin 9. Every tenth case was then removed from the data file and stored in a separate file to be used later for testing the expert. This gave a training set of 1080 cases and a testing set of 120 cases, each set having 50% with outcome 1 (bin 1) and 50% with outcome 2 (bin 9).

The procedure for training and testing the expert system is as follows. Examples are picked at random from the training set and the rules are applied to predict an outcome. If the prediction is correct nothing changes but if it is incorrect the rules are altered. After a specific number of examples the training stops and the test cases are presented one by one. The predictions are compared with the correct outcomes and the percentage of correct predictions is reported.

The stopping criterion that determines when training is complete is simply the number of training examples specified in the program. Choosing a high enough number is a way of ensuring that the expert has every chance of training itself to perfection, but does not guard against over-training. The progress can be monitored by interrupting the training at intervals to test the rules. It was found that after quite a small number of examples (less than the total number in the training set) the improvement stopped and the percentage of correct predictions just fluctuated widely. The order in which the examples were presented had a much greater effect on the results than the number of examples.

This is easily explained. The examples are picked randomly and there is nothing in the program to prevent any particular case being presented more than once. Neither is there anything to ensure that every example is seen. When several consecutive cases are from the same class the rules may not change and there is no benefit gained from these cases. The combination of these factors means that the training can be very different every time the program is run, even though the training set is the same. It would be possible to constrain the training by selecting each example once and only once, but this would not solve the problem entirely. Any further restrictions, such as alternating between classes, are not desirable because then the result would be too data-specific. Ideally the expert should have a general capability and should converge on a set of rules after sufficient random examples.

Rather than restricting the training mode the program was allowed to keep selecting at random from the training set, in the hope that the random order would not influence the results as much when the number of cases presented was very high. The program was allowed to run overnight, going through several million examples and testing after each million. The results still fluctuated and the rules showed no sign of converging. *Figure 5.1* shows the performance after every hundred cases up to five thousand cases and *Figure 5.2* shows the performance after every million cases up to sixteen million. These graphs are similar and show that extra training with the same data set does not guarantee any improvement in performance.

The only consistent feature of the rules was that the signs were almost always the same regardless of the number of training examples seen. There was only exception in all the rule sets seen. With only two possible outcomes, the rule for outcome 1 is -1 times the rule for outcome two for each of the variables. It was found that for axis ratio the rule was always a positive number for bin 1 and a negative number for bin 9, while the rules for the other three variables were always the other way round, i.e. negative for bin 1 and positive for bin 9. The magnitude of the rules varied considerably. *Table 5.1* lists some of the rule sets obtained from various efforts to train the expert. They are ranked in order of performance, all having been tested with

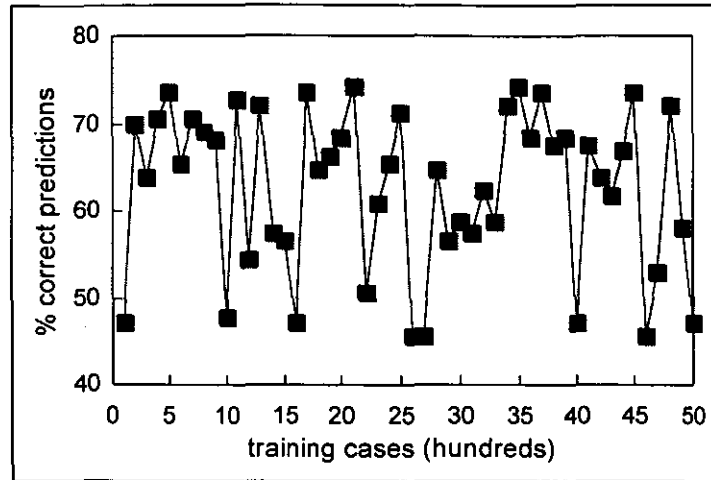


Figure 5.1 : Expert's performance up to 5,000 training cases

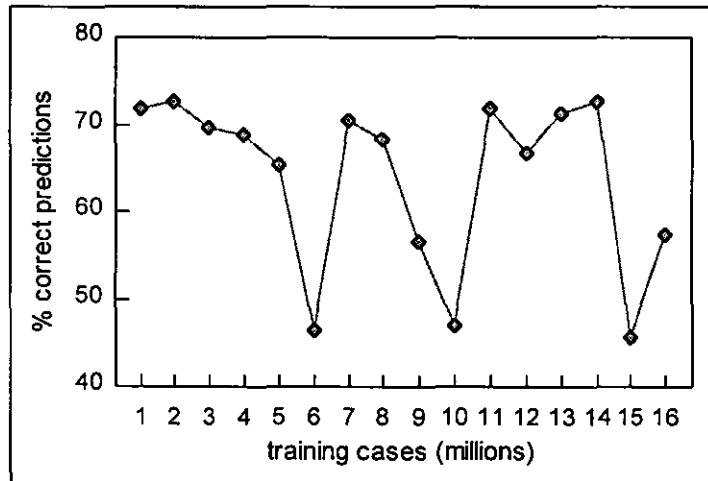


Figure 5.2 : Expert's performance up to 16,000,000 training cases

the same test data. Only the bin 9 rules are shown, since the rules for bin 1 are the same except for the sign.

Table 5.2 contains averages of the rules which gave >80%, 70-80% and <70% performance respectively, along with the overall average. It is interesting to note that applying the averages gives better than 80% correct predictions, even with the <70% average.

Table 5.1 : Expert's rules $r(i,j)$ for $j=2$ (bin 9) for 50/60 bins 1 and 9 .

<i>performance</i>	<i>r(1,2) area</i>	<i>r(2,2) axis ratio</i>	<i>r(3,2) symmetry</i>	<i>r(4,2) roundness</i>
86%	2.307	-4.148	4.612	1.219
85%	2.104	-4.435	5.295	1.489
85%	1.235	-4.604	5.254	2.018
85%	2.423	-4.158	5.648	0.859
84%	2.923	-4.909	4.868	1.584
83%	3.168	-4.567	4.124	1.034
83%	1.087	-4.132	5.880	1.514
80%	3.002	-4.576	5.193	1.556
80%	1.760	-5.130	3.930	2.203
77%	1.102	-2.825	5.542	0.887
77%	2.321	-4.144	6.221	1.407
76%	1.426	-3.312	4.913	1.447
74%	1.350	-1.870	1.921	0.702
74%	2.101	-4.667	5.009	0.770
74%	2.479	-4.978	6.167	0.153
74%	0.816	-4.277	5.537	0.983
73%	1.310	-4.815	5.462	0.951
71%	2.111	-4.928	5.378	0.432
71%	1.308	-4.051	4.779	0.464
70%	1.545	-2.247	1.054	0.318
69%	2.347	-5.042	4.298	0.697
65%	1.685	-4.091	5.231	-0.312
65%	2.587	-5.489	4.402	0.425
61%	1.600	-5.195	4.680	0.599
59%	1.477	-1.413	1.712	0.461
59%	3.492	-4.441	3.249	2.486
57%	2.034	-3.547	4.679	2.072
54%	1.593	-1.240	2.363	0.330

Table 5.2 : Performance of averaged rules

<i>averaged</i>	<i>r(1,2) area</i>	<i>r(2,2) axis ratio</i>	<i>r(3,2) length dif</i>	<i>r(4,2) roundness</i>	<i>performance</i>
>80%	2.307	-4.148	4.612	1.219	86%
70-80%	2.104	-4.435	5.295	1.489	81%
<70%	1.235	-4.604	5.254	2.018	82%
all	2.423	-4.158	5.648	0.859	82%

It appears from *Table 5.2* that the performance of the expert is greatly improved by averaging several sets of rules. This theory was investigated by modifying the training program to include an averaging step. After each 1,000 examples the rules are added to a running total then reset to zero. This is repeated a number of times and the averages are taken. The program was run ten times with no averaging, ten times averaging five sets of rules and ten times averaging twenty sets of rules. *Table 5.3* demonstrates the improvement this gives for this particular dataset.

Table 5.3 : Performance by training with averaging - 50/60 bins 1 and 9

1 only	average of 5	average of 20
82	81	81
58	82	82
73	84	83
86	83	86
62	85	86
75	81	86
64	84	85
77	74	86
75	83	83
82	74	82
range 62-86%	range 74-85%	range 81-86%

With averaging of twenty trials the inconsistencies associated with the random order of presentation of training samples have been eliminated and the expert now trains itself to the same level of proficiency each time, at least for this dataset. (Changing the files so that the test set was every ninth instead of every tenth case from the mother file gave similar results. This was done to make sure there were no dependencies on the one test set used up until now.)

5.1.2 Expert Results

The program (listed in *Appendix 9*) was now ready to tackle some new data. The bin samples from the retabling of *tb2* were used to assess the capability of the expert to distinguish between the different bins in a tabling of bulk 40/45 material. As before

the image analysis data was stored as lists of the four parameters and a class, and every tenth case was moved to a test file. The program was run ten times for certain combinations of bins and averaging twenty sets of rules. The performance was again measured as the percentage of correct predictions when the averaged rules are applied to the test data. The performance ranges over ten trials are presented in *Table 5.4*.

Table 5.4 : Expert's range of performance over ten trials

bins 1 and 9	71% - 75%
bins 2 and 8	60% - 67%
bins 2 and 5	54% - 60%
bins 1 and 2	50% - 55%
bins 8 and 9	56% - 60%
bins 2, 5 and 8	44% - 48%
bins 1, 5 and 9	44% - 48%

The following points are noted:

- Bins 1 and 9 from this tabling are not as well discriminated as bins 1 and 9 from the routine production tabling of 50/60 used in setting up the expert. This could be a size effect or it could be related to the table settings.
- The first three rows of *Table 5.4* show that the performance gets worse as the bins get closer together.
- With only two outcomes a performance of 50% could be expected with random guesses so the expert cannot distinguish between neighbouring bins 1 and 2.
- The performance for bins 8 and 9 is slightly better than for bins 1 and 2, showing that there is better discrimination at the poor shape end of the table.
- When presented with three possible outcomes the expert gets less than half of them right and performs no better with bins 1, 5 and 9 than it does with bins 2, 5 and 8. The number of correct predictions is higher than it would be by chance, but is too low to be of much use.

The expert has not shown itself to be any better at classifying diamond particles than any of the methods tried earlier. The observations listed above do not reveal anything

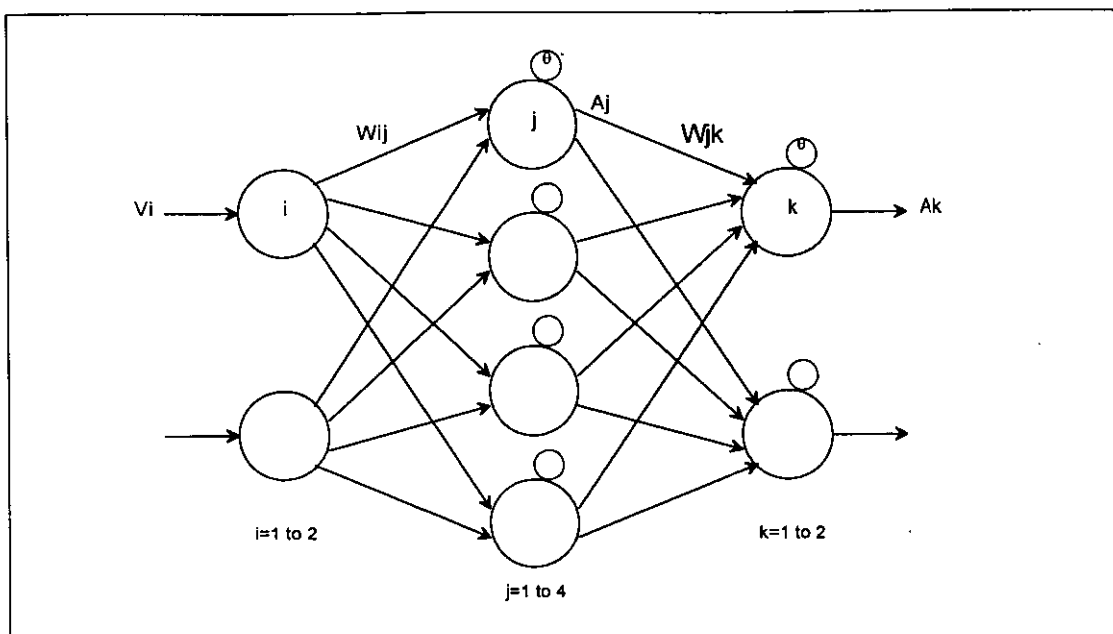


Figure 5.3 : Example of a neural network

new about shape sorting on a vibrating table. They merely confirm the perception of tabling as an imprecise and probabilistic operation.

5.2 NEURAL NETWORK

An alternative form of artificial intelligence is the neural network, a computing system made up of a number of simple, highly connected processing elements called nodes. As in the expert system the links are weighted and the input to a node is the summed product of the weights and the outputs from the previous layer. Between the input and output nodes there can be any number of hidden layers.

5.2.1 A Feedforward Network With Training By Back Propagation

Figure 5.3 illustrates a feedforward network with two inputs, two outputs and a hidden layer with four nodes. The input nodes take on the given values of the variables, normalised to fall within the range 0 to 1. The input to node j in the hidden layer is

$$I_j = \sum_i v_i w_{ij} \dots\dots\dots (32)$$

The activation level, or output, from hidden node j is calculated by

$$A_j = \frac{1}{1 + e^{-(I_j - \theta_j)}} \dots\dots(33)$$

where θ_j is a threshold or bias value for node j . This activation function is an example of a sigmoid function¹ and gives an output in the range 0 to 1, as illustrated in *Figure 5.4*. The inputs to any additional hidden layers, and

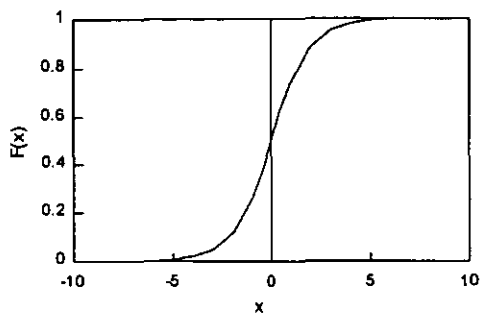


Figure 5.4 : Activation function

finally to the output nodes, are calculated in a similar manner using the outputs from the previous layer and the appropriate weights, and then are passed through the activation function along with the appropriate threshold value. If the neural network is being trained as a classifier then the output node with the highest activation denotes the winning class.

At the start of training the weights and thresholds are set randomly between certain limits. Examples are presented to the network and if the outcome is not correct then an adjustment is made to the weights. (The thresholds can be considered as additional weights.) The adjustment is in proportion to the error in the outcome. This form of training is called back propagation. First, the weights associated with the output nodes are altered, according to the following equation:

$$new\ w_{jk} = old\ w_{jk} + \eta\delta_k A_j + \alpha\Delta w_{jk} \dots\dots\dots(34)$$

where η is the trial independent learning rate, δ_k is a parameter related to the error at node k , α is a momentum term, and Δw_{jk} is the previous change for this weight. The changes for the hidden layers use the same equation, substituting i and j for j and k . The difference is in δ_k and δ_j . The desired outcome at the output nodes is known and δ_k is calculated as

$$\delta_k = A_k(1 - A_k)(A_d - A_k) \dots\dots\dots(35)$$

¹ A sigmoid function is a bounded differentiable real function that is defined for all real input values and that has a positive derivative everywhere. It rapidly approaches a fixed finite upper limit asymptotically as its argument increases and a fixed finite lower limit asymptotically as its argument decreases. The central portion is assumed to be roughly linear and its slope is called the gain of the sigmoid.

where A_d is the desired activation and A_k is the actual activation of the output node. There is no way of knowing what the activations of the hidden nodes are supposed to be so δ_j is based on a combination of the errors in the output layer.

$$\delta_j = A_j(1 - A_j)\sum_k w_{jk}\delta_k \dots\dots\dots(36)$$

This particular back propagation method is called the delta rule, or Widrow/Hoff learning. In theory, this method converges to the optimum weight vector from any starting point. The weight change can be made after every training case, but it is sometimes beneficial to present a batch of examples and use the average error in the corrections.

There are many other ways to set up a neural network but they will not be discussed here. The reader is referred to some introductory texts on the subject for further information [100-104]. The type of network described above was chosen because it is the most general and basic type and the application is a straightforward classification system.

The main differences between a neural network and an expert system are the presence of the hidden layer and the relationship between the weight changes and the error. It was hoped that a neural network would give a better performance than the expert system because of these differences.

5.2.2 Setting Up The Network

Unlike the expert system, where the only design consideration was when to stop the training, there are many variables to be considered in a neural network. These can be listed as follows:

- ♦ number of hidden layers,
- ♦ number of nodes in each hidden layer,
- ♦ range for initialising weights and thresholds,
- ♦ learning rate, η ,
- ♦ momentum term, α ,
- ♦ batch size,

- ♦ stopping criterion.

Since neural networks can be applied to a vast range of applications there are no hard and fast rules for choosing the parameters. The textbooks give some general guidelines for starting off but they don't necessarily agree with each other. A neural network is essentially a black box and there is an amount of trial and error required to get one working. Without going into the details of the trial and error process, the following conditions were found to give the best results in this application, based on the same data used to develop the expert system.

- ♦ One hidden layer, because the general advice is not to complicate the system without a specific reason.
- ♦ The hidden layer has two nodes more than the input layer. If there are too few the network may train but will not perform well with noisy data. If there are too many the network will not generalise well.
- ♦ Weights initialised between -1 and 1.
- ♦ $\eta=0.7$ If this parameter is too big the network gets paralysed and if it is too small the network will not converge.
- ♦ $\alpha=0.9$
- ♦ batch size = 10
- ♦ As with the expert system training stops after a specified number of training cases have been seen.

There was also a problem in deciding on how to quantify the error in the outcome. The desired outcome is that the node corresponding to the correct outcome would have the highest activation. If this happens then there is no error. If the output node x has the highest activation level and y is the correct class then an error for each node must be quantified. The ideal outcome would be $A_x=0$ and $A_y=1$ and all the other $A_k=0$. The error for node x could be $0-A_x$ and for node y could be $1-A_y$. The other nodes have an error of 0 if their activations are already less than A_y , otherwise the error is $0-A_k$. Alternatively, given that the winner need not necessarily have an activation of 1, but just needs to have the highest activation, the error could be taken as the difference between A_x and A_y , with a positive error for node y and a negative error for node x . Other nodes with $A_k>A_y$ would have an error of A_y-A_k . Both of these

options for quantifying the error were tried and there was not much difference in the results. The method using 1 and 0 was maybe marginally better and so was chosen.

As with the expert system, problems with variability in performance were encountered. There seemed to be a high dependence on the set of random starting weights (and possibly the random order in which the training examples were presented as well). After an initial improvement the network would achieve a certain performance level and would not improve any more no matter how long it was left to keep feeding itself on the training set. This performance level changed if the program was re-run with a new set of starting weights. The only way out of this problem was to first run a preliminary short training, repeat it several times, and store the set of weights which gave the best results on the test set. This then became the starting set for the real training. It was found, though, that little improvement could be achieved with further training. The best result from, say, fifty short trainings was as good as could be attained.

5.2.3 Neural Network Results

The QuickBASIC program is listed in *Appendix 10*. On the 50/60 bins 1 and 9 data the best result obtained in the verification step was 86%, the same as the expert system's best result. *Table 5.5* shows some results from the 40/45 *tb2* data compared with the best of the expert system results. In each row the figure given for the neural network is the best of fifty short training trials, where one trial consists of 1,000 training examples presented in batches of 10.

Table 5.5 : Neural Network vs. Expert System for tabled bulk 40/45

	Neural Network	Expert System
bins 1 and 9	77%	75%
bins 2 and 8	76%	67%
bins 2 and 5	60%	60%
bins 1 and 2	61%	55%
bins 8 and 9	61%	60%
bins 2, 5 and 8	53%	48%
bins 1, 5 and 9	51%	48%

The neural network shows a slightly better performance than the expert system for some of the combinations of bins but the hoped-for vast improvement was not achieved.

5.3 PREDICTING TABLING

The expert system and neural network classifiers have been judged on whether or not they can predict the source or bin number of an individual particle. The poor performance suggests that, even when particle shape is defined by a combination of parameters, there is too much overlap between the bins for a classification system to work, or at least that is the case with this combination of four parameters. It is not known whether this is the most appropriate set of parameters to use or if a set exists that would make classification of single particles by bin number possible. Some attempts were made to vary the number of parameters - area was excluded from the expert system and the neural network was tried with just axis ratio and roundness, but no significant improvements could be found. Without more exhaustive testing it cannot be concluded that the particles cannot be classified, but it seems likely that there will always be overlap between the bins no matter how the particle shapes are defined.

The ultimate test on both of these artificial intelligence systems would be to train them on data from all of the bins and then see what distributions they predict when presented with data from a bulk sample. In this test there is no right or wrong answer for a given particle and the performance can be judged on the distribution by bin. Despite the poor performances recorded with single particles there was still a chance that a bulk analysis would work.

Data from 500 particles from each of bins 1 to 11 from the retabling of *tb2* were combined into a file. Every tenth case was moved to a testing file and the rest to a training file. As described previously the expert averaged twenty sets of rules and the neural network took the best set of weights from fifty training attempts. (During the training phase neither system could do better than 16% correct individual predictions with the test data.) Data from a sample of the bulk material was then classified by

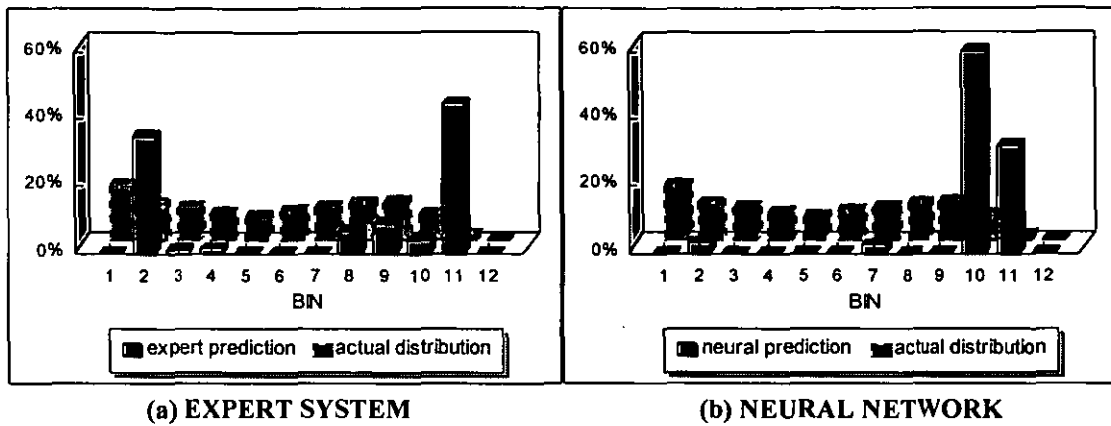


FIGURE 5.5 : Predicting tabling at *tb2* settings

both systems. *Figures 5.5 (a) and (b)* show the predicted distributions, along with the actual distribution. Neither system spread the particles among all the bins. The neural network sent most of them to bins 10 and 11, while the expert preferred 2 and 11.

On retraining the results come out slightly differently, but bin 11 always seems to figure strongly. The expert is inclined to put about 40-60% of the particles into the higher bins (poor shape end of the table) and the rest into one of the lower bins, i.e. 1, 2 or 3. The neural network biases more heavily towards bin 11 or bins 10 and 11 (70-90%) and distributes the rest among a few of the other bins.

Clearly, this performance is not acceptable and the model based on axis ratio and probabilities is superior.

What about adding probabilities to the classifier systems? The expert system was easier to adjust than the neural network so the axis ratio probabilities determined earlier were factored in. The particles in the training and testing sets were assigned axis ratio classes corresponding to the classes for which the probabilities were available. The outcomes, $d(j)$, were multiplied by the appropriate probability. Because $d(j)$ can be a negative value, all $d(j)$'s were shifted by an equal amount to make them all positive and non-zero, before the multiplication. This was done because multiplying a negative number by p where $0 < p < 1$ makes it bigger while a positive number multiplied by p is made smaller, and this could artificially change the decisions.

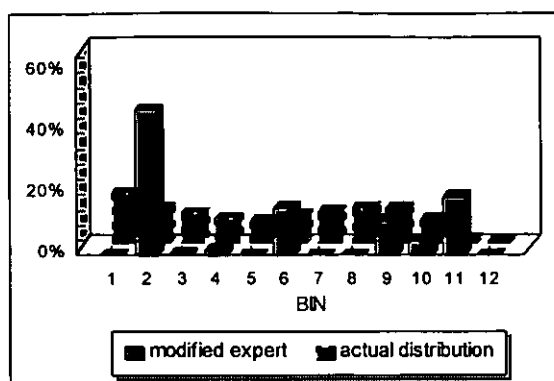


Figure 5.6 : Bulk tabling predicted by expert with inclusion of axis ratio probabilities

The addition of the axis ratio probabilities altered the predictions of the expert system but did not improve them. An example of the predictions for bulk tabling is shown in *Figure 5.6*.

5.3.1 Discussion

Expert systems and neural networks cannot be discounted based only on the work presented. This experimentation was limited in scope. A key requirement for a classification system is a suitable choice of parameters. In Chapter 2 there was a systematic approach to find shape parameters that are likely to describe tabled fractions appropriately and by a sequence of logical steps the most useful parameter was identified to be axis ratio. However, when it comes to choosing a combination of parameters the only way is by trial and error, especially when the optimum number of parameters is not known.

In this case the choice was made by default because at the time of starting to experiment with an expert system it was convenient to use a set of data that had been obtained previously in an unrelated exercise. This set contained four parameters and, since three of the four matched the shortlist of parameters in Chapter 3, it was thought to be as good a set as any. There may be other combinations that would work better as classifiers.

The expert system was written in a basic and simple form. It gave a reasonable performance in discriminating between particles from bins 1 and 9 but could not distinguish between particles from neighbouring bins. Knowing the amount of

overlap between bins within each of the parameters individually, this is probably as much as can be expected from a simple expert system such as this one.

The neural network uses a gradient descent algorithm to find the minimum point in the error space and would be expected to achieve better results than the expert system. Unsuitable choices of network parameters such as number of hidden nodes, learning rate and momentum, can cause paralysis of the network by trapping it in a local minimum or on a plateau. However, with suitable network parameters this algorithm should converge on a solution from any starting point. If there is no convergence after repeated efforts using random starting weights and different values for the network parameters then there is a problem. Either the data cannot be classified as required, or in this case where some amateur programming was involved, there could be a fault in the neural network program.

The program was checked and rechecked and appeared to be working correctly but for more convincing verification the same data was fed into a commercial neural network package. The package is O'inca Design Framework from Intelligent Machines Inc. and contains a back propagation training algorithm. The original training and testing datasets with four parameters for bins 1 and 9 size 50/60 were converted to the format required by O'inca. A network was set up with six hidden nodes, the default learning rate and momentum, and random starting weights. The cases in the training dataset were shuffled and then repeatedly presented to the network. One presentation of the whole set is called an epoch. The default criterion for convergence was an RMS error less than 0.2, where the error is the difference between the actual and expected activations at the output nodes. Training was attempted several times with new random starting weights each time. Convergence was not attained with this criterion but the RMS error always settled at a value of 0.7064. This "settling down" happened after as few as ten epochs.

When the error no longer changes and it is obvious that there will be no further improvement, the training can be interrupted and the network can be tested. The testing dataset contains the desired output activation for each case; 1 for the output node representing the correct class and 0 for all other output nodes. The test data is

fed through the network, the output activations are compared with the desired values and the number of failed cases is reported. The pass/fail criterion can be set as the maximum error or the RMS error. (In this mode the software does not report the actual activations so the winning output node (the one with the highest activation) is not known.) If the maximum allowed error is set to 0.5 then a case will pass only if all output activations are closer to the desired value than to the undesired value in the 0-1 range. On this basis 85% of the cases in the test set passed, which compares favourably with the performance of the neural network program in *Appendix 8*.

The O'inca network was then trained and tested on the data from bins 1 and 2 of *tb2*. The expert had achieved 55% correct predictions and the QuickBASIC neural network had given a result of 61%. Again, O'inca failed to converge and the result for the test set was only 55%.

The commercial neural network behaved in a similar manner to the QuickBASIC neural network, confirming that the problems are associated with the data rather than the programming. The conclusion is that this combination of network parameters and shape parameters will not produce a useful classifier.

Other parameters and/or a different network configuration may give better results. Taking advantage of the ease of use of the O'inca package some other combinations were tried but to no avail. The process of trial and error is very time-consuming when each attempt at training takes several hours. There are so many variables that even experimental design techniques would not produce a quick or easy way to find the optimum settings. Reluctantly, this approach was abandoned.

This completes the exploratory work on shape quantification and modelling. The next chapter summarises and discusses the findings.

6 APPLICATIONS AND DISCUSSION

6.1 SUMMARY

The work is summarised in this section and all findings are emphasised using bold print. The hypotheses proposed in Chapter 1 were:

Hypothesis 1: There exists a shape quantifier that describes meaningfully the table sorting of synthetic diamond sawgrit particles.

Hypothesis 2: The shape quantifier can be used to characterise and model the table sorting of synthetic diamond sawgrit particles.

Many known methods of quantifying shape were introduced in Chapter 2 and then applied to diamond in Chapter 3. Advanced computational methods such as Fourier analysis and fractal analysis were shown to produce information about particle shape but were found to be unsuitable; fractal analysis is not useful for non-rugged particles, while methods employing Fourier series expansion of the particle profile gave too much data and not enough information. An effort to extract a simple parameter from the coefficients resulted in a choice of A_2 , which was then found to correlate very well with a more easily obtained shape factor.

Methods for counting corners were also applied and these produced accurate representations of both computer-generated shapes and images of diamond particles. It is felt that counting corners could be very useful in the diamond industry, if not for modelling tabling then for analysing individual particles in cutting tools. Studying the changing shapes of the protruding particles gives information on the suitability of the diamond type and size for the application, the suitability of the cutting parameters, and the quality of manufacture of the saw blade. The spanning chord method was preferred and it should be possible to develop it later for use in testing saw blades.

Standard shape factors from an image analysis package were also explored. Several shape factors showed a trend in mean value across the bins of a table.

- ♦ **Shape factors calculated by PC-based image analysis software proved to be relevant in describing tabled diamond.**

On the basis of the relationship with strength (as measured by the Friatest) axis ratio was deemed to be the most suitable in terms of relevance for end use of the diamond grit products. This was an important step in the choice of a shape factor because it could not be assumed that the current production table sort is optimum and it would have been wrong to judge the shape factors on tabling only.

- ♦ **Axis ratio was chosen as the shape parameter that proves the first hypothesis to be correct.**
- ♦ **Axis ratio is related to impact strength provided the metal content is taken into account.**

The criteria for obtaining a representative axis ratio distribution for a population were set. It was found that:

- ♦ **With the available equipment individual readings of axis ratio are repeatable to two decimal places when there is reasonable care in focusing the image.**
- ♦ **A representative sample can be obtained by dipping a spoon into the container. Devices like the spinning riffler are not necessary. A slide can be prepared from the contents of the spoon using the procedure described on page 39.**
- ♦ **Measurement of 400 particles is adequate for samples of good, blocky diamonds (from the lower bins). 625 particles is adequate for all but the worst shape fractions.**

With the aim of modelling the tablesort some tabling experiments were carried out and were reported in Chapter 4. Bulk 40/45 material was tabled at two different sets of tabling conditions - *tb1* and *tb2*. This gave two distributions by weight across the bins. Comparing bins 1, 5 and 9 from *tb1* with their counterparts from *tb2* showed them to be significantly different at a 99% confidence level.

- ♦ **Differences between bin contents for these two sets of tabling conditions can be quantified by axis ratio.**

- ♦ **The "open" tabling gave tighter axis ratio distributions within the bins. Biasing the weight distribution towards the lower end of the table gave better discrimination on average axis ratio. (Figure 4.5)**

It was proposed that for a given axis ratio there is a probability associated with each bin as a possible destination. This idea was used as the basis for a model. The probabilities were derived from the proportions of each axis ratio class in each of the bins. Graphs of the probabilities gave some insight into the sorting efficiencies of *tb1* and *tb2*.

- ♦ **The graphs in Figure 4.6 demonstrate the different sorting actions of two sets of tabling conditions.**

The model for *tb2* was tested by first using the probabilities to predict what would happen when the contents of a bin were retabled, and then retabling some of the bins.

- ♦ **The model failed to predict the correct weight distribution for retabling bins 1, 5 and 9 of *tb2*.**

Attempts to adjust the model did not produce any improvement in the predictions. However, it was pointed out that the model has some merits.

- ♦ **The model correctly predicts that the contents of a single bin will spread out to other bins when retabled.**
- ♦ **The reproducibility curve predicted by the model has the correct shape, showing higher reproducibility in the end bins.**

It was felt that one of the shortcomings of the probabilities model was that it relied on only one parameter. In Chapter 5 artificial intelligence was employed to explore the possibility that an appropriate combination of parameters would have less overlap in the bin contents. Four parameters - axis ratio, roundness, length dif and area - were chosen for the initial trials. An expert system and a neural network were programmed in QuickBASIC. When trained and tested on various bin combinations they gave the performances listed overleaf:

from Table 5.5

	Neural Network	Expert System
bins 1 and 9	77%	75%
bins 2 and 8	76%	67%
bins 2 and 5	60%	60%
bins 1 and 2	61%	55%
bins 8 and 9	61%	60%
bins 2, 5 and 8	53%	48%
bins 1, 5 and 9	51%	48%

For this combination of parameters:

- **Neither system was good at distinguishing between neighbouring bins.**
- **Neither system performed well when presented with three bins.**
- **Both systems failed completely to predict the outcome of bulk tabling**

While this thesis was being written up some similar work was published by Hundal et al [105]. They used the Zahn and Roskies Fourier method (page 21 and [45]) to get the first ten harmonics for KCl crystal particles. They then tried two kinds of neural network - competitive and back propagation - to classify the particles into five classes. A competitive network is one that learns without knowledge of the classes and discovers relationships in the data by itself. Hundal et al found that their network clustered the particles into classes but the problem was that the contents of the clusters depended on how long the network was allowed to train. The back propagation network had two hidden layers with 25 neurons in the first and fifteen neurons in the second, and only one output neuron. The activation of the output neuron determined the class. The success rate with five classes was 42%. The fact that other authors also had limited success and acknowledged the difficulties of setting up the correct network proves that this is a promising technique but needs to be developed for each specific application.

Hypothesis 2 was not confirmed but neither can it be rejected. It was demonstrated that table sorting can be characterised using axis ratio measurements. The probabilities model may not have held for new feed distributions but would be valid for bulk. It is still not known whether table sorting can be modelled any better than this. The fact that the probabilities model failed for new feeds is arguably the most

important finding, because it provides new information pertinent to the question of why material from a bin spreads across the table. This will be discussed in section 6.3.

Secondary objectives were to use shape measurements to learn more about tabling and suggest improvements. It has already been shown that axis ratio measurements can help to illustrate differences in bin contents when table settings are changed. The following section gives some more examples of how axis ratio can be used.

6.2 LEARNING FROM AXIS RATIO MEASUREMENTS

6.2.1 Learning Experiment 1

A large batch of 40/45 SDA was being tabled with the purpose of producing nine shape fractions and a reject fraction. During tabling some deliberate interference was introduced to upset the sorting pattern at the high end. On completion of the run an experienced technician viewed the contents of the bins using an optical stereomicroscope and declared that the fractions in bins 6, 7, 8 and 9 were unacceptable by normal sorting standards, but that he could rectify the situation without having to table the whole batch again.

Samples were taken from bins 1 to 9 and axis ratio measurements were made. *Figure 6.1* is a cumulative-percentage-under graph.

The technician recombined the contents of bins 6 to 9 and tabled them such that the particles spread out into all ten bins. He then combined the contents, based on visual assessment, into five fractions - 6a, 7a, 8a, 9a and reject - to match the way bins 6 to 10 should have looked the first time. This is a skilled operation and relies entirely on the experience of the technician. Can his efforts be quantified?

Axis ratio measurements were made on these new fractions and the cumulative graph was replotted, substituting 6a to 9a for 6 to 9. The result is shown in *Figure 6.2*. The improvement is clear. The bin 9 distribution has moved to the right, showing that it contains less reject material than before, and there is a more even spacing of the other

distributions. T-tests were used to test for significant differences in mean axis ratio at a 95% confidence level. In the first tabling (*Figure 6.1*) bins 5 and 6 were not significantly different, neither were bins 7 and 8. After the second tabling (*Figure 6.2*), fractions 6a to 9a were all significantly different from their neighbours.

The purpose of this exercise was not to test the technician, but to test the sensitivity of axis ratio to the subtleties of diamond processing. Tabling is an inexact science but

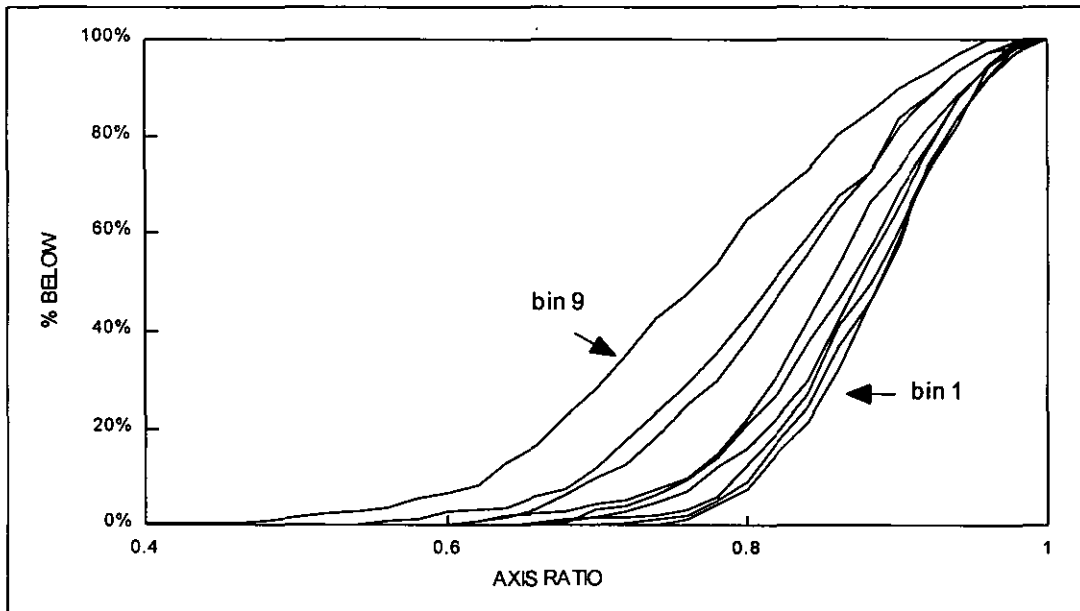


Figure 6.1 : Cumulative axis ratio distributions for bulk tabling with deliberate interference

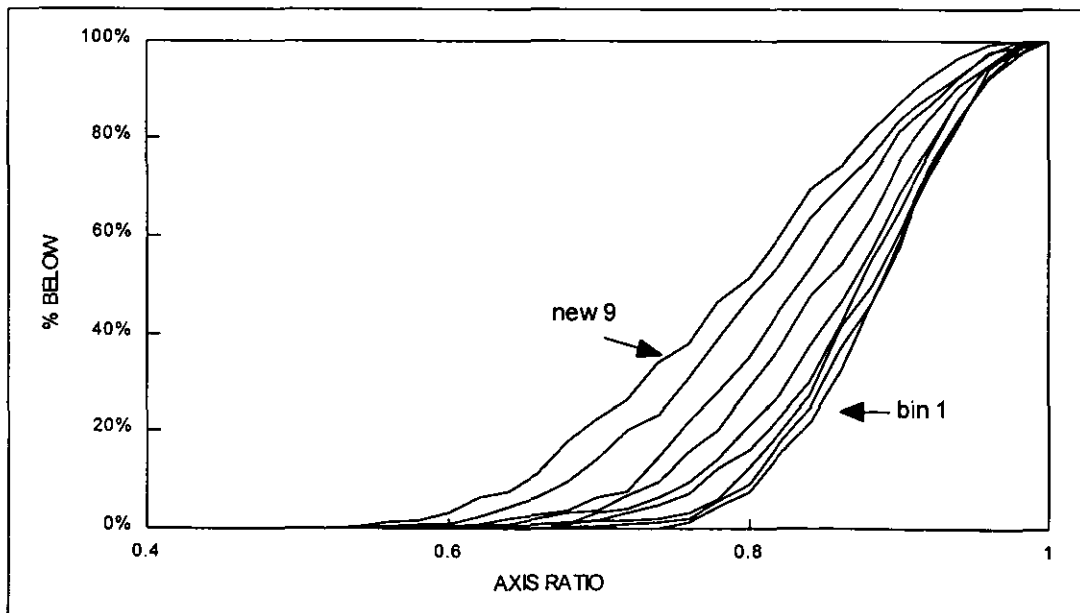


Figure 6.2 : Cumulative axis ratio distributions after retabbling bins 6 to 9

the technicians know how to tweak the system to get the desired results every time. Now, at last, there is a non-subjective way to appreciate their skills.

6.2.2 Learning Experiment 2

Samples of grit with low magnetic impurity and grit with high magnetic impurity were obtained from the contents of bins 1 and 9 from a standard bulk tabling of SDA 40/45. Axis ratio measurements were made on these fractions, which will be called *low mag* and *high mag* respectively. Cumulative distributions are shown in *Figure 6.3*, along with those of the bins from which the fractions came. The shape distribution in the bin 1 fractions is consistent and does not appear to be related to metal content. However, the axis ratios in the *high mag* bin 9 fraction are slightly lower in general than those of the original bin 9. This shows that there is some relationship between shape and metal content at the poor shape end of the SDA range.

This helps to emphasise the point that individual particle strength as measured by the Friatest is dependent on both shape and metal content. The more magnetic fraction from bin 1 would have a lower Friatest result than the less magnetic fraction from the same bin, but there is no difference in shape. In bin 9 a lower Friatest result for the more magnetic fraction would be attributed to both higher metal content and lower axis ratio.

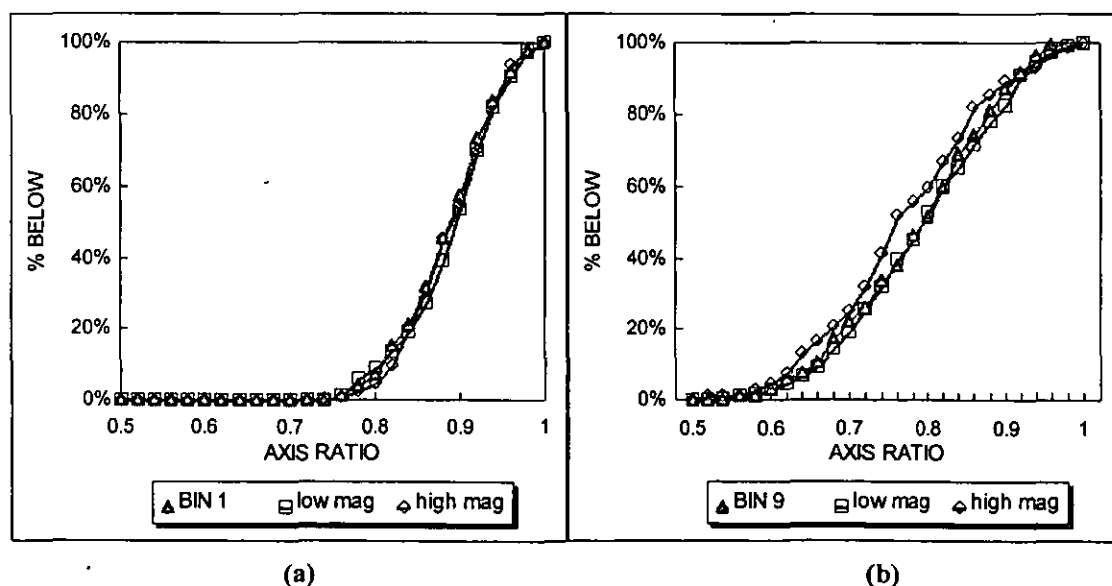


Figure 6.3 : Culmulative axis ratios for magnetic fractions of (a) bin 1 and (b) bin 9

6.3 DISCUSSION

6.3.1 Past

De Beers have been processing synthetic diamonds in Shannon for thirty-five years and possess an understanding of shape sorting that comes with experience. Development of the process has tended to focus on improving the operation of the table itself, by better electronic control for example. Over the years this has helped to improve the consistency of the sort, reducing the need for retabbling. Millions of carats are sorted every month. Within the current specifications it is a trivial matter to achieve the required result from a table.

The problems arise when there is a need to bring about a change in the output. This occurs every now and then when the market demands an addition to the product line, or when the bulk material changes because of improved control during synthesis. The way to cope with such situations is to find new tabling conditions by trial and error, using visual inspection and Friatests to judge the outcome. This can take some time but, eventually, a scheme for obtaining a set of shape fractions is agreed and production carries on. There is never any confirmation that this is the optimum solution and there is always a slight suspicion that there may be a better way - that the same results could be achieved with less bins, or that changing the table settings completely might give a sharper sort. Reluctant to move away from what is adequate, the developers tweak the process rather than attempt radical change.

The stumbling block has been the lack of a shape quantifier. Before image analysis became easily available, efforts to put numbers on the shapes of individual particles concentrated on the diamond morphology using the 0 to 8 system (shown in *Figure 2.1*). Bulk shape measurements were also tried and there were attempts to characterise tabled diamond by subjecting the bin contents to other shape sorting methods like sieving on slotted screens [106]. Then image analysis opened up new possibilities by providing the means of obtaining non-subjective shape measurements.

It was quickly realised that shape would first have to be defined.

6.3.2 Present

The objective of finding a useful definition of shape has been achieved with axis ratio, and the use of this parameter to quantify bin contents in various tabling situations has given some new insights into the table sorting operation. Section 6.2 demonstrated how axis ratio measurements can be used to learn more about tabling. The shape measurements give quantitative confirmation of current understanding and lend credence to theories derived by observation. More examples are given in *Table 6.1*:

Table 6.1 : Examples of observations that have been quantified

<i>Known from Observation</i>	<i>Demonstrated Quantitatively</i>
The difference in shape between neighbouring bins is much greater at the upper end (poor shape end) of the table	In <i>Figure 3.6</i> the graphs are steeper at the upper end <i>Table 5.5</i> shows that the expert system gave a higher success rate with bins 8 and 9 than with bins 1 and 2 (although the neural network did not)
If tabling conditions are altered to give a different weight distribution across the bins then the shape mix in each bin must change	Bins 1, 5 and 9 from two different tablings are compared in <i>Figure 4.4</i> . T-tests proved the means to be significantly different with 99% confidence
Although a bulk shape progression can be seen in the bins after tabling, every bin contains individual particles that look like they should be in another bin	The curves in <i>Figure 4.6</i> show how particles of certain axis ratios are distributed throughout the bins

Some of the diamond tabling mysteries were mentioned in Chapter 1. These can now be discussed in light of the new findings.

QUESTION 1: Why do the contents of a bin, when retabled without changing any settings, spread to other bins as well as returning to the bin from which they came?

Given that tabling conditions have not changed and the shapes of the particles have not changed, the only variables that can cause an individual particle to take a different

route across the table are the interference from its neighbours and the randomness associated with the orientation of the particle each time it hits the surface. The number of possible orientations is related to the shape of the particle. In Chapter 4 the proportions of the particles of a given shape (where shape is defined as axis ratio) ending up in each bin were estimated. This gave an indication of the most likely path for any one particle. It was still impossible to predict the destination of a single particle but when the probabilities were applied in a statistical manner to a set of particles the bulk result could be predicted. The flaw in this approach was that this element of randomness could not be isolated from the particle to particle interference. The predictions were not accurate, probably due to the fact that the interference from other particles was different when the feed material had a narrower shape range.

Some work on single particle tabling was carried out in the past [107]. It showed that when a blocky crystal is tabled on its own repeatedly, it either returns to the same bin every time or ends up in one of two neighbouring bins. However, it cannot be concluded that interference is the sole cause of inconsistency of destination, because the scope of the experiment was very limited. The vibration and angles of the table were set so that the particles had a long residence time on the deck. The particles were hand-picked and were regular in shape, reducing the effect of orientation.

The answer to the question has to be that there is a contribution from both the shape-related randomness and the particle to particle interference. The latter changes when the feed material is the contents of one bin rather than the bulk. The reason the model overestimated the spread of the particles was that it was assuming greater interference.

QUESTION 2: Why is the weight distribution repeatable?

If the same feed is tabled at the same conditions then the only factor to be considered is the shape-related randomness. In statistical terms the overall result in terms of the shape mix in each bin will be the same, even though many of the individual particles will have ended up in different bins.

QUESTION 3: Why is there so much overlap between the bins?

The operation is the sorting of diamond from diamond. The shape range is quite narrow to start with and usually ten to twelve shape fractions are required. If the purpose was to separate diamond from another abrasive then the sort would be much more efficient. *Figure 6.4* shows the cumulative axis ratio distribution for a sample of silicon carbide abrasive compared with those of bin 1 and bin 9 diamond shape fractions. The fact that there are seven other fractions between bin 1 and bin 9 puts the overlap problem in perspective. There would also be less overlap if fewer shape fractions were needed. If the only requirement were to separate the worst shapes from the rest of the bulk, then the table could be set to achieve a sharp separation with very little overlap. The problem of overlap is not unique to tabling. Batch sieving also gives overlap, as demonstrated by Ludwick and Henderson [16].

QUESTION 4: Can the overlap be reduced?

There would be less overlap if tabling was carried out at much lower feedrates to

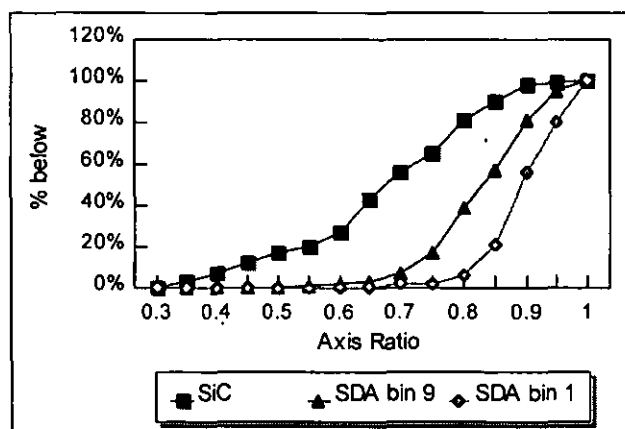


Figure 6.4 : Cumulative axis ratios of diamond compared with SiC

reduce the effect of the particle-particle interference. However, this is not practical in a commercial production operation. Another non-practical suggestion is to greatly enlarge the table, since increasing the residence time of the particles on the deck would reduce randomness. Otherwise the extent of overlap will depend on the sort required. It was shown in *Figure 4.5* that *tb2* produced sharper fractions than *tb1*.

However, this is not much help if the weight distribution of *tbl* is preferred. This leads on to the question about the optimum sort.

QUESTION 5: Is the "even" sort the optimum sort?

The tools for assessing a sort are now in place but a definition of exactly what is required from bulk table sorting is needed before this question can be addressed.

6.3.3 Future

It is acknowledged that it is highly unlikely that a single two-dimensional shape parameter will ever provide all that is required in shape analysis of diamond. If multiple factors are required then artificial intelligence may be the way to go. The exploration of expert systems and neural networks in Chapter 5 was only a brief test of the principles. As well as trying shape factors as inputs, Fourier coefficients could be used, as demonstrated by Hundal et al [105]. It takes a little more effort to obtain the coefficients but the routine could be automated to make it faster and less tedious. Further work in this area would be worthwhile. Commercial software and some time dedicated to trying many variations are all that are needed.

Otherwise, if a single parameter is to be adopted as the definitive shape measurement the preceding chapters make a strong case for axis ratio. This parameter is easy to measure and will be very useful in the characterisation of new and existing diamond sawgrit products. The analysis should be extended to sizes other than 40/45.

The last question in the previous section is the one to be answered if any real progress in revolutionising diamond shape sorting is to be made. Currently, products are specified by strength. By the nature of the Friatest the measured strength is a bulk property and is probably affected by the width of the shape distribution. A specification on the mean and standard deviation of axis ratio would help to define the shape of a product independently of processing. Once the preferred shape mix for a specified strength and desired appearance is established, there is the possibility of finding a new set of tabling conditions to give this mix. This should be the main objective of any future work.

One of the hindrances in the tabling experiments was the fact that a table could not be set precisely. Another was that individual particles could not be monitored. Some engineering developments are required to allow exact and reproducible settings and it would be a real breakthrough if a method of tagging individual particles could be found. These factors combined would greatly help future researchers with shape-sorting of any material, not just diamond. They would enable an assessment of the steady state conditions, and the effects of reduced weight on the table during starting and ending of feed from the hopper. The particle-particle interference on the table could be investigated further and should be incorporated into any future model of tabling.

6.4 CONCLUSION

Two hypotheses were proposed. The first was shown to be correct. Axis ratio was identified as a very useful shape factor and it is hoped that it will become a recognised parameter in diamond characterisation. It provides a means of defining shape independently of processing and this is a significant step forward for the industrial diamond industry.

The second hypothesis was not so straightforward. It was shown that axis ratio can be used to characterise the results of table sorting. The behaviour of diamond on a shape sorting table was analysed. This gave quantitative confirmation of accepted but unproved theories and gave new insight into some of the tabling anomalies. It was also shown that a model based on probabilities associated with axis ratios worked in certain cases. The fact that the model did not hold in other cases was informative and elements such as particle-particle interference and randomness due to orientation were discussed with new authority.

The primary objective of producing a model for the tabling of synthetic diamond was partially achieved - the proposed model was valid in limited situations, and the reasons for failure of the model in other situations were given. Secondary objectives of learning more about shape in general, about diamond shape, and about tabling of diamond were achieved.

REFERENCES

1. Luerkens D. W., Beddow J. K., Vetter A. F., Structure and Morphology - The Science of Form Applied to Particle Characterisation, *Pow. Tech.*, 50 (1987) pp93-101
2. Lloyd P. J., The Characterisation of Particle Shape, Particle Size Analysis, John Wiley & Sons, 1988
3. Hausner Henry H., Characterisation of the Powder Particle Shape, Symp. Part. Size Anal., LUT, Soc. Anal. Chem., London, 1966, pp20-29
4. Flook Alan G., A Comparison of Quantitative Methods of Shape Characterisation, *Acta Stereol.*, 3/2 (1984) pp159-164
5. Wentworth Chester K., The Shapes of Rock Particles : A Discussion, *J. Geol.*, 41 (1933) pp306-309
6. Meloy T. P., Mani B. P., Clark N. N., Particle Shape Analysis and Separation Techniques: A Critical Review, *J. Pow. Bulk Solids Tech.*, 10 (1) 1986) pp15-20
7. Endoh S., Sorting of Particles by Inclined Vibrating Plate. I. Analysis of the Motion of Particles on an Inclined Vibrating Plate, *Pow. Tech.*, 50 (1987) pp103-109
8. Ohya H., Endoh S., Yamamoto M., Iwata H., Analysis of Particle Motion Regarding Shape Separation Using an Inclined Conveyor, *Pow. Tech.*, 77 (1993) pp55-59
9. Meloy T. P., Pitchumani B., Clark N., Residence Time Distribution of Particles on Sieves Shape Separation, *Ind. Chem. Eng.*, 29 (1) (1987) pp43-49
10. Clark N., Durney T. E., Meloy T. P., Recent Advances in Particle Shape Characterisation, *J. Pow. Bulk Solids Tech.*, 8 (1984) pp21-24
11. Meloy T. P., Clark N., Durney T. E., Pitchumani B., Measuring the Particle Shape Mix in a Powder with the Sieve Cascadograph, *Chem. Eng. Sci.*, 40 (7) (1985) pp1077-1084
12. Meloy Thomas, Williams Mark, Controlling Particle Sizing with Two-Dimensional Networks, 5. European Symposium Particle Characterisation, Nuremberg, 1992, Pre-prints pp561-571
13. Meloy T. P., Williams, M. C., Rulke A., Vibrating Tables - A Two-Dimensional Network Analysis, *Pow. Tech.*, 70 (1992) pp51-56
14. Nakajima Y., Whiten W. J., White M. E., Method for Measurement of Particle Shape Distribution by Sieves, *Trans. Inst. Min. Metall.*, 87 (1978) ppC194-203
15. Whiteman M., Ridgeway K., A Comparison Between Two Methods of Shape Sorting Particles, *Pow. Tech.*, 56 (1988) pp83-94
16. Ludwick J. C., Henderson P., Particle Shape and Inference of Size from Sieving, *Sedimentology*, 11 (1968) pp197-235
17. Ludwick John C., Particle Shape: Classification of Thickness Using Slotted Screens, *J. Sed. Petrol.*, 41 (1) (1971) pp19-29
18. Sano S., Nikaidoh M., Proc. 2nd World Congress Part. Tech., Kyoto, Sept. 19-22, 1990, pp214
19. Sano S., Yashima S., Proc. Spring Meet. Soc. Pow. Tech. Jpn., Osaka, May 26-27, 1987, pp5
20. Endoh S., Iwata H., Proc. 24th Autumn Meet. Soc. Chem. Eng. Jpn., Nagoya, Oct 16-18, 1991, pp404
21. Furuuchi M., Gotoh K., Shape Separation of Particles, *Pow. Tech.*, 73 (1992) pp1-9
22. Wadell Hakon, Volume, Shape, and Roundness of Rock Particles, *J. Geol.*, 40 (1932) pp443-451
23. Wadell Hakon, Volume, Shape, and Roundness of Quartz Particles, *J. Geol.*, 45 (1935) pp250-280
24. Zingg Th., Beitrag zur Schotteranalyse, *Schweiz Min. u. Pet. Mittl.*, 15 (1935) pp39-140
25. Krumbein W. C., Measurement and Geological Significance of Shape and Roundness of Sedimentary Particles, *J. Sed. Petrol.*, 11 (2) (1941) pp64-72
26. Aschenbrenner Bert C., A New Method of Expressing Particle Sphericity, *J. Sed. Petrol.*, 26 1 (1956) pp15-31
27. Heywood H., Particle Shape Coefficients, *J. Imp. Chem. Eng. Soc.*, 8 (1954) pp25-33
28. Medalia A. I., Dynamic Shape Factors of Particles, *Pow. Tech.*, 4 (1970) pp117-138
29. Burns K. L., Spry A. H., Analysis of the Shape of Deformed Pebbles, *Tectonophysics*, 7 (3) (1969) pp177-196
30. Sneed E. D., Folk R. L., Pebbles in the Lower Colorado River, *J. Geol.*, 66 (1958) pp114

31. Davies R., A Simple Feature-Space Representation of Particle Shape, *Pow. Tech.*, 12 (1975) pp111-124
32. Schwarcz H. P., Shane K. C., Measurement of Particle Shape by Fourier Analysis, *Sedimentology*, 13 (1969) pp213-231
33. Ehrlich Robert, Weinberg Bernhard, An Exact Method for the Characterisation of Grain Shape, *J. Sed. Petrol.*, 40 (1) (1970) pp205-212
34. Meloy T. P., Fast Fourier Transforms Applied to Shape Analysis of Particulate Silhouettes to Obtain Morphological Data, *Pow. Tech.*, 17 (1977) pp27-35.
35. Gotoh Keishi, Suzuki Akira, Meloy T. P., Shape Characterisation of Two-Dimensional Forms By Fraction of Ellipse and Diamond, *Part. Sci. Tech.*, 1 (1985) pp67-75
36. Beddow J. K., Philip G. C., Vetter A. F., Nasta M. D., Relating Some Particle Profile Characteristics to the Profile Fourier Co-efficients, *Pow. Tech.*, 18 (1977) pp19-25
37. Beddow John Keith, Vetter Arthur F., Luerkens David, Collins Steve, Morphological Analysis of Fine Particles, *Proc. 2nd Eur. Symp. Part. Char.*, Nuremberg, 1979, pp565-581
38. Luerkens D. W., Beddow, J. K., Vetter A. F., Morphological Fourier Descriptors, *Pow. Tech.*, 31 (1982) pp209-215
39. Swanson P.A., Vetter A. F., The Measurement of Abrasive Particle Shape and the Effect on Wear, *ASLE Translations*, 28 (2) (1984) pp225-230.
40. Vetter A. F., Swanson P. A., Particle Morphology Applied to Characterising Abrasive Materials, *Part. Sci. Tech.*, 1 (1983) pp127-138
41. Rajpal Samir, Beddow J. K., Hua Louise, Chang C. R., On the Effects of Particle Morphology on Dry Separation of Solids, *Intl. Conf. on Pow. and Bulk Solids Proc.*, Chicago, IL, 1982, pp37-46
42. Gotoh K., Finney J. L., Representation of Size and Shape of a Single Particle, *Pow. Tech.*, 12 (1975) pp125-130
43. Luerkens D. W., Mathematical Representations of Irregularly Shaped Particles in Two and Three Dimensions, 1. *World Congress Particle Technology*, Part 1, Nuremberg, 1986, Pre-prints p63-70
44. Luerkens D. W., Fine Particle Representations, *Pow. Bulk Solids Conf./Ex.* 1989, pp615-624
45. Zahn C. T., Roskies R. Z., Fourier Descriptors for Plane Closed Curves, *IEEE Trans. Comp.*, C-21 (3) (1972) pp269-281
46. Fong S. T., Beddow J. K., Vetter A. F., A Refined Method of Particle Shape Representation, *Pow. Tech.*, 22 (1979) pp17-21
47. Luerkens D. W., Beddow, J. K., Vetter A.F., A Generalised Method of Morphological Analysis (the (R,S) Method), *Pow. Tech.*, 31 (1982) pp217-220
48. Shibata Toshiharu, Yamaguchi Kenji, Shift x,y Co-ordinate Detection of Line Figures and the Extraction of Particle Shape Information, *Pow. Tech.*, 81 (1994) pp111-115
49. Meloy T. P., A Hypothesis for Morphological Characterisation of Particle Shape and Physiochemical Properties, *Pow. Tech.*, 16 (1977) pp233-253.
50. Meloy Thomas P., Particulate Shape Characterisation, *J. Pow. Bulk Solids Tech.*, 2 (2) (1978) pp13-23
51. Mandelbrot B. P., *Fractals: Form, Chance and Dimension*, W. H. Freeman & Co., San Francisco, 1977
52. Kaye B. H., Specification of the Ruggedness and/or Texture of a Fineparticle Profile by its Fractal Dimension, *Pow. Tech.*, 21 (1978) pp1-16
53. Kaye B. H., Trottier R. A., Clark G. G., Characterising the Fractal Structure of Fineparticle Profiles Using the Concepts of Geometrical Probability, 5. *European Symposium Particle Characterisation*, Nuremberg, 1992, pp59-70.
54. Schwarz H., Exner H. E., The Implementation of the Concept of Fractal Dimension on a Semi-Automatic Image Analyser, *Pow. Tech.*, 27 (1980) pp207-213.
55. Clark N. N., Three Techniques for Implementing Digital Fractal Analysis of Particle Shape, *Pow. Tech.*, 46 (1986) pp45-52.
56. Normand M. D., Peleg M., Determination of the Fractal Dimension of a Particle Silhouette Using Image Processing Techniques, *Pow. Tech.*, 45 (1986) pp271-275.
57. Kaye Brian H., Multifractal Description of a Rugged Fineparticle Profile, *Part. Charact.*, 1 (1984) pp14-21
58. Flook Alan G., Fractal Dimensions : Their Evaluation and Their Significance in Stereological Measurements, *Acta Stereol.*, (1982) pp79-87

59. Flook A. G., The Use of Dilation Logic on the Quantimet to Achieve Fractal Dimension Characterisation of Textured and Structured Profiles, *Pow. Tech.*, 21 (1978) pp295-298.
60. Adler J., Hancock D., Advantages of Using a Distance Transform Function in the Measurement of Fractal Dimensions by the Dilation Method, *Pow. Tech.* 78 (1994) pp191-196
61. Graf J. C., The Importance of Resolution Limits to the Interpretation of Fractal Description of Fine Particles, *Pow. Tech.*, 67 (1991) pp83-85
62. Wright K., Karlsson B., Fractal Analysis and Stereological Evaluation of Microstructures, *J. Micros.*, 129 (2) (1983) pp185-200
63. Orford J. D., Whalley W. B., The Use of Fractal Dimension to Quantify the Morphology of Irregular-Shaped Particles, *Sedimentology*, 30 (1983) pp655-668
64. Rigaut J. P., An Empirical Formulation Relating Boundary Lengths to Resolution in Specimens Showing "Non-Ideally Fractal" Dimensions, *J. Micros.*, 133(1) (1984) pp41-54
65. Allen Martin, Brown Gareth J., Miles Nick J., Measurement of Boundary Fractal Dimensions: Review of Current Techniques, *Pow. Tech.*, 84 (1995) pp1-14
66. Clark N. N., A New Scheme for Particle Shape Characterisation Based on Fractal Harmonics and Fractal Dimensions, *Pow. Tech.*, 51 (1987) pp243-249
67. Reilly S., Clark N. N., Computer Based General Shape Description with Polygonal Harmonics and a Roughness Index, *Proc. Instrn. Mechn. Engrs.*, 205(E) (1991) pp103-111.
68. Clark N. N., Gabriele P., Shuker S., Drag Co-efficient of Irregular Particles in Newton's Settling Regime, *Pow. Tech.*, 59 (1989) pp69-72
69. Young B. D., Bryson A. W., Van Vliet B. M., An Evaluation of the Technique of Polygonal Harmonics for the Characterisation of Particle Shape, *Pow. Tech.*, 63 (1990) pp157-168.
70. Maeder A. J., Clark N. N., Harmonic Endurance - A New Shape Descriptor Derived From Polygonal Harmonics, *Pow. Tech.*, 68 (1991) pp137-143.
71. Piper D. J. W., The Use of the D-Mac Pencil Follower in Routine Determination of Sedimentary Parameters, in J. L. Cutbill (ed.) *Data Processing in Biology and Geology*, Academic Press, London, 1971, pp97-103
72. Pickett James, Clark Nigel, Shuker Stephanie, A Re-examination of Piper's Shape Analysis Technique, *Part. Part. Syst. Char.*, 8 (1991) pp110-115
73. Clark N. N., Meloy T. P., Delta Analysis of Particle Surface Fine Structure, *J. Pow. Bulk Solids Tech.*, 9 (1) (1985) pp1-8
74. Kaye B. H., Clark G. G., Liu Y., Characterising the Structure of Abrasive Fineparticles, *Part. Part. Syst. Charact.*, 9 (1991) pp1-8
75. Beresford R. H., Lloyd P. J., Particle Shape, *Granulometrie*, 5, Dresden, (1987)
76. Kaye B. H., The Use of Feret's Diameter Signature Waveform as a Shape Characterisation Parameter in Fineparticle Science, *J. Pow. Bulk Solids Tech.*, 2 (2) (1978) pp24-33
77. Kaye B. H., Naylor A. G., An Optical Information Procedure for Characterising the Shape of Fineparticle Images, *J. Pattern Recog. Soc.*, May, 1972
78. Clark J. M., Reid K., Kaye P. H., Particle Shape Characterisation by Light Scattering and by Image Analysis, *The Aerosol Soc. Part. Shape Workshop*, Loughborough University of Technology, 1991
79. Staniforth J. N., Rees J. E., Shape Classification of Re-entrant Particles I: The Shape Factor, *Pow. Tech.*, 28 (1981) pp3-8
80. Staniforth J. N., Rees J. E., Shape Classification of Re-entrant Particles II: Description of Re-entrant and Non-Reentrant Particle Shapes, *Pow. Tech.*, 28 (1981) pp9-16
81. Meloy T. P., Geometry for Characterising Fractured Particle Shape, *Pow. Tech.*, 55 (1988) pp285-291
82. Meloy T. P., A Method for Quantify Crushed Particle Shape, 4. *Eur. Symp. Part. Char.*, Nuremberg, 1989, Pre-prints pp441-451
83. Bandemer Hans, Kraut Andre, On a Fuzzy-Theory-Based Computer-Aided Particle Shape Description, *Fuzzy Sets and Systems*, 27 (1988) pp105-113
84. Heidenreich E., Muller G., New Aspects in Particle Shape Analysis With Respect to its Technological Relevance, 1. *World Congress Part. Tech.*, Nuremberg, 1986, Pre-prints pp81-91
85. Bonifazi G., Massacci P., Patrizi G., Hierarchical Properties of Particle Shape for the Recognition of Powdered Materials, 4. *European Symposium Particle Characterisation*, Nuremberg, 1989, Pre-prints pp425-440

86. Bonifazi G., Patrizi G., Image Characteristics and the Recognisable Properties of Mineral Particles, 5. European Symposium Particle Characterisation, Nuremberg, 1992, Pre-prints pp45-58
87. Custers J. F. H., Raal F. A., A New Method of Determining the Average Shape of Diamond and Other Particles, *Ind. Dia. Rev.*, 19 (1959) pp72
88. Dyer H. B., Wedepohl P. T., Determination of the Shape of Diamond Grit Particles, IDA Conference, Paris, 1962
89. Bakon A., Szymanski A., Morphological Qualitative Classification of Synthetic Diamond Microcrystals, *Mineralogica Polonica*, 13 (2) (1982) pp61-68
90. Woods G. S., Lang A. R., Cathodoluminescence, Optical Absorption and X-Ray Topographic Studies of Synthetic Diamond, *J. Crystal Growth*, 28 (1975) pp215-226
91. Davies G., Cathodoluminescence of Diamond : A Short Review, *Diamond Research*, 1975 pp13-17
92. Pipkin N. J., An SEM Study of Synthetic Diamond Morphology, *Ind. Dia. Rev.*, Feb. 1980 pp58-62
93. Deakins Martin, Hawkins Alicia, New Diamond Technologies Changing the Shape of the Stone Industry, *Dimensional Stone Magazine*, Sept 1993 pp17-21
94. Jackson W. E., Hayden S. C., Quantifiable Diamond Characterisation Techniques : Shape and Compressive Fracture Strength, *Finer Points*, 5 (3) pp21-29
95. U.S. patent nos. 3 649 268, 4 282 308
96. Allen T., Sieve Calibration Using Tacky Dots, *Pow. Tech.*, 79 (1994) pp61-68
97. British Standard BS 3406 1988 Part 2
98. D'Arcy O., De Beers Internal Report, 1991
99. Naylor Chris, *Build Your Own Expert System*, Sigma Technical Press, Cheshire, 1983
100. Hecht-Nielsen Robert, *Neurocomputing*, Addison-Wesley Publishing Company Inc., 1990
101. Eberhart Russell C. and Dobbins Roy W. eds., *Neural Network PC Tools A Practical Guide*, Academic Press Inc., San Diego, 1990
102. Fu LiMin, *Neural Networks in Computer Intelligence*, McGraw Hill Series in Computer Science, 1994
103. Marren Alianna, Harston Craig, Pap Robert, *Handbook of Neural Computing Applications*, Academic Press, San Diego, 1990
104. Rumelhart David E., McClelland James L. and the PDP Research Group, *Parallel Distributed Processing, Explorations in the Microstructure of Cognition, Volume 1 : Foundations*, MIT Press, Cambridge, MA, 1986
105. Hundal H. S., Rohani S., Wood H. C., Pons M. N., Particle Shape Characterisation Using Image Analysis and Neural Networks, *Pow. Tech.*, 91 (1997) pp217-227
106. Vucinovich C., De Beers Internal Report, 1992
107. Burke Hugo R. G., De Beers Internal Report, 1992

APPENDIX 1

'EDGE_FINDER

'this program reads a grey-level file shape\$.gry and writes the edge
'co-ordinates to a file shape\$.edg

DECLARE FUNCTION edge! (i!, j!)

FOR w = 1 TO 24

shape\$ = "bin2_" + LTRIM\$(STR\$(w))

file\$ = shape\$ + ".gry"

OPEN file\$ FOR INPUT AS #1

' file contains greylevel values for rectangular ROI

' format n.g1.g2.g3.....gn where n is no. of points per line

DIM SHARED P(100, 100)

'P(x,y) takes the value 1 if pixel x,y is

'particle, 0 for background, and 2 for edge

'read in the file, assign xy co-ordinates and identify particle pixels

'count=no. of particle pixels

y = 0: count = 0: sumx = 0: sumy = 0

DO

INPUT #1, n

y = y + 1

FOR x = 1 TO n

INPUT #1, G

IF G < 20 THEN

P(x, y) = 1

sumx = sumx + x

sumy = sumy + y

count = count + 1

ymax = y

ELSE

P(x, y) = 0

END IF

NEXT x

LOOP UNTIL EOF(1)

'find centroid

xcen = sumx / count: ycen = sumy / count

PRINT "particle area ": count; " pixels"

PRINT "centroid ": xcen, ycen

CLOSE #1

' edge-following algorithm

' sets P of edges to 2

' writes co-ordinates of edge points to a file

file\$ = shape\$ + ".edg"

OPEN file\$ FOR OUTPUT AS #2

e = 0 'e counts edge points

x = 1: y = 1

' look along top line for first edge point

100 IF P(x, y) = 0 THEN

```

    x = x + 1
    IF x > 120 THEN y = y + 1: x = 1
    GOTO 100
  END IF

'when an edge pixel is found, write its co-ordinates to the file
found: WRITE #2, x - xcen, -y + ycen
      P(x, y) = 2: e = e + 1
      endflag = 0

'search clockwise for next edge pixel, starting at 12 o'clock
try:  x = x + 1
      IF edge(x, y) = 1 THEN GOTO found
      y = y + 1
      IF edge(x, y) = 1 THEN GOTO found
      x = x - 1
      IF edge(x, y) = 1 THEN GOTO found
      x = x - 1
      IF edge(x, y) = 1 THEN GOTO found
      y = y - 1
      IF edge(x, y) = 1 THEN GOTO found
      y = y - 1
      IF edge(x, y) = 1 THEN GOTO found
      x = x + 1
      IF edge(x, y) = 1 THEN GOTO found
      x = x + 1
      IF edge(x, y) = 1 THEN GOTO found

endflag = endflag + 1
'if didn't find another edge pixel move right and have one more try
'if fail on second try then assume back at the beginning
IF endflag < 2 THEN GOTO try

CLOSE #2
PRINT w, e, " edge points"

NEXT w
END

FUNCTION edge (i, j)
'this examines eight neighbouring pixels and identifies (i,j) as an
'edge pixel if at least one off-diagonal pixel has P=0

flag = 0
IF P(i, j) = 1 THEN
FOR m = i - 1 TO i + 1
  FOR n = j - 1 TO j + 1
    IF P(m, n) = 0 THEN
      IF m = i OR n = j THEN flag = flag + 1
    END IF
  NEXT n
NEXT m
END IF

IF flag > 0 THEN edge = 1 ELSE edge = 0

END FUNCTION

```

APPENDIX 2

'CALCULATION OF FOURIER COEFFICIENTS

'this program reads a file of cartesian co-ordinates, converts them to polar
'coordinates, calculates the Fourier coefficients and LBV factors, and regenerates
'the profile to check the error

```

FOR w = 1 TO 24
shape$ = "bin2_" + LTRIM$(STR$(w))
file$ = shape$ + ".edg"
OPEN file$ FOR INPUT AS #1

'find number of edge points
e = 0
DO
INPUT #1, x, y
e = e + 1
LOOP UNTIL EOF(1)
CLOSE #1

PRINT : PRINT "converting edge points to polar co-ordinates..."
' define arrays for polar co-ordinates
REDIM r(e), theta(e)
OPEN file$ FOR INPUT AS #1
pi = 3.14159265#
i = 0: sumr = 0
'convert x,y to r,theta
DO
INPUT #1, x, y
i = i + 1
r(i) = SQR(x ^ 2 + y ^ 2)
sumr = sumr + r(i)
IF x = 0 AND y > 0 THEN theta(i) = pi / 2
IF x = 0 AND y < 0 THEN theta(i) = 3 * pi / 2
IF x > 0 AND y >= 0 THEN theta(i) = ATN(y / x)
IF x > 0 AND y < 0 THEN theta(i) = 2 * pi + ATN(y / x)
IF x < 0 THEN theta(i) = pi + ATN(y / x)
LOOP UNTIL EOF(1)
CLOSE #1

' normalise the radii
FOR i = 1 TO e: r(i) = r(i) * e / sumr: NEXT i

' sort by theta : standard compare and swap routine
PRINT : PRINT "sorting..."
sort: flag = 0
FOR i = 2 TO e
IF theta(i) < theta(i - 1) THEN
t = theta(i): theta(i) = theta(i - 1): theta(i - 1) = t
r = r(i): r(i) = r(i - 1): r(i - 1) = r
flag = 1
END IF
NEXT i
IF flag = 1 THEN GOTO sort

```

```

PRINT : PRINT "estimating Fourier co-efficients..."
'           using equations from paper by Ehrlich and Weinberg

n1 = 50 'n1=number of coefficients
REDIM fa(n1), fb(n1), a(n1) 'arrays for Fourier coefficients

FOR i = 1 TO e
th1 = theta(i): r1 = r(i)
IF i = e THEN
'since last point is followed by first point to close the loop
th2 = theta(1) + 2 * pi: r2 = r(1)
ELSE
th2 = theta(i + 1): r2 = r(i + 1)
END IF
fa(0) = fa(0) + (r2 + r1) * (th2 - th1)
FOR j = 1 TO n1
fa(j) = fa(j) + (r2 - r1) * (COS(j * th2) - COS(j * th1)) / (th2 - th1) / j ^ 2 +
(r2 * SIN(j * th2) - r1 * SIN(j * th1)) / j
fb(j) = fb(j) + (r2 - r1) * (SIN(j * th2) - SIN(j * th1)) / (th2 - th1) / j ^ 2 -
(r2 * COS(j * th2) - r1 * COS(j * th1)) / j
NEXT j
NEXT i

file$ = shape$ + ".fab"
OPEN file$ FOR OUTPUT AS #2
fa(0) = fa(0) / 4 / pi
WRITE #2, fa(0)
sumA = 0
FOR j = 1 TO n1
fa(j) = fa(j) / pi: fb(j) = fb(j) / pi
'write first ten coefficients to file
IF j < 11 THEN WRITE #2, fa(j), fb(j)

' calculate Luerkens, Beddow, Vetter parameters
a(j) = SQR(fa(j) ^ 2 + fb(j) ^ 2)
sumA = sumA + a(j) ^ 2
NEXT j
Ro = SQR(fa(0) ^ 2 + .5 * sumA)
WRITE #2, Ro
WRITE #2, fa(0) / Ro
FOR j = 1 TO 5
L(j) = a(j) ^ 2 / (2 * Ro ^ 2)
WRITE #2, L(j)
NEXT j
PRINT : PRINT

PRINT : PRINT "re-generating profile..."

sumr = 0
file$ = shape$ + ".prg"
OPEN file$ FOR OUTPUT AS #1
WRITE #1, shape$
REDIM rg(e) 'edge points regenerated from Fourier coefficients
FOR i = 1 TO e
rg(i) = fa(0)
FOR j = 1 TO n1
rg(i) = rg(i) + fa(j) * COS(j * theta(i)) + fb(j) * SIN(j * theta(i))
NEXT j

```

```
sumr = sumr + (r(i) - rg(i)) ^ 2
WRITE #1, r(i), rg(i), theta(i)
NEXT i
PRINT "mean error = "; SQR(sumr / e)
CLOSE

NEXT w
```

APPENDIX 3

' POLYGONAL HARMONICS

```

FOR w = 1 TO 24
w$ = LTRIM$(STR$(w))
shape$ = "t2m1_0" + w$
file$ = shape$ + ".edg"
OPEN file$ FOR INPUT AS #1

'find number of edge points
e = 0
DO
INPUT #1, x, y
e = e + 1
LOOP UNTIL EOF(1)
CLOSE #1

REDIM x(e), y(e)
REDIM SX(100), SY(100)      'arrays for
REDIM H(101)                'array for no. of occurrences of each harmonic

OPEN file$ FOR INPUT AS #1
FOR i = 1 TO e
INPUT #1, x(i), y(i)
NEXT i
x(0) = x(e): y(0) = y(e)
CLOSE #1

'stepping algorithm from paper by Young, Bryson, Van Vliet [69]
'r=required steplength, L=actual distance from previous point to current
' point, N=minimum no. of points to step, T=no. of traverses, p=no. of
' sides on polygon, corr=correction to eliminate first steps before settling,
' har=order of harmonic

r = 9: quitflag = 0

DO
r = r + 1
N = 1: xb = x(1): yb = y(1): p = 0: T = 0
SX(0) = x(1): SY(0) = y(1): flag = 0: corr = 0
DO
L = 0
DO
N = INT(N + (r - L) / SQR(2))
IF N > e THEN N = N - e: T = T + 1      'T counts no. of traverses
L = SQR((xb - x(N)) ^ 2 + (yb - y(N)) ^ 2)
LOOP UNTIL r - L < SQR(2)
WHILE r - L > 0
N = N + 1
IF N > e THEN N = N - e: T = T + 1
IF T = 1 AND p = 0 THEN GOTO quit
L = SQR((xb - x(N)) ^ 2 + (yb - y(N)) ^ 2)
WEND
IF r - L = 0 THEN
xb = x(N): yb = y(N)

```

```

ELSE 'interpolate
  IF x(N) = x(N - 1) THEN
    newy = yb + SQR(r ^ 2 - (x(N) - xb) ^ 2)
    IF ABS((newy - y(N)) + (newy - y(N - 1))) > ABS(y(N) - y(N - 1)) THEN
      newy = yb - SQR(r ^ 2 - (x(N) - xb) ^ 2)
    END IF
    xb = x(N): yb = newy
  ELSE
    m = (y(N) - y(N - 1)) / (x(N) - x(N - 1))
    c = (x(N) * y(N - 1) - x(N - 1) * y(N)) / (x(N) - x(N - 1))
    newx = (xb - m * (c - yb) + SQR((m * (c - yb) - xb) ^ 2 - (1 + m ^ 2) *
(xb ^ 2 + (c - yb) ^ 2 - r ^ 2))) / (1 + m ^ 2)
    IF ABS((newx - x(N)) + (newx - x(N - 1))) > ABS(x(N) - x(N - 1)) THEN
      newx = (xb - m * (c - yb) - SQR((m * (c - yb) - xb) ^ 2 - (1 + m ^ 2) *
(xb ^ 2 + (c - yb) ^ 2 - r ^ 2))) / (1 + m ^ 2)
    END IF
    xb = newx
    yb = m * xb + c
  END IF
END IF
p = p + 1
IF p > 100 THEN flag = 1: GOTO giveup
SX(p) = xb: SY(p) = yb
' check for repetition
FOR i = 0 TO p - 1
  IF ABS(SX(p) - SX(i)) < .01 AND ABS(SY(p) - SY(i)) < .01 THEN
    flag = 1: corr = i: i = p - 1
  END IF
NEXT i
giveup:
LOOP UNTIL flag = 1

IF corr > 0 THEN T = INT(1 + T * (p - corr) / p)
har = p - corr
IF T = 1 THEN H(har) = H(har) + 1
LPRINT r, har, T
quit:
IF T = 1 AND p = 0 THEN quitflag = 1
LOOP UNTIL quitflag = 1

NEXT w

```

APPENDIX 4

'SPANNING_CHORDS

```

FOR w = 1 TO 24
shape$ = "bin2_" + LTRIM$(STR$(w))
file$ = shape$ + ".new"
OPEN file$ FOR INPUT AS #1

'find number of edge points
e = 0
DO
INPUT #1, x, y
e = e + 1
LOOP UNTIL EOF(1)
CLOSE #1

j = 10 'j is steplength
d = e + j
REDIM x(d), y(d)

OPEN file$ FOR INPUT AS #1
FOR i = 1 TO e
INPUT #1, x(i), y(i)
NEXT i
FOR i = 1 TO j
x(e + i) = x(i): y(e + i) = y(i)
NEXT i

shape$ = "2_" + LTRIM$(STR$(w)) + "_"
j$ = LTRIM$(STR$(j))
file$ = shape$ + j$ + ".len"
OPEN file$ FOR OUTPUT AS #3
legend$ = shape$ + j$
WRITE #3, legend$

FOR i = 1 TO e
x1 = x(i): y1 = y(i): x2 = x(i + j): y2 = y(i + j)
length = SQR((x2 - x1) ^ 2 + (y2 - y1) ^ 2)
WRITE #3, i, length, length / j
NEXT i
CLOSE

NEXT w

```


APPENDIX 5

'TO CONVERT A FILE OF EDGE CO-ORDINATES TO EVENLY SPACED POINTS

'reads from file shape\$.edg and writes to file shape\$.new

spacing = 1

FOR w = 1 TO 24

shape\$ = "bin2_" + LTRIM\$(STR\$(w))

file\$ = shape\$ + ".edg"

OPEN file\$ FOR INPUT AS #1

'find number of edge points

e = 0

DO

INPUT #1, x, y

e = e + 1

LOOP UNTIL EOF(1)

CLOSE #1

d = e + 1

REDIM x(d), y(d)

OPEN file\$ FOR INPUT AS #1

FOR i = 1 TO e

INPUT #1, x(i), y(i)

NEXT i

x(e + 1) = x(1): y(e + 1) = y(1)

CLOSE #1

file\$ = shape\$ + ".new"

OPEN file\$ FOR OUTPUT AS #2

'first point stays the same

newx = x(1): newy = y(1)

WRITE #2, newx, newy

j = 1

WHILE j < e

a = newx: b = newy

j = j + 1

DO

'step until the distance is greater than required spacing

j = j + 1

x1 = x(j): y1 = y(j): x2 = x(j + 1): y2 = y(j + 1)

LOOP UNTIL SQR((x(j + 1) - a)^2 + (y(j + 1) - b)^2) > spacing

'if stepping straight up or down then x stays the same, interpolate for y

IF x2 = x1 THEN

newx = x2

newy = b + SQR(spacing^2 - (x2 - a)^2)

' but newy could be the other side of b

IF ABS(newy - y2) + ABS(newy - y1) > ABS(y2 - y1) THEN

newy = b - SQR(spacing^2 - (x2 - a)^2)

```
END IF

'otherwise interpolate for both x and y
ELSE
m = (y2 - y1) / (x2 - x1)
c = (x2 * y1 - x1 * y2) / (x2 - x1)
newx = (a - m * (c - b) + SQR((m * (c - b) - a)^2 - (1 + m^2) * (a^2 + (c - b)^2 -
spacing^2))) / (1 + m^2)
IF ABS((newx - x2) + (newx - x1)) > ABS(x2 - x1) THEN
newx = (a - m * (c - b) - SQR((m * (c - b) - a)^2 - (1 + m^2) * (a^2 + (c - b)^2 -
spacing^2))) / (1 + m^2)
END IF
newy = m * newx + c
END IF
WRITE #2, newx, newy
WEND

CLOSE #2

NEXT w

END
```

APPENDIX 6

```

'RADIUS OF CURVATURE

ON ERROR GOTO straight          'infinite radius if three points are in
                                'straight line - assign large value instead

FOR w = 1 TO 24
shape$ = "bin2_" + LTRIM$(STR$(w))
file$ = shape$ + ".new"
OPEN file$ FOR INPUT AS #1

'find number of edge points
e = 0
DO
INPUT #1, x, y
e = e + 1
LOOP UNTIL EOF(1)
CLOSE #1

j = 7          'j is spacing
d = e + 2 * j
REDIM x(d), y(d)

OPEN file$ FOR INPUT AS #1
FOR i = 1 TO e
INPUT #1, x(i), y(i)
NEXT i
FOR i = 1 TO 2 * j
x(e + i) = x(i): y(e + i) = y(i)
NEXT i

j$ = LTRIM$(STR$(j))
shape$ = "2_0" + LTRIM$(STR$(w)) + "_"
file$ = shape$ + j$ + ".roc"
OPEN file$ FOR OUTPUT AS #3
legend$ = shape$ + j$
WRITE #3, legend$

' fit circle to  $x_{i-j}, y_{i-j}$   $x_i, y_i$   $x_{i+j}, y_{i+j}$ 
FOR i = j + 1 TO e + j
x1 = x(i - j): y1 = y(i - j): x2 = x(i): y2 = y(i): x3 = x(i + j): y3 = y(i + j)
b# = x1 * (x3^2 - x2^2 + y3^2 - y2^2) + x2 * (x1^2 - x3^2 + y1^2 - y3^2) + x3 *
(x2^2 - x1^2 + y2^2 - y1^2)
b# = b# / 2 / (x1 * (y3 - y2) + x2 * (y1 - y3) + x3 * (y2 - y1))
a# = y1 * (y3^2 - y2^2 + x3^2 - x2^2) + y2 * (y1^2 - y3^2 + x1^2 - x3^2) + y3 *
(y2^2 - y1^2 + x2^2 - x1^2)
a# = a# / 2 / (y1 * (x3 - x2) + y2 * (x1 - x3) + y3 * (x2 - x1))
roc# = SQR((x1 - a#)^2 + (y1 - b#)^2)
cont: WRITE #3, i, roc#
NEXT i
CLOSE

NEXT w

straight: IF ERR = 11 OR ERR = 6 THEN
roc# = 500

```

```
RESUME cont  
ELSE  
ON ERROR GOTO 0  
END IF
```

APPENDIX 7

Calculation of Axis Ratio

The second moment of area about the x axis of a particle of area A is defined as

$$I_x = \int_A y^2 dA$$

and the second moment about the y axis is

$$I_y = \int_A x^2 dA$$

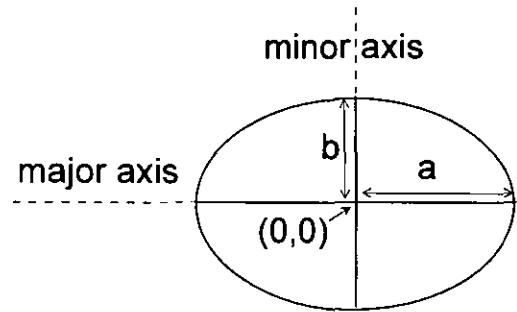
An ellipse centred on the origin with major axis $2a$ along the x axis and minor axis $2b$ along the y axis has the equation

$$\frac{x^2}{a^2} + \frac{y^2}{b^2} = 1$$

and its second moments of area are

$$I_x = \int_{-b}^b y^2 2x dy = \frac{\pi ab^3}{4}$$

$$I_y = \int_{-a}^a x^2 2y dx = \frac{\pi a^3 b}{4}$$



For an irregular particle of discrete pixels, each with area dA , located arbitrarily in the xy plane

$$I_x = \sum_n y^2, \quad I_y = \sum_n x^2, \quad I_{xy} = \sum_n xy$$

where $n = A =$ the number of pixels.

These moments cannot be compared with the moments of the ellipse defined above, unless the particle is centred on the origin with its principal axes along the x and y axes. Since this is rarely the case, the particle moments must be transformed to an appropriate co-ordinate system. The first step is to recalculate the moments about axes x', y' , whose origin is located at the centroid \bar{x}, \bar{y} of the particle, with x' parallel to x , and y' parallel to y (see diagram overleaf). The transformations are as follows:

$$I_{x'} = I_x - A\bar{y}^2, \quad I_{y'} = I_y - A\bar{x}^2, \quad I_{x'y'} = I_{xy} - A\bar{x}\bar{y}$$

The angle at which $I_{x'y'} = 0$ is the angle of the principal axes of the particle and can be found from the equation

$$\theta = \frac{1}{2} \tan^{-1} \left(\frac{2I_{x'y'}}{I_{y'} - I_{x'}} \right)$$

This defines the co-ordinate system of the particle, (x'', y'') , where

$$x'' = x' \cos \theta + y' \sin \theta$$

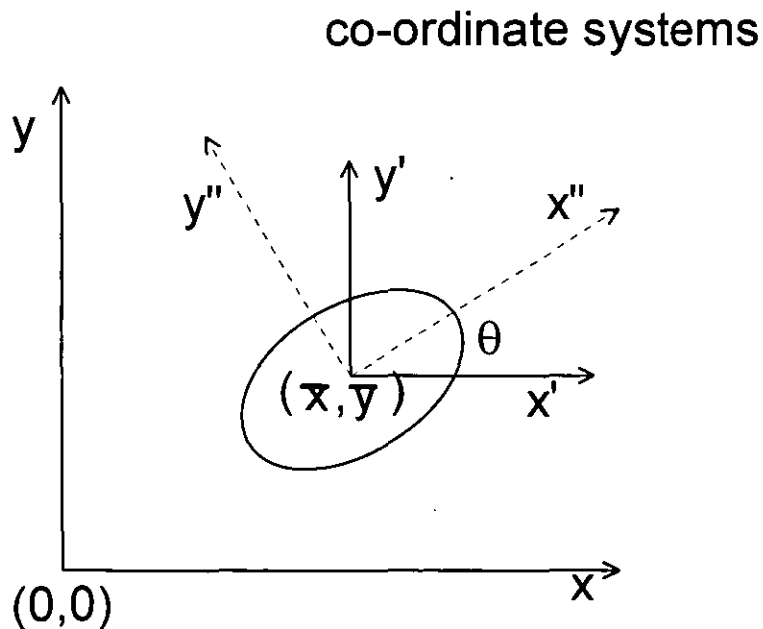
$$y'' = y' \cos \theta - x' \sin \theta$$

The particle moments are then recalculated as follows

$$I_{x''} = I_{x'} \cos^2 \theta + I_{y'} \sin^2 \theta - I_{x'y'} \sin 2\theta$$

$$I_{y''} = I_{y'} \cos^2 \theta + I_{x'} \sin^2 \theta + I_{x'y'} \sin 2\theta$$

Finally, these moments are equated with those of an ellipse, giving two equations with two unknowns, and a and b are found. The smaller of the two values is divided by the other to give the axis ratio.



APPENDIX 8

'CALCULATION OF AXIS RATIO

```

OPEN "axratio.prn" FOR OUTPUT AS #3

pi = 3.141592653589793#

FOR w = 1 TO 24
WRITE #3, "bin 2, particle ", w

w$ = LTRIM$(STR$(w))
name$ = "bin2_" + w$
file$ = name$ + ".gry"
OPEN file$ FOR INPUT AS #1
' file contains greylevel values for rectangular ROI
' format n.g1.g2.g3.....gn where n is no. of points per line
DIM P(100, 100) ' P(x,y) takes the value 1 if pixel x,y is particle, 0 for
' background, and 2 for edge

'read in the file, assign xy co-ordinates and identify particle pixels
y = 0: count = 0: sumx = 0: sumy = 0
sumxx = 0: sumyy = 0: sumxy = 0
DO
INPUT #1, n
y = y + 1
FOR x = 1 TO n
INPUT #1, G
IF G < 20 THEN
    sumx = sumx + x
    sumy = sumy + y
    sumxx = sumxx + x ^ 2
    sumyy = sumyy + y ^ 2
    sumxy = sumxy + x * y
    count = count + 1
    ymax = y
END IF
NEXT x
LOOP UNTIL EOF(1)

'find centroid
xcen = sumx / count: ycen = sumy / count

CLOSE #1

'recalculate moments about parallel axes through centroid
xx = sumxx - count * xcen ^ 2
yy = sumyy - count * ycen ^ 2
xy = sumxy - count * xcen * ycen

'find angle of principal axes
angle = .5 * ATN(2 * xy / (xx - yy))

'recalculate moments about principal axes
Ix = yy * (COS(angle)) ^ 2 + xx * (SIN(angle)) ^ 2 - xy * SIN(2 * angle)
Iy = xx * (COS(angle)) ^ 2 + yy * (SIN(angle)) ^ 2 + xy * SIN(2 * angle)

```

```
'calculate major and minor axes of equivalent ellipse  
a = (16 * Iy ^ 3 / pi ^ 2 / Ix) ^ (1 / 8)  
b = (16 * Ix ^ 3 / pi ^ 2 / Iy) ^ (1 / 8)  
  
IF a > b THEN axratio = b / a ELSE axratio = a / b  
PRINT axratio  
  
WRITE #3, axratio  
  
NEXT w  
  
END
```


APPENDIX 9

```
'EXPERT SYSTEM
'TRAINING AND TESTING PROGRAMME

OPEN "train.txt" FOR INPUT AS #1
INPUT #1, v, q, n 'number of variables, outcomes, training examples
DIM r(v, q), t(v, q), e(v + 1, n), v(v), d(q), a(q)
'read examples and classes into array e
FOR m = 1 TO n
FOR i = 1 TO v + 1: INPUT #1, e(i, m): NEXT
NEXT m
CLOSE #1

RANDOMIZE TIMER

reps = 20

FOR w = 1 TO 10 'train and test ten times

'-----
FOR y = 1 TO reps 'averaging 20 sets of rules each time

'initialise rules to 0
FOR j = 1 TO q: FOR i = 1 TO v
t(i, j) = 0
NEXT: NEXT

FOR x = 1 TO 1000 'train with 1000 examples

d = 0: flag = 0
k = INT(RND(1) * n + 1) 'pick an example, k
q1 = e(v + 1, k) 'q1 is the outcome for k
'evaluate decision rule for this outcome
FOR i = 1 TO v: d = d + e(i, k) * t(i, q1): NEXT
FOR j = 1 TO q
'evaluate decision rules for the other (incorrect) outcomes
d2 = 0
IF j <> q1 THEN
FOR i = 1 TO v: d2 = d2 + e(i, k) * t(i, j): NEXT
IF d2 >= d THEN 'alter if not smaller than correct decision rule
FOR i = 1 TO v: t(i, j) = t(i, j) - e(i, k): NEXT
'alter correct decision rule if not already done
IF flag = 0 THEN
FOR i = 1 TO v: t(i, q1) = t(i, q1) + e(i, k): NEXT
flag = 1
END IF
END IF
END IF
NEXT j

NEXT x

'sum the rules for averaging later
FOR j = 1 TO q: FOR i = 1 TO v
r(i, j) = r(i, j) + t(i, j)
```

```

NEXT: NEXT

NEXT y
-----
'average the rules
FOR j = 1 TO q: FOR i = 1 TO v
r(i, j) = r(i, j) / reps
NEXT: NEXT

'test the averaged rules
OPEN "test.txt" FOR INPUT AS #1

c = 0: nd = 0
INPUT #1, a, b, z    'number of variables, outcomes and examples

FOR x = 1 TO z

'read the variables and class
FOR i = 1 TO v
INPUT #1, v(i)
NEXT
INPUT #1, q2    'q2 is the correct outcome
FOR j = 1 TO q: d(j) = 0: NEXT
'evaluate decision rules for each outcome
FOR i = 1 TO v
FOR j = 1 TO q
d(j) = d(j) + v(i) * r(i, j)
NEXT j: NEXT i

'find the winner
d = d(1): hi = 1
FOR j = 2 TO q
IF d(j) > d THEN
    d = d(j): hi = j
END IF
NEXT

'see if winner matches correct outcome
flag1 = 0
FOR j = 1 TO q
IF d(j) = d AND j <> hi THEN flag1 = 1
NEXT
IF flag1 = 1 THEN
nd = nd + 1    'no decision if more than one winner
ELSE
IF hi = q2 THEN c = c + 1 'c=no. correct predictions
END IF

NEXT x

CLOSE #1
PRINT c * 100 / z, nd * 100 / z

NEXT w

END

```

APPENDIX 10

'NEURAL NETWORK

'BACK PROPAGATION

'WIDROW LEARNING - BATCH METHOD

```

OPEN "train.txt" FOR INPUT AS #1
INPUT #1, v, q, n
'v= no.variables, q=no.outcomes, n=no.training examples
DIM e(v + 1, n)
'read training examples into array e()
FOR m = 1 TO n
FOR i = 1 TO v + 1
INPUT #1, e(i, m)
NEXT i
NEXT m
CLOSE #1

OPEN "test.txt" FOR INPUT AS #1
INPUT #1, v, q, n2
'v= no.variables, q=no.outcomes, n2=no.testing examples
DIM t(v + 1, n2)
'read testing examples into array t()
FOR m = 1 TO n2
FOR i = 1 TO v + 1
INPUT #1, t(i, m)
NEXT i
NEXT m
CLOSE #1

'set number of input, hidden and output nodes and weights
inode = v: hnode = v + 2: onode = q
'generally i for input, h for hidden, o for output
DIM wih(inode + 1, hnode), who(hnode + 1, onode) 'extra is for bias weight
DIM Ah(hnode + 1), Ao(onode) 'activation
DIM deltao(onode), deltah(hnode)
DIM sumho(hnode + 1, onode), sumih(inode + 1, hnode), sumwhodel(hnode)
DIM error(onode), sumerr(onode)
DIM changeho(hnode + 1, onode), changeih(inode + 1, hnode)
DIM nodeo(onode + 1), nodeh(hnode)

eta = .7: alpha = .9
cmax = .1 * n2
batchsize = 10
numbatches = 100

RANDOMIZE TIMER

FOR L = 1 TO 50

'initialise weights randomly between -1 and 1
FOR i = 1 TO inode + 1
FOR h = 1 TO hnode
changeih(i, h) = 0

```

```

wih(i, h) = .01 * (INT(RND(1) * 200 + 1) - 100)
NEXT h
NEXT i

FOR h = 1 TO hnode + 1
FOR o = 1 TO onode
who(h, o) = .01 * (INT(RND(1) * 200 + 1) - 100)
changeho(h, o) = 0
NEXT o
NEXT h

'-----training loop-----
FOR batch = 1 TO numbatches

FOR h = 1 TO hnode + 1
FOR o = 1 TO onode
sumho(h, o) = 0
NEXT o
NEXT h

FOR h = 1 TO hnode
FOR i = 1 TO inode + 1
sumih(i, h) = 0
NEXT i
NEXT h

trainex = 0
'-----batch loop-----
DO

trainex = trainex + 1
'select an example and feed it through
k = INT(RND(1) * n + 1)

'calculate activation for hidden nodes
FOR h = 1 TO hnode
  nodeh(h) = 0
  FOR i = 1 TO inode
    nodeh(h) = nodeh(h) + e(i, k) * wih(i, h)
  NEXT i
  nodeh(h) = nodeh(h) + wih(inode + 1, h)      'add bias
  Ah(h) = 1 / (1 + EXP(-nodeh(h)))
NEXT h

'calculate activation for output nodes
Ah(hnode + 1) = 1
FOR o = 1 TO onode
  nodeo(o) = 0
  FOR h = 1 TO hnode + 1
    nodeo(o) = nodeo(o) + Ah(h) * who(h, o)
  NEXT h
  Ao(o) = 1 / (1 + EXP(-nodeo(o)))
NEXT o

'find winning output neuron
winner = 1
FOR o = 2 TO onode
IF Ao(o) > Ao(winner) THEN winner = o

```

```

NEXT o
'calculate errors
IF e(v + 1, k) = winner THEN
FOR o = 1 TO onode: error(o) = 0: NEXT
ELSE
FOR o = 1 TO onode
IF o = e(v + 1, k) THEN
error(o) = 1 - Ao(o)
ELSE
IF Ao(o) > Ao(e(v + 1, k)) THEN
error(o) = 0 - Ao(o)
ELSE
error(o) = 0
END IF
END IF
NEXT o
END IF

FOR o = 1 TO onode
deltao(o) = error(o) * Ao(o) * (1 - Ao(o))
NEXT o

'sum delta*input for each h-o connection
FOR o = 1 TO onode
FOR h = 1 TO hnode + 1
sumho(h, o) = sumho(h, o) + deltao(o) * Ah(h)
NEXT h
NEXT o

'calculate hidden deltas
FOR h = 1 TO hnode
sumwhodel(h) = 0
NEXT h
FOR h = 1 TO hnode
FOR o = 1 TO onode
sumwhodel(h) = sumwhodel(h) + who(h, o) * deltao(o)
NEXT o
deltah(h) = Ah(h) * (1 - Ah(h)) * sumwhodel(h)
NEXT h

'sum delta*input for each i-h connection
FOR h = 1 TO hnode
FOR i = 1 TO inode
sumih(i, h) = sumih(i, h) + deltah(h) * e(i, k)
NEXT i
sumih(inode + 1, h) = sumih(inode + 1, h) + deltah(h)
NEXT h

LOOP UNTIL trainex = batchsize
'-----end of batch-----

'adjust weights
FOR o = 1 TO onode
FOR h = 1 TO hnode + 1
who(h, o) = who(h, o) + eta * sumho(h, o) / trainex + alpha * changeho(h, o)
changeho(h, o) = eta * sumho(h, o) / trainex + alpha * changeho(h, o)
NEXT h
NEXT o

```

```

FOR h = 1 TO hnode
FOR i = 1 TO inode + 1
wih(i, h) = wih(i, h) + eta * sumih(i, h) / trainex + alpha * changeih(i, h)
changeih(i, h) = eta * sumih(i, h) / trainex + alpha * changeih(i, h)
NEXT i
NEXT h

```

```

NEXT batch

```

```

'-----end of training-----

```

```

'testing

```

```

c = 0

```

```

FOR k = 1 TO n2

```

```

'calculate activation for hidden nodes

```

```

FOR h = 1 TO hnode

```

```

  nodeh(h) = 0

```

```

  FOR i = 1 TO inode

```

```

    nodeh(h) = nodeh(h) + t(i, k) * wih(i, h)

```

```

  NEXT i

```

```

  nodeh(h) = nodeh(h) + wih(inode + 1, h)      'add bias

```

```

  Ah(h) = 1 / (1 + EXP(-nodeh(h)))

```

```

NEXT h

```

```

'calculate activation for output nodes

```

```

Ah(hnode + 1) = 1

```

```

FOR o = 1 TO onode

```

```

  nodeo(o) = 0

```

```

  FOR h = 1 TO hnode + 1

```

```

    nodeo(o) = nodeo(o) + Ah(h) * who(h, o)

```

```

  NEXT h

```

```

  Ao(o) = 1 / (1 + EXP(-nodeo(o)))

```

```

NEXT o

```

```

winner = 1

```

```

FOR o = 2 TO onode

```

```

IF Ao(o) > Ao(winner) THEN winner = o

```

```

NEXT o

```

```

IF winner = t(v + 1, k) THEN c = c + 1

```

```

NEXT k

```

```

PRINT L, c * 100 / n2

```

```

IF c > cmax THEN

```

```

  OPEN "weights.txt" FOR OUTPUT AS #1

```

```

  FOR o = 1 TO onode

```

```

    FOR h = 1 TO hnode + 1

```

```

      WRITE #1, who(h, o)

```

```

    NEXT h

```

```

  NEXT o

```

```

  FOR h = 1 TO hnode

```

```

    FOR i = 1 TO inode + 1

```

```

      WRITE #1, wih(i, h)

```

```

    NEXT i

```

```

  NEXT h

```

```

  CLOSE

```

```

cmax = c

```

```

END IF

```

```

NEXT L

```

